Journal of

# Computation and Artificial Intelligence in Mechanics and Biomechanics

Editor in Chief:
Jorge Belinha

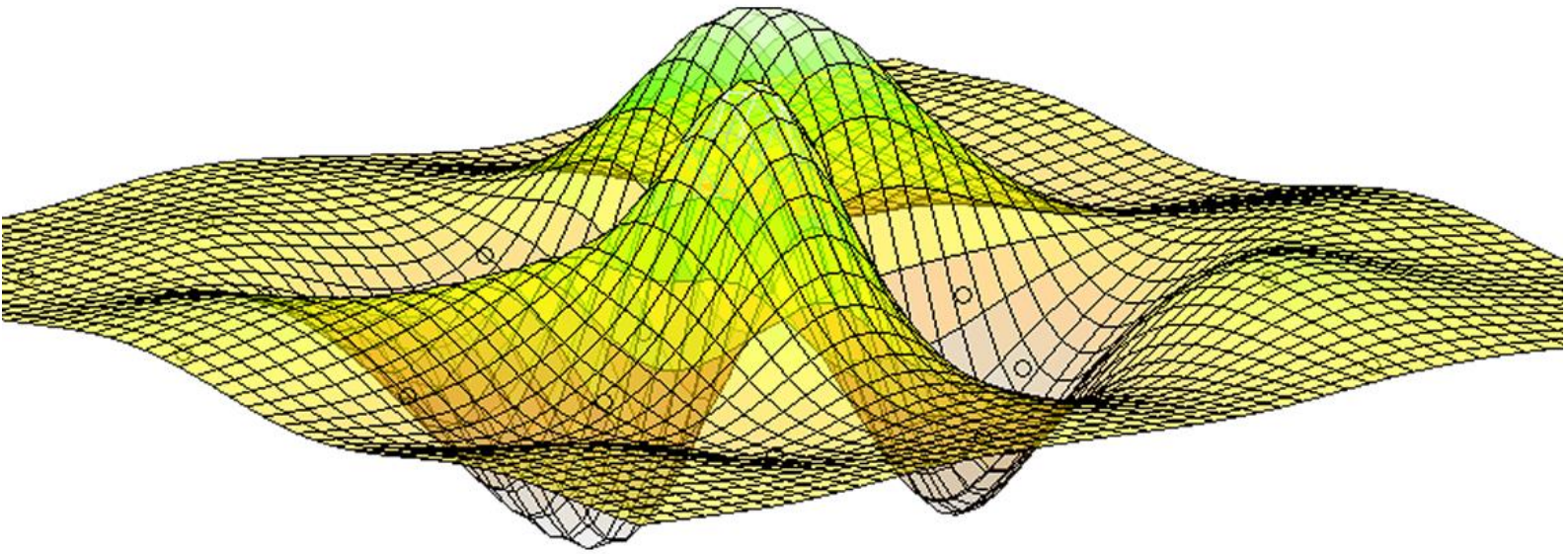

ISSN 2184-8971
Volume 2, Issue 2


PUBLICAÇÕES ISEP
European Commission | Horizon 2020 European Union funding for Research & Innovation
OpenAIRE
zenodo

# Journal of Computation and Artificial Intelligence in Mechanics and Biomechanics

**Editorial overview by**

Editor in chief: Jorge Belinha [1]

[1]*School of Engineering, Polytechnic of Porto (ISEP), Department of Mechanical Engineering, Portugal, job@isep.ipp.pt*

Journal of Computation and Artificial Intelligence in Mechanics and Biomechanics (JCAIMB) is a scholarly online peer review free open access journal fully sponsored by "Publicações ISEP". All manuscripts are available in the ZENODO repository database, from OpenAIRE project, allowing an automatically abstracting and indexation and free open access.

Thus, JCAIMB is committed to ensure free Open Science to both authors and readers and to publish only quality works, which are reviewed by experts in related field. Moreover, JCAIMB aims to publish quality original research works, following the scientific method of scholarly value in computational mechanics and biomechanics combined with several degrees of artificial intelligence, whose formulations and applications are properly demonstrated and validated. Nevertheless, innovative applications using commercial software packages are encouraged, as well as original and up-to-date revision manuscripts. In this issue, four manuscripts are published in JCAIMB:

- Bending analysis of antisymmetric angle-ply laminates using HSDTs and the radial point interpolation method – Part I: Literature review and formulation, by D.E.S. Rodrigues, Renato N. Natal Jorge and J. Belinha;
- Bending analysis of antisymmetric angle-ply laminates using HSDTs and the radial point interpolation method – Part II: numerical examples, by D.E.S. Rodrigues, Renato N. Natal Jorge and J. Belinha;
- Combining artifcial neural networks with fnite element methods to predict the structural response of the proximal femur, by A.I. Pais, J.L. Alves and J. Belinha;
- An elastoplastic constitutive model to simulate the non-linear behaviour of chitosan material for nerve regeneration guide tubes applications, by J. Gomes, R.M. Natal Jorge and J.Belinha.

Enjoy.

The editorial team.

**Technical information:**

| | |
|---|---|
| Publisher: | Publicações ISEP - https://publicacoes.isep.ipp.pt/ |
| Repository: | ZENODO repository database - https://zenodo.org/ |
| Licence: | under the terms of the Creative Commons Attribution 4.0 International (CC BY 4.0) license. |
| Director: | Jorge Belinha |
| Email: | job@isep.ipp.pt |
| Format: | Online: https://publicacoes.isep.ipp.pt/jcaimb |
| Periodicity: | Semestrial |

*Journal of Computation and Artificial Intelligence in Mechanics and Biomechanics* ISSN 2184-8971
*Volume 2, Issue 2, Page 55-72, 2022*

# Bending analysis of antisymmetric angle-ply laminates using HSDTs and the radial point interpolation method – Part I: Literature review and formulation

D. E.S. Rodrigues [1,2,3], J. Belinha [1, 2], R.M. Natal Jorge [1,4]

[1] *Institute of Science and Innovation in Mechanical and Industrial Engineering (INEGI), Porto, Portugal*
*2 School of Engineering, Polytechnic of Porto (ISEP), Department of Mechanical Engineering, Porto, Portugal.*
*3 University of Aveiro, Department of Mechanical Engineering, Campus Universitário de Santiago, Aveiro, Portugal.*
*4 Faculty of Engineering, University of Porto (FEUP), Department of Mechanical Engineering, Porto, Portugal.*

***Abstract***
*The mechanics of laminated plates is primarily studied using the Finite Element Method (FEM), which is often combined with plate models. Those plate models can be High-Order Shear Deformation Theories (HSDTs) since they accurately predict the nonlinear distributions of the shear stresses through-thickness. In this work, five HSDTs proposed in the literature are used to study the bending behavior of antisymmetric laminates with angle-ply layers. However, instead of using the traditional FEM, this study proposes the use of a meshless method: the Radial Point Interpolation Method (RPIM). Meshless methods can offer some advantages over the FEM, such as in problems involving transitory geometries where the FEM may require re-meshing processes. In meshless methods, the shape functions have virtually a high order allowing higher continuity and reproducibility. Furthermore, they only require an unstructured nodal distribution discretizing the problem domain, meaning that there is no previous relationship between nodes, which simplifies the refinement procedure. In this first part of two articles, the RPIM and different HSDTs are combined to future analyze several antisymmetric angle-ply laminates in the second part. The RPIM's formulation is presented and the HSDT's are implemented within a meshless code.*

***DOI**: 10.5281/zenodo.7492955*

*Article Info*

*Keywords*
*Meshless methods*
*Radial point interpolation method*
*Antisymmetric angle-ply laminate*
*High-Order Shear Deformation Theory*
*Plates theory*

*Article History*

| | |
|---|---|
| *Received:* | *12/10/2022* |
| *Revised:* | *16/11/2022* |
| *Accepted:* | *09/12/2022* |

## 1. Introduction

Composite laminates are advanced materials composed of fibres mixed in a matrix in a layer-by-layer arrangement. Their main advantages over the most common metallic materials are their high specific mechanical properties which make them ideal to be used in advanced structures like aircraft, automobiles, vessels, wind blades, etc. Composite laminates offer high strength and low weight. Thus, the behaviour of such materials needs to be studied accurately in order to prevent failure mechanisms and to guarantee the integrity of the structure where they are being used.

One of the most common ways in which these materials appear in the engineering field is in a plate form. Plates are three-dimensional solids that can often be treated as a 2D simplification since their thickness is much smaller than their other dimensions. In those cases, the mechanical behaviour of the plate is studied through a plate theory. Plate theories interpolate the in-plane displacements of a plate through its thickness using different mathematical expressions. The first known plate theory is the one proposed by Gustav Kirchhoff. It was suggested in the middle of the 19th century and then it was developed by Augustus-Love in 1888 and, because of that, is now known as the Kirchhoff-Love plate theory or the Classical Plate Theory (CLPT). The assumptions of the Kirchhoff-Love are: (1) when a plate is subjected to a bending load, straight lines perpendicular to the mid-surface before deformation remain straight after deformation; (2) straight lines normal to the mid-surface remain normal to the mid-surface after deformation and (3) the plate does not experience elongation along with the thickness. Due to those considerations, the CLPT neglects shear effects that are predominantly found in thick and moderately thick laminated plates.



*Corresponding Author:*
*Jorge Belinha*
*job@isep.ipp.pt*

About 100 years later, Mindlin [1]–[4] developed the First-Order Shear Deformation Theory (FSDT), which considers shear effects. The assumptions of Mindlin are similar to the ones proposed by Kirchhoff but with a significant difference: straight lines perpendicular to the mid-surface before deformation remain straight but not necessarily normal to the mid-surface after deformation. Reissner, a few years after, developed a plate theory also including shear effects and they are both known nowadays as the Reissner-Mindlin plate theory. In the Reissner-Mindlin plate theory, the displacement field is obtained considering that the in-plane displacements are linearly distributed through the plate thickness. Thus, despite considering the shear effects, the FSDT predicts constant shear stresses across the thickness of the plate.

The interpolation of the in-plane displacements can be performed using higher-order functions (transverse shear functions) which also capture the non-linear behaviour observed in the distribution of the shear stresses across the laminate thickness. Such theories are called high-order shear deformation theories (HSDTs) and they can be used to predict with accuracy the mechanical behaviour of composite laminates. Additionally, HSDTs fulfil the traction boundary condition (zero shear stresses at the top and bottom faces of the plate) and do not need shear correction factors, unlike the FSDT. Each HSDT possesses a different transverse shear function which can have several mathematical forms such as polynomials [5]–[7], trigonometric [8], and hyperbolic [9], [10] functions, or the combination of trigonometric and exponential functions [11], etc.

The plate theories mentioned before are also called Equivalent Single Layer (ESL) Theories since they treat the laminate (composed of several layers) as a plate with just one layer. There are also layerwise (LW) theories (considering independent degrees of freedom for each layer) [12] and the zigzag (ZZ) theories [13] (where the kinematic behaviour is described on the whole laminate, and local refinement approach acts on the scale of the layer thickness [13]). These two approaches, even though being more accurate, are also computationally expensive. These plate models will not be analysed in this study.

The mechanical, vibrational, and dynamic analysis of composite laminates using HSDTs is not often performed through analytical procedures. Numerical tools like the Finite Element Method (FEM) or the Generalized Differential Quadrature (GDQ) method (which is a strong formulation of the governing equations applied in [14]–[17] to doubly-curved laminated composite shells and panels) offer easier ways to obtain solutions for complex problems. The FEM discretizes the problem domain in small sub-domains called elements. It is the association of these elements that forms a mesh where the nodal connectivity can be found. Since it is "mesh-reliant", the FEM can find some limitations like the re-meshing process that is required in problems involving mesh distortion (large deformations, crack propagation, etc). Unlike the FEM, meshless methods only require an unstructured nodal distribution in order to discretize the problem domain. Thus, the concept of mesh or element does not exist [18]. The nodal connectivity is imposed by an overlapping rule of 'influence-domains' - areas or volumes in which the field variables are approximated. Meshless methods can offer some advantages when compared with the FEM. Meshless methods do not require re-meshing procedures, they have shape functions with a virtually higher order, allowing a higher continuity and reproducibility, and the refinement procedure is simpler – nodes can be added or removed from the nodal mesh [19].

This work makes use of a simple meshless method, the Radial Point Interpolation Method (RPIM) [20], to analyse the bending behaviour of antisymmetric angle-ply laminates using HDSTs. The RPIM uses radial interpolation functions, possessing the compact support and the delta Kronecker properties, to interpolate the field variables within 'influence-domains'. To integrate the discrete system of equations obtained from the Galerkin weak form, a nodal independent background integration mesh is used, based on the Gauss-Legendre integration scheme. This makes the RPIM a 'not truly meshless method' since the mesh-free characteristic of the method is not verified [18]. In the following sections, the RPIM's formulation is explained, the HSDTs are presented, and the framework of the developed in-house code is detailed.

## 2. Meshless Methods

It is useful to analyze meshless methods, as almost all kinds of numerical methods, through three fundamental parts: the field approximation (or interpolation) function, the used formulation and the integration [18]. Regarding the field approximation, meshless methods can be divided into approximant and interpolant meshless methods, depending on the type of shape functions used. Some of the most relevant approximant meshless methods use the Taylor approximation, the Moving Least-Square (MLS) approximation, the Reducing Kernel approximation, or the hp-cloud approximation. The Meshless Local Petrov-Galerkin Method (MLPG) [21], the Reproducing Kernel Particle Method (RKPM) [22] or the Finite Point Method (FPM) [23] are approximant meshless methods that appeared first but, despite their successful application to computational mechanics [19], they do not possess a very attractive and useful numerical property: the delta Kronecker property. Thus, interpolant meshless methods proposed more recently possess the delta Kronecker

property, simplifying the numerical imposition of the essential and natural boundary conditions. The Point Interpolation Method (PIM) [24] is a well know interpolant meshless method that has several versions, as can be found in the literature. The Radial Point Interpolation Method (RPIM) [20] is a version of PIM since it makes use of its polynomial basis and it combines them with radial basis functions (RBF) to interpolate the field variables. The radial interpolation functions used in the RPIM possess the compact support and the delta Kronecker properties.

Meshless methods appeared first in 1977 when the Smooth Particle Hydrodynamics Method (SPH) [25] was proposed. Nevertheless, the considered first global weak form-based meshless method was only presented in 1994 with the development of the Element Free Galerkin Method (EFGM) [26], [27]. However, schemes based on the MSL initially gave birth to the actual first weak-form domain-type meshless method in 1992, named the Diffuse Element Method (DEM) [28] – which was then extended creating the EFGM.

Thus, in terms of formulation, the meshless methods can be classified, as the FEM, in two categories: strong and weak formulations. The RPIM uses the Galerkin weak form to obtain the discrete system of equations. In the literature, there are also meshless methods based on strong form formulations, but they are not analysed in this study.

Concerning the integration scheme, it can be performed using nodal dependent or nodal independent integration meshes. As already mentioned in the introductory section, the RPIM uses a nodal independent integration mesh that covers the problem domain, and it is composed of integration points (with correspondent integration weights). Other meshless methods, such as the one developed by Belinha et al. [29] – the Natural Neighbour Radial Point Interpolation Method (NNRPIM) - uses the Voronoï Diagram concept to determine 'influence-cells' and the integration scheme is based on that geometrical construction, creating an integration mesh dependent on the nodal mesh.

Other relevant meshless methods are the Point Assembly Method (PAM) [30], the Natural Element Method (NEM) [31], the Method of Finite Spheres (MFS) [32], or the Meshless Finite Element Method (MFEM) [33].

### 2.1. The RPIM formulation

In the Radial Point Interpolation Method (RPIM), the nodes are arbitrarily distributed and they do not have any spatial relationship. Thus, in order to ensure the nodal connectivity, 'influence-domains' are constructed and overlapped.

The numerical procedure of the RPIM is initialized with the discretization of the problem domain in a set of nodes forming a regular or irregular nodal mesh (the irregular nodal mesh has, in general, lower accuracy). The next step is to create the integration mesh which, in the case of the RPIM, is based on the Gauss-Legendre integration scheme. The integration mesh can be fitted to the problem domain, or it can have a regular shape (in this case, it is necessary to remove the integration points placed outside the problem domain). The nodal independent background integration meshes constructed in the scope of this work are composed of quadrilateral cells (with isoparametric shape) containing integration points with a correspondent integration weight. Then, for each integration point of the integration mesh, the mentioned 'influence-domains' are defined. 'Influence-domains' are areas (for two-dimensional problems) or volumes (for three-dimensional problems), concentric with the integration points and containing a certain number of nodes of the nodal mesh. In this work, since the plate models are two-dimensional problems, 'influence-domains' are areas. These areas can contain a fixed number of nodes or a variable number of nodes, as suggested by Fig.1.

The literature recommends [18] the use of 'influence-domains' with a fixed number of nodes, between 9 and 16 nodes, which allows the construction of shape functions with the same degree of complexity. The different 'influence-domains' constructed for each integration point overlap each other, ensuring the nodal connectivity of the numerical method.

Using the 'influence-domain' concept, the field variables are interpolated. Thus, the displacement field at the interest point $\boldsymbol{x}_{\mathrm{I}}$, $u(\boldsymbol{x}_{\mathrm{I}})$, is obtained interpolating the displacement fields observed in each node within the 'influence-domain' of $\boldsymbol{x}_{\mathrm{I}}$, Eq. (1):

$$u(\boldsymbol{x}_{\mathrm{I}}) = \sum_{\mathrm{j}=1}^{n} \varphi_j(\boldsymbol{x}_{\mathrm{I}})\, \boldsymbol{u}_j \tag{1}$$

where $n$ is the number of nodes within the 'influence-domain' of $\boldsymbol{x}_{\mathrm{I}}$, $\boldsymbol{u}_j$ represents the displacements of each node $j$ and $\varphi_j(\boldsymbol{x}_{\mathrm{I}})$ is the shape function of the node $j$ obtained using the $n$ nodes within the 'influence-domain' [29]. The

interpolation functions used in the RPIM are the result of the combination of multiquadric (MQ) radial basis functions (RBFs) and polynomial basis functions, and are presented in detail in the literature [29].

After the interpolation functions are calculated, the discrete system of equations is established from the Galerkin weak form (the meshless discrete system of equations is obtained in Appendix A), the boundary conditions are applied using, for instance, the Gauss elimination method [29], and solutions are found.

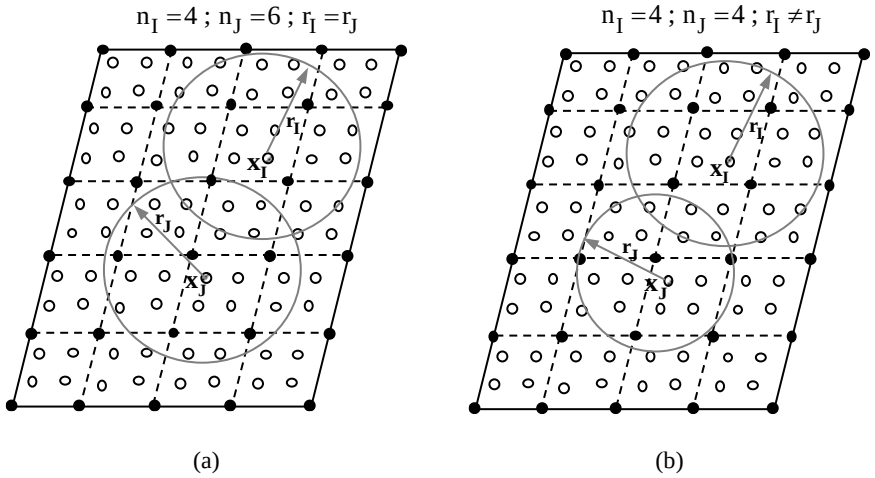


**Fig.1** - (a) 'Influence-domain' with a fixed area ( $r_I = r_J$ ); (b) 'Influence-domain' with a variable area ( $r_I \neq r_J$ ) but a fixed number of nodes.

## 3. High-Order Shear Deformation Theories

Higher-Order Shear Deformation Theories (HSDTs) are Equivalent Single Layer Theories which allow higher accuracy than the First-Order Shear Deformation Theory (FSDT) when dealing with shear stresses. In the literature, it can be found several HSDTs that, as mentioned in the introductory section, have different transverse shear functions. The first proposed HSDT was the one developed by Ambartsumian [28], firstly applied to the analysis of anisotropic plates and shallow shells and later adapted for the analysis of composite materials. The Third-Order Shear Deformation Theory (TSDT) by J. N. Reddy [34] is probably the most well-known HSDT, although some works by Kant et al. [35]–[37], Levinson [38] and Murthy [39] about similar third-order theories are dated before Reddy's. Shi [40], [41], [6] also developed a simple TSDT mathematically similar to Reddy's theory. Nguyen-Xuan [42] also proposed a plate model using a fifth-degree polynomial as the transverse shear function (it is a Five-Order Shear Deformation Theory). Other authors proposed transverse shear functions that are not polynomials: Mantari [43], Karama [30] and Aydogdu [31] used exponential shape functions, Touratier [8] and Grover [46] consider trigonometric shape functions, Mantari [11] also developed shape functions which are combinations of exponential and trigonometric functions, Soldatos [47] and Meiche [10] made use of hyperbolic functions, etc.

This work uses five of these HSDTs in the bending analysis of antisymmetric angle-ply composite laminated plates. In this section, some of those HSDTs found in the literature are studied. Their displacement and strain fields are obtained and, in the end, the matrixes composing the discrete system of equations obtained in Appendix A are established.

### 3.1. Displacement Field. Strain-Stress Relations

Consider the plate represented in Fig.2, with dimensions a, b and h. Consider also that the plate is subjected to a generic load that produces displacements along with the directions of the coordinate axis $Oxyz$ – displacement $u(x, y, z)$ in direction $Ox$, $v(x, y, z)$ in direction $Oy$ and $w(x, y, z)$ in direction $Oz$.

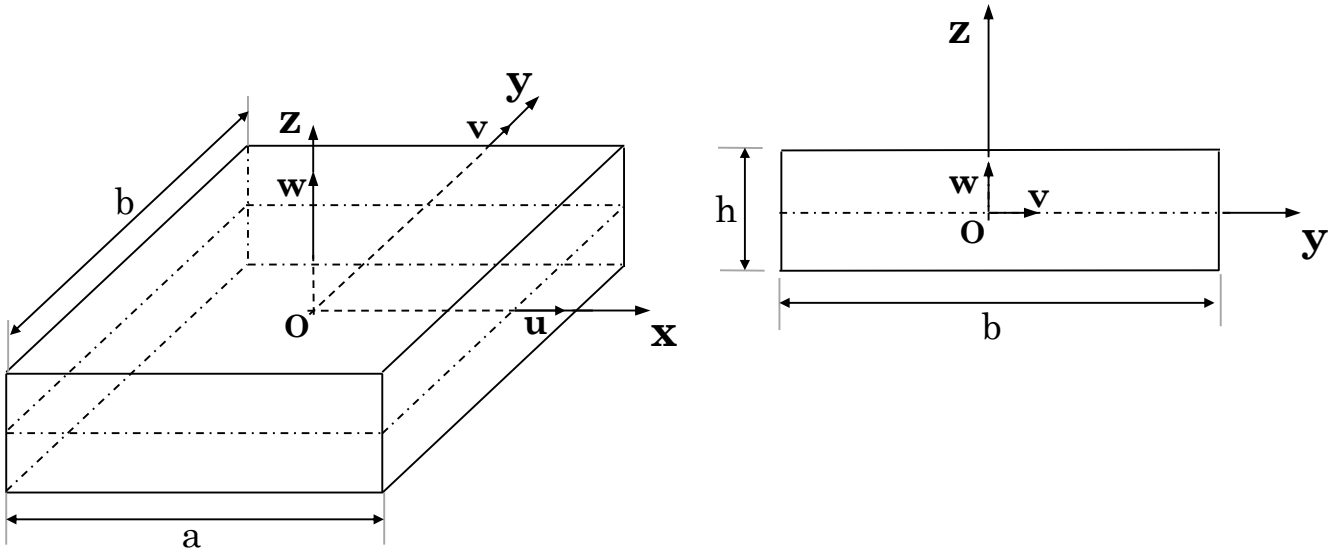


**Fig. 2** – Generic geometry of a plate and coordinate system.

In Equivalent Single Layer (ESL) theories, those displacements can be written in terms of five independent degrees of freedom, three displacements along with the three coordinate axes, $Ox, Oy$ and $Oz$, and two rotations: $u_0(x,y)$, $v_0(x,y)$, $w_0(x,y)$, $\phi_x(x,y)$ and $\phi_y(x,y)$,

$$\begin{aligned} u(x,y,z) &= u_0(x,y) + f(z)\cdot\left[\phi_x(x,y) + \frac{\partial w_0(x,y)}{\partial x}\right] - z\cdot\frac{\partial w_0(x,y)}{\partial x} \\ v(x,y,z) &= v_0(x,y) + f(z)\cdot\left[\phi_y(x,y) + \frac{\partial w_0(x,y)}{\partial y}\right] - z\cdot\frac{\partial w_0(x,y)}{\partial y} \\ w(x,y,z) &= w_0(x,y) \end{aligned} \tag{2}$$

where $f(z)$ is a transverse shear function depending on the variable $z$. Thus, if $f(z) = z$, Eq. (2) becomes the displacement field proposed by the FSDT:

$$\begin{aligned} u(x,y,z) &= u_0(x,y) + z\cdot\phi_x(x,y) \\ v(x,y,z) &= v_0(x,y) + z\cdot\phi_y(x,y) \\ w(x,y,z) &= w_0(x,y) \end{aligned} \tag{3}$$

Unlike the HSDTs, the FSDT does not verify the traction boundary conditions at the top and bottom faces of the plate since the shear stresses at those locations are not zero ( $f'(h/2) = f'(-h/2) \neq 0$ ). The strain field is obtained by spatial derivation of the displacement field. Notice that for ESL theories, $\varepsilon_{zz} = 0$ - i.e. the component of the strain along with the $Oz$ direction is considered null. The strain tensor can be written in the Voigt notation as: $\boldsymbol{\varepsilon} = \left\{\varepsilon_{xx}\ \varepsilon_{yy}\ \gamma_{xy}\ \gamma_{yz}\ \gamma_{xz}\right\}^{\mathrm{T}}$, whose components are determined in Eq. (4):

$$\boldsymbol{\varepsilon}=\begin{bmatrix}\varepsilon_{xx}\\ \varepsilon_{yy}\\ \gamma_{xy}\\ \gamma_{yz}\\ \gamma_{xz}\end{bmatrix}=\begin{bmatrix}\dfrac{\partial u}{\partial x}\\ \dfrac{\partial v}{\partial y}\\ \dfrac{\partial u}{\partial y}+\dfrac{\partial v}{\partial x}\\ \dfrac{\partial v}{\partial z}+\dfrac{\partial w}{\partial y}\\ \dfrac{\partial u}{\partial z}+\dfrac{\partial w}{\partial x}\end{bmatrix}=\begin{bmatrix}\dfrac{\partial u_0}{\partial x}+[f(z)-z]\cdot\dfrac{\partial^2 w_0}{\partial x^2}+f(z)\cdot\dfrac{\partial \phi_x}{\partial x}\\ \dfrac{\partial v_0}{\partial y}+[f(z)-z]\cdot\dfrac{\partial^2 w_0}{\partial y^2}+f(z)\cdot\dfrac{\partial \phi_y}{\partial y}\\ \dfrac{\partial u_0}{\partial y}+\dfrac{\partial v_0}{\partial x}+2[f(z)-z]\cdot\dfrac{\partial^2 w_0}{\partial x\partial y}+f(z)\cdot\left(\dfrac{\partial \phi_x}{\partial y}+\dfrac{\partial \phi_y}{\partial x}\right)\\ f'(z)\cdot\left(\dfrac{\partial w_0}{\partial y}+\phi_y\right)\\ f'(z)\cdot\left(\dfrac{\partial w_0}{\partial x}+\phi_x\right)\end{bmatrix} \tag{4}$$

Thus, from Eq. (4) a differential operator, $\boldsymbol{L}$, can be established such that $\boldsymbol{\varepsilon}=\boldsymbol{L}\boldsymbol{u}$, being $\boldsymbol{u}=\begin{bmatrix}u_0 & v_0 & w_0 & \phi_x & \phi_y\end{bmatrix}^T$,

$$\boldsymbol{L}=\begin{bmatrix}\partial/\partial x & 0 & [f(z)-z]\partial^2/\partial x^2 & f(z)\dfrac{\partial}{\partial x} & 0\\ 0 & \partial/\partial y & [f(z)-z]\partial^2/\partial y^2 & 0 & f(z)\partial/\partial y\\ \partial/\partial y & \partial/\partial x & 2[f(z)-z]\partial^2/\partial x\partial y & f(z)\partial/\partial y & f(z)\partial/\partial x\\ 0 & 0 & f'(z)\partial/\partial y & 0 & f'(z)\\ 0 & 0 & f'(z)\partial/\partial x & f'(z) & 0\end{bmatrix} \tag{5}$$

where $\boldsymbol{L}=\boldsymbol{L}(z)$, since the differential operator depends on the transverse shear function, $f(z)$, and also on its derivative, $f'(z)$. The stress field is obtained from the strain field, using the Hooke's law: $\boldsymbol{\sigma}^{(k)}=\bar{\boldsymbol{Q}}^{(k)}\boldsymbol{\varepsilon}$, with $\boldsymbol{\sigma}^{(k)}=\begin{Bmatrix}\sigma_{xx} & \sigma_{yy} & \tau_{xy} & \tau_{yz} & \tau_{xz}\end{Bmatrix}^{\mathrm{T}}$ being the stress tensor, written in Voigt notation, for the layer *k*, and $\bar{\boldsymbol{Q}}^{(k)}$ is the transformed reduced constitutive matrix for the same layer. $\bar{\boldsymbol{Q}}^{(k)}$ depends on the angle formed between the local system of coordinates, O123, (in which direction 1 is the direction of the fibres) and the global system of coordinates, *Oxyz*, represented in Fig. 2 such that: $\bar{\boldsymbol{Q}}^{(k)}=\boldsymbol{T}^T\boldsymbol{Q}^{(k)}\boldsymbol{T}$ (where $\boldsymbol{T}$ is the transformation matrix). The reduced elastic coefficients, $Q_{ij}^{(k)}$, are given by,

$$\boldsymbol{Q}^{(k)}=\begin{bmatrix}\dfrac{E_1^{(k)}}{\left(1-\upsilon_{12}^{(k)}\upsilon_{21}^{(k)}\right)} & \dfrac{\left(\upsilon_{12}^{(k)}E_2^{(k)}\right)}{\left(1-\upsilon_{12}^{(k)}\upsilon_{21}^{(k)}\right)} & 0 & 0 & 0\\ \dfrac{\left(\upsilon_{12}^{(k)}E_2^{(k)}\right)}{\left(1-\upsilon_{12}^{(k)}\upsilon_{21}^{(k)}\right)} & \dfrac{E_2^{(k)}}{\left(1-\upsilon_{12}^{(k)}\upsilon_{21}^{(k)}\right)} & 0 & 0 & 0\\ 0 & 0 & G_{12}^{(k)} & 0 & 0\\ 0 & 0 & 0 & G_{23}^{(k)} & 0\\ 0 & 0 & 0 & 0 & G_{31}^{(k)}\end{bmatrix} \tag{6}$$

where $E_1$ is the Young's modulus of the composite laminate in the direction of the fibres, $E_2$ is the Young's modulus of the in-plane transverse direction, $\upsilon_{ij}$ represents the Poisson's ratio which measures the transverse deformation – direction $j$ – related to an applied force in direction $i$ and $G_{ij}$ is the shear modulus characterizing the variation angle between directions $i$ and $j$.

### 3.2. Transverse Shear Functions and Determination of the Deformation Matrixes

The transverse shear functions considered in this work are presented in Table 1 and Fig. 3.

**Table 1** – Five high-order shear deformation theories whose formulation is used in this work.

| HSDT | $f(z)$ | $f'(z)$ |
|---|---|---|
| Levinson [38], Murthy [39] and Reddy [5] | $z\left(1-\frac{4z^2}{3h^2}\right)$ | $1-\frac{4z^2}{h^2}$ |
| Kaczkowski [40], Panc [41], Reissner [1] and Shi [6] | $\frac{5z}{4}\left(1-\frac{4z^2}{3h^2}\right)$ | $\frac{5}{4}-\frac{4z^2}{h^2}$ |
| Ambartsumian [7] | $\frac{z}{2}\left(\frac{h^2}{4}-\frac{z^2}{3}\right)$ | $\frac{h^2}{8}-\frac{z^2}{2}$ |
| Touratier [8] | $\frac{h}{\pi}\sin\left(\frac{\pi z}{h}\right)$ | $\cos\left(\frac{\pi z}{h}\right)$ |
| Mantari [11] | $\frac{h}{\pi}\left[\sin\left(\frac{\pi z}{h}\right)\cdot e^{\frac{1}{2}\cdot\cos\left(\frac{\pi z}{h}\right)}+\frac{\pi z}{2h}\right]$ | $\frac{1}{2}+e^{\frac{1}{2}\cdot\cos\left(\frac{\pi z}{h}\right)}\cdot\left[\cos\left(\frac{\pi z}{h}\right)-\frac{1}{2}\cdot\text{sen}^2\left(\frac{\pi z}{h}\right)\right]$ |

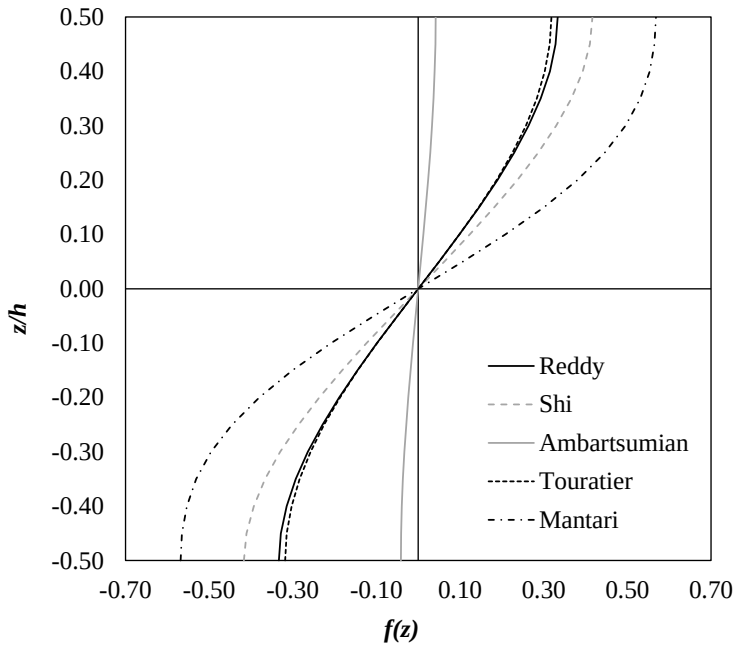


**Fig. 3** – Distribution of the transverse shear functions, $f(z)$ for different HSDTs along with the normalized thickness z/h.

In order to obtain the displacement field suggested by each HSDTs, it is only necessary to replace the functions $f(z)$ in the expressions of Eq. (2). As can be seen in Table 1, the HSDTs considered in the scope of this work have different mathematical expressions defining the variation of the in-plane displacements across the plate thickness. The first three are Third-Order Shear Deformation Theories (TSDTs) already presented in the introduction of the present section. Reddy, Shi, and Ambartsumian are formally similar, and, because of that, they can be written in a standard form, which allows an easier computational implementation. Thus, the transverse shear functions can be written as: $f(z)=a\,z+bz^3$ , being $a$ and $b$ coefficients depending on the TSDT considered:

$$\begin{aligned}
&\text{Reddy}: f(z)=z\left(1-\frac{4z^2}{3h^2}\right)=z-\frac{4z^3}{3h^2},\ \{a,b\}=\left\{1,-\frac{4}{3h^2}\right\}\\
&\text{Shi}: f(z)=\frac{5}{4}z\left(1-\frac{4z^2}{3h^2}\right)=\frac{5}{4}z-\frac{5z^3}{3h^2},\ \{a,b\}=\left\{\frac{5}{4},-\frac{5}{3h^2}\right\}\\
&\text{Ambartsumian}: f(z)=\frac{z}{2}\left(\frac{h^2}{4}-\frac{z^2}{3}\right)=\frac{h^2}{8}z-\frac{z^3}{6},\ \{a,b\}=\left\{\frac{h^2}{8},-\frac{1}{6}\right\}
\end{aligned} \tag{7}$$

Analysing the coefficients $a$ and $b$ , it can be concluded that Reddy and Shi's theories are mathematically similar. Regarding Amabrtsumian's theory, and since the representation of its transverse shear function - see Fig. 3 - is almost equal to zero for the full range of *z/h*, it seems to have some similarities to the Classical Plate Theory (CLPT) which has no transverse shear function ( $f(z)=0$).

The Touratier [8] model is also present in Table 1. It predicts the variation of the in-plane displacements along with the thickness of the plate as a trigonometric function, which can still be approximated in a unified polynomial form, as stated by Nguyen et al. [48]. The polynomial expansion of Touratier theory [44], [49] is given by:

$$\text{Touratier}: f(z)=\left(\frac{h}{\pi}\right)\sin\left(\frac{\pi z}{h}\right)=z-1.645\frac{z^3}{h^2}+0.812\frac{z^5}{h^4}-0.191\frac{z^7}{h^6}+0.0261\frac{z^9}{h^8}+... \tag{8}$$

When compared with Reddy's theory, it can be seen that the Touratier model has the same linear term coefficient and a similar coefficient for the cubic term of the polynomial. But, additionally to Reddy's theory, Touratier's plate model possesses terms with higher order than the third, which will lead to higher values for the shear stresses, as will be seen in a coming section.

The last theory presented in Table 1 is Mantari' HSDT [11], which has an exponential and a trigonometric part . The transverse shear function written in Table 1 can be generalized, being dependent on a parameter $m$ - Eq. (9).

$$\text{Mantari}: f(z)=\frac{h}{\pi}\left(\sin\left(\frac{\pi z}{h}\right)e^{m\cdot\cos\left(\frac{\pi z}{h}\right)}+\frac{\pi z}{h}m\right)\quad,\quad m\geq 0 \tag{9}$$

Mantari optimized the parameter $m$ and found that for $m=1/2$ , the difference between his results and the solutions obtained from the 3D Elasticity approach were lowered. Thus, the transverse shear function presented in Table 1 uses $m=1/2$ .

Substituting the transverse shear functions in Eq.(5), a different differential operator is obtained for each considered HSDT. As can be seen in detail in Appendix A, to obtain the stiffness matrix it is necessary to establish a deformation matrix, which is the product of the differential operator $\boldsymbol{L}(z)$ by the matrix of interpolation functions, $\boldsymbol{H}(\boldsymbol{x}_I)$: $\boldsymbol{B}(\boldsymbol{x}_I)=\boldsymbol{L}(z)\,\boldsymbol{H}(\boldsymbol{x}_I)$. The matrix of the interpolation functions at the interest point $x_1$ is given by:

$$\boldsymbol{H}_j(\boldsymbol{x}_I)=\begin{bmatrix} H_j(\boldsymbol{x}_I) & 0 & 0 & 0 & 0 \\ 0 & H_j(\boldsymbol{x}_I) & 0 & 0 & 0 \\ 0 & 0 & H_j(\boldsymbol{x}_I) & 0 & 0 \\ 0 & 0 & 0 & H_j(\boldsymbol{x}_I) & 0 \\ 0 & 0 & 0 & 0 & H_j(\boldsymbol{x}_I) \end{bmatrix}_j \quad j=\{1,2,...n\} \tag{10}$$

which is a $[5\times 5n]$ matrix since there are five independent field variables, with $n$ being the number of nodes within the 'influence-domain' of the interest point $\boldsymbol{x}_I$. Thus, established the differential operator, the deformation matrixes are easily obtained for the different HSDT considered: $\boldsymbol{B}(\boldsymbol{x}_I)\big|_{TSDT}$ (for Reddy, Shi and Amabrtsumian's theories), $\boldsymbol{B}(\boldsymbol{x}_I)\big|_{Touratier}$ (for Touratier's HSDT) and $\boldsymbol{B}(\boldsymbol{x}_I)\big|_{Mantari}$ (for Mantari's HSDT).

$$\boldsymbol{B}(\boldsymbol{x}_I)\big|_{TSDT}=\begin{bmatrix} \frac{\partial}{\partial x} & 0 & \left(az+bz^3-z\right)\frac{\partial^2}{\partial x^2} & \left(az+bz^3\right)\frac{\partial}{\partial x} & 0 \\ 0 & \frac{\partial}{\partial y} & \left(az+bz^3-z\right)\frac{\partial^2}{\partial y^2} & 0 & \left(az+bz^3\right)\frac{\partial}{\partial y} \\ \frac{\partial}{\partial y} & \frac{\partial}{\partial x} & 2\left(az+bz^3-z\right)\frac{\partial^2}{\partial x\partial y} & \left(az+bz^3\right)\frac{\partial}{\partial y} & \left(az+bz^3\right)\frac{\partial}{\partial x} \\ 0 & 0 & \left(z+3bz^2\right)\frac{\partial}{\partial y} & 0 & \left(z+3bz^2\right) \\ 0 & 0 & \left(z+3bz^2\right)\frac{\partial}{\partial x} & \left(z+3bz^2\right) & 0 \end{bmatrix}\cdot\boldsymbol{H}(\boldsymbol{x}_I) \tag{11}$$

$$\boldsymbol{B}(\boldsymbol{x}_I)\big|_{Touratier}=\begin{bmatrix} \frac{\partial}{\partial x} & 0 & \left[\frac{h}{\pi}\sin\left(\frac{\pi z}{h}\right)-z\right]\frac{\partial^2}{\partial x^2} & \frac{h}{\pi}\sin\left(\frac{\pi z}{h}\right)\frac{\partial}{\partial x} & 0 \\ 0 & \frac{\partial}{\partial y} & \left[\frac{h}{\pi}\sin\left(\frac{\pi z}{h}\right)-z\right]\frac{\partial^2}{\partial y^2} & 0 & \frac{h}{\pi}\sin\left(\frac{\pi z}{h}\right)\frac{\partial}{\partial y} \\ \frac{\partial}{\partial y} & \frac{\partial}{\partial x} & 2\left[\frac{h}{\pi}\sin\left(\frac{\pi z}{h}\right)-z\right]\frac{\partial^2}{\partial x\partial y} & \frac{h}{\pi}\sin\left(\frac{\pi z}{h}\right)\frac{\partial}{\partial y} & \frac{h}{\pi}\sin\left(\frac{\pi z}{h}\right)\frac{\partial}{\partial x} \\ 0 & 0 & \cos\left(\frac{\pi z}{h}\right)\frac{\partial}{\partial y} & 0 & \cos\left(\frac{\pi z}{h}\right) \\ 0 & 0 & \cos\left(\frac{\pi z}{h}\right)\frac{\partial}{\partial x} & \cos\left(\frac{\pi z}{h}\right) & 0 \end{bmatrix}\cdot\boldsymbol{H}(\boldsymbol{x}_I) \tag{12}$$

$$\boldsymbol{B}(\boldsymbol{x}_I)\big|_{Mantari} = \begin{bmatrix} \frac{\partial}{\partial x} & 0 & \left[\frac{z}{2}+f_1(z)-z\right]\cdot\frac{\partial^2}{\partial x^2} & \left[\frac{z}{2}+f_1(z)\right]\cdot\frac{\partial}{\partial x} & 0 \\ 0 & \frac{\partial}{\partial y} & \left[\frac{z}{2}+f_1(z)-z\right]\cdot\frac{\partial^2}{\partial y^2} & 0 & \left[\frac{z}{2}+f_1(z)\right]\cdot\frac{\partial}{\partial y} \\ \frac{\partial}{\partial y} & \frac{\partial}{\partial x} & 2\cdot\left[\frac{z}{2}+f_1(z)-z\right]\cdot\frac{\partial^2}{\partial x\partial y} & \left[\frac{z}{2}+f_1(z)\right]\cdot\frac{\partial}{\partial y} & \left[\frac{z}{2}+f_1(z)\right]\cdot\frac{\partial}{\partial x} \\ 0 & 0 & \left[\frac{1}{2}+f_2(z)\right]\cdot\frac{\partial}{\partial y} & 0 & \left[\frac{1}{2}+f_2(z)\right] \\ 0 & 0 & \left[\frac{1}{2}+f_2(z)\right]\cdot\frac{\partial}{\partial x} & \left[\frac{1}{2}+f_2(z)\right] & 0 \end{bmatrix}\cdot\boldsymbol{H}(\boldsymbol{x}_I) \tag{13}$$

where $f_1(z)=\frac{h}{\pi}\sin\left(\frac{\pi z}{h}\right)e^{\frac{1}{2}\cdot\cos\left(\frac{\pi z}{h}\right)}$ and $f_2(z)=e^{\frac{1}{2}\cdot\cos\left(\frac{\pi z}{h}\right)}\cdot\left(\cos\left(\frac{\pi z}{h}\right)-\frac{\sin^2\left(\frac{\pi z}{h}\right)}{2}\right)$.

### 3.3. Determination of the Stiffness Matrix

Using the integration scheme presented in subsection 2.2, the stiffness matrix can be obtained for a generic laminate,

$$\boldsymbol{K}=\int_{\Omega}\boldsymbol{B}^{\mathrm{T}}\boldsymbol{c}\,\boldsymbol{B}\;\mathrm{d}\Omega=\sum_{I=1}^{nG}\bar{\omega}_I\left(\sum_{k=1}^{n_k}\int_{z_{k-1}}^{z_k}\boldsymbol{B}^{\mathrm{T}}(\boldsymbol{x}_I)\,\bar{\boldsymbol{Q}}^{(k)}\boldsymbol{B}(\boldsymbol{x}_I)\,\mathrm{d}z\right) \tag{14}$$

being $nG$ the number of integration points used to integrate the stiffness matrix, $\bar{\omega}_I$ the integration weight of point $\boldsymbol{x}_I$, $n_k$ the total number of layers of the laminate, $\bar{\boldsymbol{Q}}^{(k)}$ the transformed reduced constitutive matrix of the layer $k$ obtained for the coordinate system $Oxyz$ of Fig. 2, and finally, $z_{k-1}$ and $z_k$ the coordinates $z$ of the bottom and top faces of the layer $k$.

Nevertheless, the integral (14) can be rewritten for an easier computational implementation. Thus, the deformation matrixes of Eq. (11)-(13) were divided into sub-matrixes, distinct from each other, and affected by distinct functions. For the TSDTs considered in this work, this process is exemplified below,

$$\boldsymbol{B}(\boldsymbol{x}_I)\big|_{TSDT}=\boldsymbol{B}_0+az\cdot\boldsymbol{B}_1(\boldsymbol{x}_I)+3bz^2\cdot\boldsymbol{B}_2(\boldsymbol{x}_I)+bz^3\boldsymbol{B}_3(\boldsymbol{x}_I)+(az-z)\cdot\boldsymbol{B}_4(\boldsymbol{x}_I) \tag{15}$$

where sub-.matrixes $\boldsymbol{B}_0$, $\boldsymbol{B}_1$, $\boldsymbol{B}_2$, $\boldsymbol{B}_3$ and $\boldsymbol{B}_4$ are given by,

$$\boldsymbol{B}_0^i(\boldsymbol{x}_I) = \begin{bmatrix} \dfrac{\partial \varphi_i(\boldsymbol{x}_I)}{\partial x} & 0 & 0 & 0 & 0 \\ 0 & \dfrac{\partial \varphi_i(\boldsymbol{x}_I)}{\partial y} & 0 & 0 & 0 \\ \dfrac{\partial \varphi_i(\boldsymbol{x}_I)}{\partial y} & \dfrac{\partial \varphi_i(\boldsymbol{x}_I)}{\partial x} & 0 & 0 & 0 \\ 0 & 0 & a\dfrac{\partial \varphi_i(\boldsymbol{x}_I)}{\partial y} & 0 & a\varphi_i(\boldsymbol{x}_I) \\ 0 & 0 & a\dfrac{\partial \varphi_i(\boldsymbol{x}_I)}{\partial x} & a\varphi_i(\boldsymbol{x}_I) & 0 \end{bmatrix}_i \quad i = \{1, 2, \ldots n\} \tag{16}$$

$$\boldsymbol{B}_1^i(\boldsymbol{x}_I) = \begin{bmatrix} 0 & 0 & 0 & \dfrac{\partial \varphi_i(\boldsymbol{x}_I)}{\partial x} & 0 \\ 0 & 0 & 0 & 0 & \dfrac{\partial \varphi_i(\boldsymbol{x}_I)}{\partial y} \\ 0 & 0 & 0 & \dfrac{\partial \varphi_i(\boldsymbol{x}_I)}{\partial y} & \dfrac{\partial \varphi_i(\boldsymbol{x}_I)}{\partial x} \\ 0 & 0 & 0 & 0 & 0 \\ 0 & 0 & 0 & 0 & 0 \end{bmatrix}_i \quad i = \{1, 2, \ldots n\} \tag{17}$$

$$\boldsymbol{B}_2^i(\boldsymbol{x}_I) = \begin{bmatrix} 0 & 0 & 0 & 0 & 0 \\ 0 & 0 & 0 & 0 & 0 \\ 0 & 0 & 0 & 0 & 0 \\ 0 & 0 & \dfrac{\partial \varphi_i(\boldsymbol{x}_I)}{\partial y} & 0 & \varphi_i(\boldsymbol{x}_I) \\ 0 & 0 & \dfrac{\partial \varphi_i(\boldsymbol{x}_I)}{\partial x} & \varphi_i(\boldsymbol{x}_I) & 0 \end{bmatrix}_i \quad i = \{1, 2, \ldots n\} \tag{18}$$

$$\boldsymbol{B}_3^i(\boldsymbol{x}_I) = \begin{bmatrix} 0 & 0 & \dfrac{\partial^2 \varphi_i(\boldsymbol{x}_I)}{\partial x^2} & \dfrac{\partial \varphi_i(\boldsymbol{x}_I)}{\partial x} & 0 \\ 0 & 0 & \dfrac{\partial^2 \varphi_i(\boldsymbol{x}_I)}{\partial y^2} & 0 & \dfrac{\partial \varphi_i(\boldsymbol{x}_I)}{\partial y} \\ 0 & 0 & 2\dfrac{\partial^2 \varphi_i(\boldsymbol{x}_I)}{\partial x \partial y} & \dfrac{\partial \varphi_i(\boldsymbol{x}_I)}{\partial y} & \dfrac{\partial \varphi_i(\boldsymbol{x}_I)}{\partial x} \\ 0 & 0 & 0 & 0 & 0 \\ 0 & 0 & 0 & 0 & 0 \end{bmatrix}_i \quad i = \{1, 2, \ldots n\} \tag{19}$$

$$\boldsymbol{B}_4^i(\boldsymbol{x}_I) = \begin{bmatrix} 0 & 0 & \dfrac{\partial^2 \varphi_i(\boldsymbol{x}_I)}{\partial x^2} & 0 & 0 \\ 0 & 0 & \dfrac{\partial^2 \varphi_i(\boldsymbol{x}_I)}{\partial y^2} & 0 & 0 \\ 0 & 0 & 2\dfrac{\partial^2 \varphi_i(\boldsymbol{x}_I)}{\partial x \partial y} & 0 & 0 \\ 0 & 0 & 0 & 0 & 0 \\ 0 & 0 & 0 & 0 & 0 \end{bmatrix}_i \quad i = \{1, 2, \ldots n\} \tag{20}$$

Thus, the deformation sub-matrixes do not depend on the variable $\boldsymbol{z}$, so they are put outside of the integral in Eq. (14). Therefore, the stiffness matrix can be written as follows,

$$\boldsymbol{K} = \sum_{i=0}^{4} \sum_{j=0}^{4} \boldsymbol{K}_{ij} \tag{21}$$

which represents a sum of 25 matrixes $\boldsymbol{K}_{ij}$, with $i, j = \{0,1,2,3,4\}$. The matrixes $\boldsymbol{K}_{ij}$ are given as in equation (22). This homogenization procedure consists in separately summing the integrals of the constitutive matrixes affected by the terms of Eq. (15) that depend on the variable $\boldsymbol{z}$, through the thickness of each layer. Thus, the matrixes $\boldsymbol{c}_1$ to $\boldsymbol{c}_{15}$ are homogenized constitutive matrixes and obtained as in equation (23). This process allows reducing the computational cost of the algorithm. For the remaining HSDTs, a similar method was also adopted, although it is not detailed in this work.

## 4. Final Remarks

In the first part of the research work here presented, an extensive literature review on meshless methods and plates theory was performed. It was found that HSDTs are accurate approaches to predict the displacements in composite laminates since the traction boundary condition is satisfied and they do not need shear correction factors, unlike the FSDT. Five distinct HSDTs were selected to simulate, in the second part of this work, the mechanical performance of antisymmetric angle-ply laminated plates.

In order to do so, the Radial Point Interpolation Method (RPIM) will be used as main numerical technique – the RPIM's formulation was here shown with detail. Since it uses a background nodal independent integration mesh, where the Gauss-Legendre quadrature is implemented, RPIM is not a truly meshless method. However, this classification is not a disadvantage. In fact, since the RPIM shares the same integration scheme with FEM and both methods are interpolator discrete numerical methods, RPIM and FEM can be straightforwardly combined in the same analysis. Such combination would allow to use FEM the majority of the analyzed volume and use the RPIM only in the location in which it is necessary to update the nodal distribution (such as crack opening locations or locations with stress concentrations). Since the nodal connectivity is enforced by an overlapping rule of 'influence-domains', the RPIM does not depend on re-meshing processes in problems involving large deformation or fracture mechanics, unlike the FEM.

In the next part of this work, the formulation and computer implementation explained in the last sections will be used to compute displacements and stresses in several antisymmetric angle-ply laminates subjected to bending loads.

$$\boldsymbol{K}_{00}=\sum_{I=1}^{nG}\hat{\omega}_I\cdot\sum_{k=1}^{n_k}\int_{z_{k-1}}^{z_k}\boldsymbol{B}_0^T(\boldsymbol{x}_I)\cdot\bar{\boldsymbol{Q}}^{(k)}\cdot\boldsymbol{B}_0(\boldsymbol{x}_I)\,\mathrm{d}z=\sum_{I=1}^{nG}\hat{\omega}_I\cdot\boldsymbol{B}_0^T(\boldsymbol{x}_I)\cdot\boldsymbol{c}_1\cdot\boldsymbol{B}_0(\boldsymbol{x}_I)$$

$$\boldsymbol{K}_{01}=\sum_{I=1}^{nG}\hat{\omega}_I\cdot\sum_{k=1}^{n_k}\int_{z_{k-1}}^{z_k}\boldsymbol{B}_0^T(\boldsymbol{x}_I)\cdot\bar{\boldsymbol{Q}}^{(k)}\cdot k_1\cdot z\cdot\boldsymbol{B}_1(\boldsymbol{x}_I)\,\mathrm{d}z=\sum_{I=1}^{nG}\hat{\omega}_I\cdot\boldsymbol{B}_0^T(\boldsymbol{x}_I)\cdot\boldsymbol{c}_2\cdot\boldsymbol{B}_0(\boldsymbol{x}_I)=\boldsymbol{K}_{10}$$

$$\boldsymbol{K}_{02}=\sum_{I=1}^{nG}\hat{\omega}_I\cdot\sum_{k=1}^{n_k}\int_{z_{k-1}}^{z_k}\boldsymbol{B}_0^T(\boldsymbol{x}_I)\cdot\bar{\boldsymbol{Q}}^{(k)}\cdot 3k_2\,z^2\cdot\boldsymbol{B}_2(\boldsymbol{x}_I)\,\mathrm{d}z=\sum_{I=1}^{nG}\hat{\omega}_I\cdot\boldsymbol{B}_0^T(\boldsymbol{x}_I)\cdot\boldsymbol{c}_3\cdot\boldsymbol{B}_0(\boldsymbol{x}_I)=\boldsymbol{K}_{20}$$

$$\boldsymbol{K}_{03}=\sum_{I=1}^{nG}\hat{\omega}_I\cdot\sum_{k=1}^{n_k}\int_{z_{k-1}}^{z_k}\boldsymbol{B}_0^T(\boldsymbol{x}_I)\cdot\bar{\boldsymbol{Q}}^{(k)}\cdot k_2\,z^3\cdot\boldsymbol{B}_3(\boldsymbol{x}_I)\mathrm{d}z=\sum_{I=1}^{nG}\hat{\omega}_I\cdot\boldsymbol{B}_0^T(\boldsymbol{x}_I)\cdot\boldsymbol{c}_4\cdot\boldsymbol{B}_3(\boldsymbol{x}_I)=\boldsymbol{K}_{30}$$

$$\boldsymbol{K}_{04}=\sum_{I=1}^{nG}\hat{\omega}_I\cdot\sum_{k=1}^{n_k}\int_{z_{k-1}}^{z_k}\boldsymbol{B}_0^T(\boldsymbol{x}_I)\cdot\bar{\boldsymbol{Q}}^{(k)}\cdot(k_1z-z)\cdot\boldsymbol{B}_4(\boldsymbol{x}_I)\mathrm{d}z=\sum_{I=1}^{nG}\hat{\omega}_I\cdot\boldsymbol{B}_0^T(\boldsymbol{x}_I)\cdot\boldsymbol{c}_5\cdot\boldsymbol{B}_4(\boldsymbol{x}_I)=\boldsymbol{K}_{40}$$

$$\boldsymbol{K}_{11}=\sum_{I=1}^{nG}\hat{\omega}_I\cdot\sum_{k=1}^{n_k}\int_{z_{k-1}}^{z_k}\boldsymbol{B}_1^T(\boldsymbol{x}_I)\cdot\bar{\boldsymbol{Q}}^{(k)}\cdot(k_1z)^2\cdot\boldsymbol{B}_1(\boldsymbol{x}_I)\mathrm{d}z=\sum_{I=1}^{nG}\hat{\omega}_I\cdot\boldsymbol{B}_1^T(\boldsymbol{x}_I)\cdot\boldsymbol{c}_6\cdot\boldsymbol{B}_1(\boldsymbol{x}_I)$$

$$\boldsymbol{K}_{12}=\sum_{I=1}^{nG}\hat{\omega}_I\cdot\sum_{k=1}^{n_k}\int_{z_{k-1}}^{z_k}\boldsymbol{B}_1^T(\boldsymbol{x}_I)\cdot\bar{\boldsymbol{Q}}^{(k)}\cdot(k_1z)\cdot(3k_2z^2)\cdot\boldsymbol{B}_2(\boldsymbol{x}_I)\,\mathrm{d}z=\sum_{I=1}^{nG}\hat{\omega}_I\cdot\boldsymbol{B}_1^T(\boldsymbol{x}_I)\cdot\boldsymbol{c}_7\cdot\boldsymbol{B}_2(\boldsymbol{x}_I)=\boldsymbol{K}_{21}$$

$$\boldsymbol{K}_{13}=\sum_{I=1}^{nG}\hat{\omega}_I\cdot\sum_{k=1}^{n_k}\int_{z_{k-1}}^{z_k}\boldsymbol{B}_1^T(\boldsymbol{x}_I)\cdot\bar{\boldsymbol{Q}}^{(k)}\cdot(k_1z)\cdot(k_2z^3)\cdot\boldsymbol{B}_3(\boldsymbol{x}_I)\mathrm{d}z=\sum_{I=1}^{nQ}\hat{\omega}_I\cdot\boldsymbol{B}_1^T(\boldsymbol{x}_I)\cdot\boldsymbol{c}_8\cdot\boldsymbol{B}_3(\boldsymbol{x}_I)=\boldsymbol{K}_{31}\tag{22}$$

$$\boldsymbol{K}_{14}=\sum_{I=1}^{nG}\hat{\omega}_I\cdot\sum_{k=1}^{n_k}\int_{z_{k-1}}^{z_k}\boldsymbol{B}_1^T(\boldsymbol{x}_I)\cdot\bar{\boldsymbol{Q}}^{(k)}\cdot k_1z\cdot(k_1z-z)\cdot\boldsymbol{B}_4(\boldsymbol{x}_I)\mathrm{d}z=\sum_{I=1}^{nG}\hat{\omega}_I\cdot\boldsymbol{B}_1^T(\boldsymbol{x}_I)\cdot\boldsymbol{c}_9\cdot\boldsymbol{B}_4(\boldsymbol{x}_I)=\boldsymbol{K}_{41}$$

$$\boldsymbol{K}_{22}=\sum_{I=1}^{nG}\hat{\omega}_I\cdot\sum_{k=1}^{n_k}\int_{z_{k-1}}^{z_k}\boldsymbol{B}_2^T(\boldsymbol{x}_I)\cdot\bar{\boldsymbol{Q}}^{(k)}\cdot(3k_2z^2)^2\cdot\boldsymbol{B}_2(\boldsymbol{x}_I)\mathrm{d}z=\sum_{I=1}^{nG}\hat{\omega}_I\cdot\boldsymbol{B}_2^T(\boldsymbol{x}_I)\cdot\boldsymbol{c}_{10}\cdot\boldsymbol{B}_2(\boldsymbol{x}_I)$$

$$\boldsymbol{K}_{23}=\sum_{I=1}^{nG}\hat{\omega}_I\cdot\sum_{k=1}^{n_k}\int_{z_{k-1}}^{z_k}\boldsymbol{B}_2^T(\boldsymbol{x}_I)\cdot\bar{\boldsymbol{Q}}^{(k)}\cdot(3k_2z^2\cdot k_2z^3)\cdot\boldsymbol{B}_3(\boldsymbol{x}_I)\,\mathrm{d}z=\sum_{I=1}^{nG}\hat{\omega}_I\cdot\boldsymbol{B}_2^T(\boldsymbol{x}_I)\cdot\boldsymbol{c}_{11}\cdot\boldsymbol{B}_3(\boldsymbol{x}_I)=\boldsymbol{K}_{32}$$

$$\boldsymbol{K}_{24}=\sum_{I=1}^{nG}\hat{\omega}_I\cdot\sum_{k=1}^{n_k}\int_{z_{k-1}}^{z_k}\boldsymbol{B}_2^T(\boldsymbol{x}_I)\cdot\bar{\boldsymbol{Q}}^{(k)}\cdot\left[3k_2z^2\cdot(k_1z-z)\right]\cdot\boldsymbol{B}_4(\boldsymbol{x}_I)\,\mathrm{d}z=\sum_{I=1}^{nG}\hat{\omega}_I\cdot\boldsymbol{B}_2^T(\boldsymbol{x}_I)\cdot\boldsymbol{c}_{12}\cdot\boldsymbol{B}_4(\boldsymbol{x}_I)=\boldsymbol{K}_{42}$$

$$\boldsymbol{K}_{33}=\sum_{I=1}^{nG}\hat{\omega}_I\cdot\sum_{k=1}^{n_k}\int_{z_{k-1}}^{z_k}\boldsymbol{B}_3^T(\boldsymbol{x}_I)\cdot\bar{\boldsymbol{Q}}^{(k)}\cdot(k_2z^3)^2\cdot\boldsymbol{B}_3(\boldsymbol{x}_I)\mathrm{d}z=\sum_{I=1}^{nG}\hat{\omega}_I\cdot\boldsymbol{B}_3^T(\boldsymbol{x}_I)\cdot\boldsymbol{c}_{12}\cdot\boldsymbol{B}_3(\boldsymbol{x}_I)$$

$$\boldsymbol{K}_{34}=\sum_{I=1}^{nG}\hat{\omega}_I\cdot\sum_{k=1}^{n_k}\int_{z_{k-1}}^{z_k}\boldsymbol{B}_3^T(\boldsymbol{x}_I)\cdot\bar{\boldsymbol{Q}}^{(k)}\cdot\left[k_2z^3\cdot(k_1z-z)\right]\cdot\boldsymbol{B}_4(\boldsymbol{x}_I)\mathrm{d}z=\sum_{I=1}^{nG}\hat{\omega}_I\cdot\boldsymbol{B}_3^T(\boldsymbol{x}_I)\cdot\boldsymbol{c}_{14}\cdot\boldsymbol{B}_4(\boldsymbol{x}_I)=\boldsymbol{K}_{43}$$

$$\boldsymbol{K}_{44}=\sum_{I=1}^{nG}\hat{\omega}_I\cdot\sum_{k=1}^{n_k}\int_{z_{k-1}}^{z_k}\boldsymbol{B}_4^T(\boldsymbol{x}_I)\cdot\bar{\boldsymbol{Q}}^{(k)}\cdot\left[(k_1z-z)\cdot(k_1z-z)\right]\cdot\boldsymbol{B}_4(\boldsymbol{x}_I)\mathrm{d}z=\sum_{I=1}^{nG}\hat{\omega}_I\cdot\boldsymbol{B}_4^T(\boldsymbol{x}_I)\cdot\boldsymbol{c}_{15}\cdot\boldsymbol{B}_4(\boldsymbol{x}_I)$$

$$\boldsymbol{c}_1 = \sum_{k=1}^{n_k} \int_{z_{k-1}}^{z_k} \bar{\boldsymbol{Q}}^{(k)} \mathrm{d}\, z = \sum_{k=1}^{n_k} \left( z_k - z_{k-1} \right) \cdot \bar{\boldsymbol{Q}}^{(k)}$$

$$\boldsymbol{c}_2 = \sum_{k=1}^{n_k} \int_{z_{k-1}}^{z_k} \bar{\boldsymbol{Q}}^{(k)} \cdot a\, z \,\mathrm{d}\, z = k_1 \cdot \sum_{k=1}^{n_k} \left( \frac{{z_k}^2}{2} - \frac{{z_{k-1}}^2}{2} \right) \cdot \bar{\boldsymbol{Q}}^{(k)}$$

$$\boldsymbol{c}_3 = \sum_{k=1}^{n_k} \int_{z_{k-1}}^{z_k} \bar{\boldsymbol{Q}}^{(k)} \cdot 3b\, z^2 \,\mathrm{d}\, z = 3b \cdot \sum_{k=1}^{n_k} \left( \frac{{z_k}^3}{3} - \frac{{z_{k-1}}^3}{3} \right) \cdot \bar{\boldsymbol{Q}}^{(k)}$$

$$\boldsymbol{c}_4 = \sum_{k=1}^{n_k} \int_{z_{k-1}}^{z_k} \bar{\boldsymbol{Q}}^{(k)} \cdot b\, z^3 \,\mathrm{d}z = b \cdot \sum_{k=1}^{n_k} \left( \frac{{z_k}^4}{4} - \frac{{z_{k-1}}^4}{4} \right) \cdot \bar{\boldsymbol{Q}}^{(k)}$$

$$\boldsymbol{c}_5 = \sum_{k=1}^{n_k} \int_{z_{k-1}}^{z_k} \bar{\boldsymbol{Q}}^{(k)} \cdot (a\, z - z) \,\mathrm{d}\, z = (a-1) \cdot \sum_{k=1}^{n_k} \left( \frac{{z_k}^2}{2} - \frac{{z_{k-1}}^2}{2} \right) \cdot \bar{\boldsymbol{Q}}^{(k)}$$

$$\boldsymbol{c}_6 = \sum_{k=1}^{n_k} \int_{z_{k-1}}^{z_k} \bar{\boldsymbol{Q}}^{(k)} \cdot \left( a\, z \right)^2 \mathrm{d}\, z = a^2 \cdot \sum_{k=1}^{n_k} \left( \frac{{z_k}^3}{3} - \frac{{z_{k-1}}^3}{3} \right) \bar{\boldsymbol{Q}}^{(k)}$$

$$\boldsymbol{c}_7 = \sum_{k=1}^{n_k} \int_{z_{k-1}}^{z_k} \bar{\boldsymbol{Q}}^{(k)} \cdot (a\, z) \cdot (3b\, z^2) \,\mathrm{d}\, z = 3ab \cdot \sum_{k=1}^{n_k} \left( \frac{{z_k}^4}{4} - \frac{{z_{k-1}}^4}{4} \right) \cdot \bar{\boldsymbol{Q}}^{(k)}$$

$$\boldsymbol{c}_8 = \sum_{k=1}^{n_k} \int_{z_{k-1}}^{z_k} \bar{\boldsymbol{Q}}^{(k)} \cdot (a\, z) \cdot (b\, z^3) \,\mathrm{d}\, z = a \cdot b \cdot \sum_{k=1}^{n_k} \left( \frac{{z_k}^5}{5} - \frac{{z_{k-1}}^5}{5} \right) \cdot \bar{\boldsymbol{Q}}^{(k)} \tag{23}$$

$$\boldsymbol{c}_9 = \sum_{k=1}^{n_k} \int_{z_{k-1}}^{z_k} \bar{\boldsymbol{Q}}^{(k)} \cdot a\, z \cdot (a\, z - z) \,\mathrm{d}\, z = a \cdot (a-1) \cdot \sum_{k=1}^{n_k} \left( \frac{{z_k}^3}{3} - \frac{{z_{k-1}}^3}{3} \right) \cdot \bar{\boldsymbol{Q}}_k^{(k)}$$

$$\boldsymbol{c}_{10} = \sum_{k=1}^{n_k} \int_{z_{k-1}}^{z_k} \bar{\boldsymbol{Q}}^{(k)} \cdot \left( 3b\, z^2 \right)^2 \mathrm{d}\, z = 9b^2 \cdot \sum_{k=1}^{n_k} \left( \frac{{z_k}^5}{5} - \frac{{z_{k-1}}^5}{5} \right) \cdot \bar{\boldsymbol{Q}}_k^{(k)}$$

$$\boldsymbol{c}_{11} = \sum_{k=1}^{n_k} \int_{z_{k-1}}^{z_k} \bar{\boldsymbol{Q}}^{(k)} \cdot \left( 3b\, z^2 \cdot b\, z^3 \right) \mathrm{d}\, z = 3b^2 \cdot \sum_{k=1}^{n_k} \left( \frac{{z_k}^6}{6} - \frac{{z_{k-1}}^6}{6} \right) \cdot \bar{\boldsymbol{Q}}^{(k)}$$

$$\boldsymbol{c}_{12} = \sum_{k=1}^{n_k} \int_{z_{k-1}}^{z_k} \bar{\boldsymbol{Q}}^{(k)} \cdot 3b\, z^2 \cdot (a\, z - z) \,\mathrm{d}\, z = 3b(a-1) \cdot \sum_{k=1}^{n_k} \left( \frac{{z_k}^6}{6} - \frac{{z_{k-1}}^6}{6} \right) \cdot \bar{\boldsymbol{Q}}^{(k)}$$

$$\boldsymbol{c}_{13} = \sum_{k=1}^{n_k} \int_{z_{k-1}}^{z_k} \bar{\boldsymbol{Q}}^{(k)} \cdot \left( b\, z^3 \right)^2 \mathrm{d}\, z = b^2 \cdot \sum_{k=1}^{n_k} \left( \frac{{z_k}^7}{7} - \frac{{z_{k-1}}^7}{7} \right) \cdot \bar{\boldsymbol{Q}}^{(k)}$$

$$\boldsymbol{c}_{14} = \sum_{k=1}^{n_k} \int_{z_{k-1}}^{z_k} \bar{\boldsymbol{Q}}^{(k)} \cdot b\, z^3 \cdot (az - z) \,\mathrm{d}\, z = b \cdot (a-1) \cdot \sum_{k=1}^{n_k} \left( \frac{{z_k}^5}{5} - \frac{{z_{k-1}}^5}{5} \right) \cdot \bar{\boldsymbol{Q}}^{(k)}$$

$$\boldsymbol{c}_{15} = \sum_{k=1}^{n_k} \int_{z_{k-1}}^{z_k} \bar{\boldsymbol{Q}}^{(k)} \cdot (az - z) \cdot (az - z) \,\mathrm{d}\, z = (a-1) \cdot (a-1) \cdot \sum_{k=1}^{n_k} \left( \frac{{z_k}^3}{3} - \frac{{z_{k-1}}^3}{3} \right) \cdot \bar{\boldsymbol{Q}}^{(k)}$$

## Acknowledgements and Funding

The authors acknowledge the funding provided by Ministério da Ciência, Tecnologia e Ensino Superior - Fundação para a Ciência e a Tecnologia (Portugal) and LAETA, under internal project UIDB/50022/2020.

## References


[1] E. Reissner, "On the theory of transverse bending of elastic plates," *Int. J. Solids Struct.*, vol. 12, no. 8, pp. 545–554, 1976.

[2] E. Reissner, "A consistent treatment of transverse shear deformations in laminated anisotropic plates," *AIAA J.*, vol. 10, no. 5, pp. 716–718, 1972, doi: http://dx.doi.org/10.2514/3.50194.

[3] E. Reissner, "The effect of transverse shear deformations on the bending of elastic plates," *J. Appl. Mech*, vol. 12, pp. A69–A77, 1945.

[4] R. D. Mindlin, "Influence of Rotatory Inertia and Shear on Flexural Motions of Isotropic, Elastic Plates," *J. Appl. Mech.*, no. 18, pp. 31–38, 1951.

[5] J.N. Reddy, "Mechanics of laminated composite plates and shells: theory and analysis." CRC Press LLC, Boca Raton, Florida, 2004, doi: 10.1007/978-1-4471-0095-9.

[6] G. Shi, "A new simple third-order shear deformation theory of plates," *Int. J. Solids Struct.*, vol. 44, no. 13, pp. 4399–4417, 2007, doi: 10.1016/j.ijsolstr.2006.11.031.

[7] S. A. Ambartsumian, "On the theory of bending of anisotropic plates and shallow shells," *J. Appl. Math. Mech.*, vol. 24, no. 2, pp. 500–514, Jan. 1960, doi: 10.1016/0021-8928(60)90052-6.

[8] M. Touratier, "An efficient standard plate theory," *Int. J. Eng. Sci.*, vol. 29, no. 8, pp. 901–916, 1991.

[9] K. P. Soldatos, "A transverse shear deformation theory for homogeneous monoclinic plates," *Acta Mech.*, vol. 94, no. 3–4, pp. 195–220, 1992.

[10] N. El, A. Tounsi, N. Ziane, I. Mechab, E. Abbes, and A. Bedia, "A new hyperbolic shear deformation theory for buckling and vibration of functionally graded sandwich plate," *Int. J. Mech. Sci.*, vol. 53, no. 4, pp. 237–247, 2011, doi: 10.1016/j.ijmecsci.2011.01.004.

[11] J. L. Mantari, A. S. Oktem, and C. Guedes Soares, "A new higher order shear deformation theory for sandwich and composite laminated plates," *Compos. Part B Eng.*, vol. 43, no. 3, pp. 1489–1499, 2012, doi: 10.1016/j.compositesb.2011.07.017.

[12] a J. M. Ferreira, "Analysis of Composite Plates Using a Layerwise Theory and Multiquadrics Discretization," *Mech. Adv. Mater. Struct.*, vol. 12, no. 2, pp. 99–112, 2005, [Online]. Available: http://dx.doi.org/10.1080/15376490490493952.

[13] L. Iurlaro, M. Gherlone, M. Di Sciuva, and A. Tessler, "Refined Zigzag Theory for laminated composite and sandwich plates derived from Reissner's Mixed Variational Theorem," *Compos. Struct.*, vol. 133, pp. 809–817, 2015, doi: 10.1016/j.compstruct.2015.08.004.

[14] E. Viola, F. Tornabene, and N. Fantuzzi, "General higher-order shear deformation theories for the free vibration analysis of completely doubly-curved laminated shells and panels," *Compos. Struct.*, vol. 95, pp. 639–666, 2013, doi: https://doi.org/10.1016/j.compstruct.2012.08.005.

[15] E. Viola, F. Tornabene, and N. Fantuzzi, "Static analysis of completely doubly-curved laminated shells and panels using general higher-order shear deformation theories," *Compos. Struct.*, vol. 101, pp. 59–93, 2013, doi: https://doi.org/10.1016/j.compstruct.2013.01.002.

[16] F. Tornabene, E. Viola, and N. Fantuzzi, "General higher-order equivalent single layer theory for free vibrations of doubly-curved laminated composite shells and panels," *Compos. Struct.*, vol. 104, pp. 94–117, 2013, doi: https://doi.org/10.1016/j.compstruct.2013.04.009.

[17] F. Tornabene, N. Fantuzzi, and M. Bacciocchi, "The local GDQ method applied to general higher-order theories of doubly-curved laminated composite shells and panels: The free vibration analysis," *Compos. Struct.*, vol. 116, pp. 637–660, 2014, doi: https://doi.org/10.1016/j.compstruct.2014.05.008.

[18] J. Belinha, *Meshless Methods in Biomechanics: Bone Tissue Remodelling Analysis*. Porto: Springer International Publishing, 2014.

[19] J. Belinha, A. L. Araújo, A. J. M. Ferreira, L. M. J. S. Dinis, and R. M. N. Jorge, "The analysis of laminated plates using distinct advanced discretization meshless techniques," *Compos. Struct.*, vol. 143, pp. 165–179, 2016, doi: 10.1016/j.compstruct.2016.02.021.

[20] J. G. Wang and G. R. Liu, "A point interpolation meshless method based on radial basis functions," *Int. J. Numer. Methods Eng.*, vol. 54, no. 11, pp. 1623–1648, 2002.

[21] S. N. Atluri and T. Zhu, "A new Meshless Local Petrov-Galerkin (MLPG) approach in computational mechanics," *Comput. Mech.*, vol. 22, no. 2, pp. 117–127, 1998.

[22] W. K. Liu, S. Jun, S. Li, J. Adee, and T. Belytschko, "Reproducing kernel particle methods for structural dynamics," *Int. J. Numer. Methods Eng.*, vol. 38, no. 10, pp. 1655–1679, 1995, doi: 10.1002/nme.1620381005.

[23] E. Oñate, S. Idelsohn, O. C. Zienkiewicz, and R. L. Taylor, "A finite point method in computational mechanics. Applications to convective transport and fluid flow," *Int. J. Numer. Methods Eng.*, vol. 39, no. December 1995, pp. 3839–3866, 1996.

[24] G. R. Liu and Y. T. Gu, "A point interpolation method for two-dimensional solids," *Int. J. Numer. Methods Eng.*, vol. 50, no. 4, pp. 937–951, 2001.

[25] R. A. Gingold and J. J. Monaghan, "Smoothed particle hydrodynamics: theory and application to non-spherical stars," *Mon. Not. R. Astron. Soc.*, vol. 181, no. 3, pp. 375–389, 1977, doi: 10.1093/mnras/181.3.375.

[26] T. Belytschko, Y. Y. Lu, and L. Gu, "Element-free Galerkin methods," *International Journal for Numerical Methods in*

*Engineering*, vol. 37, no. 2. pp. 229–256, 1994, doi: 10.1002/nme.1620370205.
[27] J. N. . R. M. Noronha, J.; Belinha, J., Dinis, L., "The Numerical Analysis of Airplane Windshields due to Bird Strike: A Static Study," *Fac. Eng. Univ. Porto*, 2016.
[28] B. Nayroles, G. Touzot, and P. Villon, "Generalizing the finite element method: Diffuse approximation and diffuse elements," *Comput. Mech.*, vol. 10, no. 5, pp. 307–318, 1992, doi: 10.1007/BF00364252.
[29] J. Belinha, L. M. J. S. Dinis, and R. M. N. Jorge, "The Natural Neighbour Radial Point Interpolation Method: Solid Mechanics and Mechanobiology Applications," *Fac. Eng. da Univ. do Porto*, 2010.
[30] G. R. Liu, "A point assembly method for stress analysis for two-dimensional solids," *Int. J. Solids Struct.*, vol. 39, no. 1, pp. 261–276, 2001.
[31] N. Sukumar, B. Moran, and T. Belytschko, "The natural element method in solid mechanics," *Int. J. Numer. Methods Eng.*, vol. 43, no. 5, pp. 839–887, 1998, doi: 10.1002/(SICI)1097-0207(19981115)43:5<839::AID-NME423>3.0.CO;2-R.
[32] S. De and K. J. Bathe, "The method of finite spheres," *Comput. Mech.*, vol. 25, no. 4, pp. 329–345, 2000, doi: 10.1007/s004660050481.
[33] I. S. R., O. Eugenio, C. Nestor, and D. P. Facundo, "The meshless finite element method," *Int. J. Numer. Methods Eng.*, vol. 58, no. 6, pp. 893–912, Jul. 2003, doi: 10.1002/nme.798.
[34] J. N. Reddy, "A refined nonlinear theory of plates with transverse shear deformation," *Int. J. Solids Struct.*, vol. 20, no. 9–10, pp. 881–896, 1984.
[35] T. Kant, "Numerical analysis of thick plates," *Comput. Methods Appl. Mech. Eng.*, vol. 31, no. 1, pp. 1–18, 1982, doi: https://doi.org/10.1016/0045-7825(82)90043-3.
[36] T. Kant, D. R. J. Owen, and O. C. Zienkiewicz, "A refined higher-order C° plate bending element," *Comput. Struct.*, vol. 15, no. 2, pp. 177–183, 1982, doi: 10.1016/0045-7949(82)90065-7.
[37] B. N. Pandya and T. Kant, "A refined higher-order generally orthotropic C0 plate bending element," *Comput. Struct.*, vol. 28, no. 2, pp. 119–133, 1988, doi: 10.1016/0045-7949(88)90031-4.
[38] M. Levinson, "An accurate simple theory of the statics and dynamics of elastic plates," *Mech. Res. Commun*, no. 7, pp. 343–350, 1980.
[39] M. V. V. Murthy, "An improved transverse shear deformation theory for laminated anisotropic plates," *NASA Tech. Pap. 1903*, no. November, 1981.
[40] Z. Kaczkowski, *Plates. In Statical calculations*. Warszawa (in Polish): Arkady, 1968.
[41] V. Panc, *Theories of elastic plates*, 1st ed. Prague: Academia, 1975.
[42] H. Nguyen-Xuan, C. H. Thai, and T. Nguyen-Thoi, "Isogeometric finite element analysis of composite sandwich plates using a higher order shear deformation theory," *Compos. Part B Eng.*, vol. 55, pp. 558–574, 2013.
[43] J. L. Mantari, A. S. Oktem, and C. G. Soares, "Static and dynamic analysis of laminated composite and sandwich plates and shells by using a new higher-order shear deformation theory," *Compos. Struct.*, vol. 94, no. 1, pp. 37–49, 2011, doi: 10.1016/j.compstruct.2011.07.020.
[44] M. Karama, K. S. Afaq, and S. Mistou, "A new theory for laminated composite plates," *Proc. Inst. Mech. Eng. Part L J. Mater. Des. Appl.*, vol. 223, no. 2, pp. 53–62, 2009, doi: 10.1243/14644207JMDA189.
[45] M. Aydogdu, "A new shear deformation theory for laminated composite plates," *Compos. Struct. J.*, no. 89, pp. 94–101, 2008.
[46] N. Grover, B. N. Singh, and D. K. Maiti, "New Nonpolynomial Shear-Deformation Theories for Structural Behavior of Laminated-Composite and Sandwich Plates," *AIAA J.*, vol. 51, no. 8, pp. 1861–1871, 2013, [Online]. Available: http://arc.aiaa.org/doi/abs/10.2514/1.J052399.
[47] K. P. Soldatos, "A transverse shear deformation theory for homogeneous monoclinic plates," *Acta Mech.*, 1992, doi: 10.1007/BF01176650.
[48] T. N. Nguyen, C. H. Thai, and H. Nguyen-Xuan, "On the general framework of high order shear deformation theories for laminated composite plate structures: A novel unified approach," *Int. J. Mech. Sci.*, vol. 110, pp. 242–255, 2016, doi: 10.1016/j.ijmecsci.2016.01.012.
[49] A. Idlbi, M. Karama, and M. Touratier, "Comparison of various laminated plate theories," *Compos. Struct.*, vol. 37, no. 2, pp. 173–184, 1997, [Online]. Available: http://www.sciencedirect.com/science/article/pii/S0263822397800104.
[50] L. M. J. S. Dinis, R. M. Natal Jorge, and J. Belinha, "Analysis of plates and laminates using the natural neighbour radial point interpolation method," *Eng. Anal. Bound. Elem.*, vol. 32, no. 3, pp. 267–279, 2008, doi: 10.1016/j.enganabound.2007.08.006.

## Appendix A - Meshless discrete system of equations

The RPIM uses the Galerkin weak form formulation to obtain the discrete system of equations ruling the problem. The Galerkin weak is determined minimizing the Lagrangian functional written for a generic solid with domain $\Omega$ and boundary $\Gamma$, that contain all physical information about the problem and the forces acting on it:

$$\delta\int_{t_1}^{t_2}\left[\frac{1}{2}\int_{\Omega}\rho\dot{\boldsymbol{u}}^{\mathrm{T}}\dot{\boldsymbol{u}}\,\mathrm{d}\Omega-\frac{1}{2}\int_{\Omega}\boldsymbol{\varepsilon}^{\mathrm{T}}\boldsymbol{\sigma}\,\mathrm{d}\Omega+\int_{\Omega}\boldsymbol{u}^{\mathrm{T}}\boldsymbol{b}\,\mathrm{d}\Omega+\int_{\Gamma_{\mathrm{t}}}\boldsymbol{u}^{\mathrm{T}}\bar{\boldsymbol{t}}\,\mathrm{d}\Gamma\right]\mathrm{d}t=0 \tag{24}$$

being $\dot{\boldsymbol{u}}$ the velocity, $\rho$ the solid mass density, $\boldsymbol{\varepsilon}$ the strain tensor, $\boldsymbol{\sigma}$ the stress tensor, $\boldsymbol{u}$ the displacements vector, $\boldsymbol{b}$ the body forces, $\Gamma\in\Omega$ the traction boundary where the external forces $\bar{\boldsymbol{t}}$ are applied and $t_1$ and $t_2$ any initial and final time, respectively. The work here described only concerns static analysis, thus, the first term of the integrand in Eq. (24) is discarded:

$$\delta\int_{t_1}^{t_2}\left[-\frac{1}{2}\int_{\Omega}\boldsymbol{\varepsilon}^{\mathrm{T}}\boldsymbol{\sigma}\,\mathrm{d}\Omega+\int_{\Omega}\boldsymbol{u}^{\mathrm{T}}\boldsymbol{b}\,\mathrm{d}\Omega+\int_{\Gamma_{\mathrm{t}}}\boldsymbol{u}^{\mathrm{T}}\bar{\boldsymbol{t}}\,\mathrm{d}\Gamma\right]\mathrm{d}t=0 \tag{25}$$

Moving the variation operator $\delta$ inside the integrals,

$$\int_{t_1}^{t_2}\left[-\frac{1}{2}\int_{\Omega}\delta\left(\boldsymbol{\varepsilon}^{\mathrm{T}}\boldsymbol{\sigma}\right)\mathrm{d}\Omega+\int_{\Omega}\delta\boldsymbol{u}^{\mathrm{T}}\boldsymbol{b}\,\mathrm{d}\Omega+\int_{\Gamma_{\mathrm{t}}}\delta\boldsymbol{u}^{\mathrm{T}}\bar{\boldsymbol{t}}\,\mathrm{d}\Gamma\right]\mathrm{d}t=0 \tag{26}$$

Considering that, for the Eq. (26) be satisfied for all possible $\boldsymbol{u}$ and for any initial and final time, $t_1$ and $t_2$, the integrand must be null, the 'Galerkin weak form' is established,

$$\int_{\Omega}\delta\boldsymbol{\varepsilon}^{\mathrm{T}}\boldsymbol{\sigma}\,\mathrm{d}\Omega=\int_{\Omega}\delta\boldsymbol{u}^{\mathrm{T}}\boldsymbol{b}\,\mathrm{d}\Omega+\int_{\Gamma_{\mathrm{t}}}\delta\boldsymbol{u}^{\mathrm{T}}\bar{\boldsymbol{t}}\,\mathrm{d}\Gamma \tag{27}$$

being $\delta\boldsymbol{\varepsilon}$ the virtual strain tensor and $\delta\boldsymbol{u}$ the virtual displacement. The discrete system of equations is established from Eq. (27) by introducing the stress-strain relation, $\boldsymbol{\sigma}=\boldsymbol{c}\boldsymbol{\varepsilon}$ (being $\boldsymbol{c}$ is the constitutive matrix), the linear relation between strains and displacements: $\boldsymbol{\varepsilon}=\boldsymbol{L}\boldsymbol{u}$ (being $\boldsymbol{L}$ the differential operator established in **Erro! A origem da referência não foi encontrada.** and $\boldsymbol{u}=\left\{u_0\ v_0\ w_0\ \phi_x\ \phi_y\right\}^T$) and also the equations of interpolation: $u(\boldsymbol{x}_{\mathrm{I}})=\sum_{j=1}^{n}\varphi_j(\boldsymbol{x}_{\mathrm{I}})\,\boldsymbol{u}_j$ and $\delta u(\boldsymbol{x}_{\mathrm{I}})=\sum_{j=1}^{n}\varphi_j(\boldsymbol{x}_{\mathrm{I}})\,\delta\boldsymbol{u}_j$. From those considerations, the concept of deformation matrix is found: $\boldsymbol{B}(\boldsymbol{x}_{\mathrm{I}})=\sum_{j=1}^{\mathrm{n}}\boldsymbol{L}\varphi_j(\boldsymbol{x}_{\mathrm{I}})$, such as $\boldsymbol{\varepsilon}(\boldsymbol{x}_{\mathrm{I}})=\boldsymbol{B}(\boldsymbol{x}_{\mathrm{I}})\boldsymbol{u}_{\mathrm{i}}$, being $\boldsymbol{u}_{\mathrm{i}}$ the vector contain the nodal values. Thus, the discrete system of equations is obtained,

$$\int_{\Omega}\boldsymbol{B}^{\mathrm{T}}\,\boldsymbol{c}\,\boldsymbol{B}\,d\Omega\cdot\boldsymbol{u}=\int_{\Omega}\boldsymbol{H}\,\boldsymbol{b}\,d\Omega+\int_{\Gamma}\boldsymbol{H}\,\bar{\boldsymbol{t}}\,d\Gamma \tag{28}$$

where matrix $\boldsymbol{H}$ is the same that was introduced in subsection 3.2. Eq. (28) can be written in a standard form:

$$\boldsymbol{K}\cdot\boldsymbol{u}=\boldsymbol{F} \tag{29}$$

with $\boldsymbol{K}=\int_{\Omega}\boldsymbol{B}^{\mathrm{T}}\,\boldsymbol{c}\,\boldsymbol{B}\,\mathrm{d}\Omega$ and $\boldsymbol{F}=\int_{\Omega}\boldsymbol{H}\,\boldsymbol{b}\,\mathrm{d}\Omega+\int_{\Gamma}\boldsymbol{H}\,\bar{\boldsymbol{t}}\,\mathrm{d}\Gamma$. For the problem in analysis in this work, the force vector in (29) is given by the sum of the vector of the body forces, $f_b=\int_A \boldsymbol{H}(\boldsymbol{x})\left\{f_x \quad f_y \quad f_z \quad 0 \quad 0\right\}^T dA$, with $f_x$, $f_y$ and $f_z$ being the body forces along $x, y$ and $z$ directions, respectively, and $A$ being the area of the plate, and the vector of the external surface forces, $f_e=\int_A \boldsymbol{H}(\boldsymbol{x})\{0 \quad 0 \quad p_z \quad 0 \quad 0\}^T dA$, where $p_z$ is an external solicitation on the plate along with the axis $Oz$, producing a bending behaviour. The stiffness matrix $\boldsymbol{K}$ is established in subsection 3.3. The meshless discrete system of equations here briefly established is detailed shown in the literature [18], [19], [50].

*Journal of Computation and Artificial Intelligence in Mechanics and Biomechanics* ISSN 2184-8971
*Volume 2, Issue 2, Page 73-83, 2022*

# Bending analysis of antisymmetric angle-ply laminates using HSDTs and the radial point interpolation method – Part II: numerical examples

D. E.S. Rodrigues [1,2,3], J. Belinha [1, 2], R.M. Natal Jorge [1,4]

[1] *Institute of Science and Innovation in Mechanical and Industrial Engineering (INEGI), Porto, Portugal*
*2 School of Engineering, Polytechnic of Porto (ISEP), Department of Mechanical Engineering, Porto, Portugal.*
*3 University of Aveiro, Department of Mechanical Engineering, Campus Universitário de Santiago, Aveiro, Portugal.*
*4 Faculty of Engineering, University of Porto (FEUP), Department of Mechanical Engineering, Porto, Portugal.*

***Abstract***
*This work makes use of the Radial Point Interpolation Method (RPIM) and five different High-Order Shear Deformation Theories (HSDTs), to analyse several antisymmetric angle-ply composite laminated plates. The RPIM's formulation and the computer implementation of those HSDTs within the RPIM's code was properly explained in the first part of this work.*
*In this second part, the obtained meshless solutions are compared with the available analytical solutions. In the end, the accuracy and robustness of the meshless approach are proved, making the RPIM a strong alternative to the FEM. The meshless solutions presented in this paper enhance the state-of-the-art concerning the bending analysis of antisymmetric angle-ply laminates. Additionally, this paper provides new reference solutions for maximum displacements and stresses computed with HSDTs, which is a topic with an insufficient amount of literature solutions.*

***DOI**: 10.5281/zenodo.7492959*

*Article Info*

*Keywords*
*Meshless methods*
*Radial point interpolation method*
*Antisymmetric angle-ply laminate*
*High-Order Shear Deformation Theories*
*Plates theory*

*Article History*

| | |
|---|---|
| *Received:* | *12/10/2022* |
| *Revised:* | *16/11/2022* |
| *Accepted:* | *09/12/2022* |

## 1. Introduction

Several meshless methods have been used to study the behavior of composite laminates. Nevertheless, most of the studies found in the literature combine meshless methods with simpler plate models such as the Classical Plate Theory (CLPT) and the First-Order Shear Deformation Theory (FSDT). For instance, the Element Free Galerkin Method (EFGM) was used for the bending analysis of thin plates using the CLPT [1] and also for the linear and nonlinear analysis of isotropic plates and laminates using the FSDT [2], [3]. The Reproducing Kernel Particle Method (RKPM) was the numerical tool used in the static analysis of deformable beams and plates by B. M. Donning and W. K. Liu [4], using the FSDT. Recently, Belinha et al. analyzed the bending behavior of composite laminate plates using the FSDT [5], [6] and several meshless methods (the EFGM, the RPIM, the Natural Neighbor Radial Point Interpolation Method – NNRPIM, and the Natural Radial Element Method – NREM). Making use of a global meshless approach using radial basis functions (RBFs), Ferreira et al. considered the FSDT [7] for the bending analysis of composite laminates. The FSDT was also considered in the work by Rodrigues et al. [8]. Meshless methods have also been combined with plate models with higher order. The Third-Order Shear Deformation Theory (TSDT) of Reddy [9], for instance, was combined with the EFGM [10], the global meshless approach using RBFs by Ferreira et al. [11] [12] [13] and the NNRPIM [14]; the previously cited NNRPIM (a 'truly' meshless version of the RPIM employed in this work) was also used to analyze the bending behavior of symmetric and antisymmetric laminates using distinct High-Order Shear Deformation Theories (HSDTs) [15]–[17]; Xiang et al. [18], using a meshless local radial point collocation method based on multiquadric radial basis function (MQ-RBF), analyzed the static response of isotropic, sandwich and laminated plates considering several HSDTs (by Levinson [19], Aydogdu [20], Karama [21] and Touratier [22]); a higher order shear and normal deformable plate theory (HOSNDPT) [23] [24] [25] was combined with Meshless Local Petrov-Galerkin Method (MLPG) for the analysis of thick laminated composite and functionally graded plates, etc; Tornabene et al. [26] studied doubly-curved laminated



*Corresponding Author:*
*Jorge Belinha*
*job@isep.ipp.pt*

composite shells and panels using RBFs and HSDTs based on the Carrera Unified Formulation (CUF) [27]. Shukla et al. used eight layered symmetric and antisymmetric laminated plates to perform free vibration analysis [28] considering an HSDT following a new transverse shear stress function by Kumar et al. [29] and employing an RBF based meshless approach. The same authors also performed buckling [30] and bending [31] analyses.

The RPIM has been used in the static [5], [32] and dynamic [33]–[35] analysis of composite plates and shells, the inelastic analysis of 2D solids [36], 3D contact problems [37], crack growth modelling in elastic solids [38], non-local constitutive damage models [39], etc. However, it has not yet been used for the analysis of bending antisymmetric angle-ply laminates using HSDTs – this work proposes the extension of the RPIM to that field of application. Thus, this study presents, in novelty, RPIM's solutions for the bending of composite laminates with angle-ply layers, providing new numerical solutions for a solid mechanic's field where the literature lacks, enhancing the state-of-the-art concerning angle-ply laminated plates, HSDTs, and the RPIM itself.

In the following sections, the authors present the obtained numerical solutions.

## 2. Meshless Solutions

Several antisymmetric angle-ply laminates are investigated in this section. The considered material properties are as follows:

$$\text{Material 1: } E_1 = 40 \text{ GPa}, \; E_2 = 1 \text{ GPa}, \; \nu_{12} = 0.25, G_{12} = G_{13} = 0.6 \text{ GPa} \text{ and } G_{23} = 0.5 \text{ GPa}.$$
$$\text{Material 2: } E_1 = 25 \text{ GPa}, \; E_2 = 1 \text{ GPa}, \; \nu_{12} = 0.25, G_{12} = G_{13} = 0.5 \text{ GPa} \text{ and } G_{23} = 0.2 \text{ GPa}$$

Uniformly distributed loads (UDL) and sinusoidal distributed transverse loads (SSL) are considered in this study, being the load functions, $q(x,y)$, presented in Eq. (1) - $q_0$ is the nominal load.

$$\begin{aligned} q(x,y) &= q_0 \\ q(x,y) &= q_0 \sin\left(\frac{\pi x}{a}\right)\sin\left(\frac{\pi y}{b}\right) \end{aligned} \tag{1}$$

where $a$ and $b$ are the in-plane dimensions of the plate. All the solutions found are normalized according to the following expressions and are obtained at the coordinates $(x,y,z)$ suggested below,

$$\begin{aligned} \overline{w} &= w(0,0,z)\cdot\frac{E_2 h^3}{q_0 \cdot a^4} & \overline{\sigma}_{xx} &= \sigma_{xx}(0,0,z)\cdot\frac{h^2}{q_0 \cdot a^2} & \overline{\sigma}_{yy} &= \sigma_{yy}(0,0,z)\cdot\frac{h^2}{q_0 \cdot a^2} \\ \overline{\tau}_{xy} &= \tau_{xy}\left(-\frac{a}{2},-\frac{b}{2},z\right)\cdot\frac{h}{q_0 \cdot a} & \overline{\tau}_{yz} &= \tau_{yz}\left(0,-\frac{b}{2},z\right)\cdot\frac{h}{q_0 \cdot a} & \overline{\tau}_{xz} &= \tau_{xz}\left(\frac{a}{2},0,z\right)\cdot\frac{h}{q_0 \cdot a} \end{aligned} \tag{2}$$

the $z$-coordinates are presented in Table 1:

| | $\overline{w}$ | $\overline{\sigma}_{xx}$ | $\overline{\sigma}_{yy}$ | $\overline{\tau}_{xy}$ | $\overline{\tau}_{yz}$ | $\overline{\tau}_{xz}$ |
|---|---|---|---|---|---|---|
| $(\theta/-\theta)_n$ | 0 | h/2 (k =2 n) | h/2 (k = 2n) | - h/2 (k = 1) | 0 (k = 2) | 0 (k = 1) |

**Table 1** – Values for the z-coordinate in the places where the central transverse displacement and maximum stresses are calculated, as well as the respective index of the layer.

Regarding the formulation of the RPIM, a null polynomial basis is considered in the determination of the interpolation functions and the 'influence-domains' have a fixed number of nodes: 16.

## 2.1. Convergence Study

Before obtaining the main solutions, a suitable nodal mesh needs to be found. Thus, central transverse displacements and maximum stresses were obtained using regular nodal meshes with a progressively higher number of nodes. The nodal meshes followed a quadratic nodal distribution: (2+1)×(2+1), (4+1)×(4+1), (8+1)×(8+1), (16+1)×(16+1), (32+1)×(32+1). Due to the computer processor's limitation, the densest analysed nodal mesh has (50+1)×(50+1), corresponding to 2601 nodes.

In **Erro! A origem da referência não foi encontrada.**Fig. 1 is shown the graphs of the convergence studies performed on antisymmetric angle-ply laminates with stacking sequences $(30/-30)$ and $(45/-45)_3$, using two different thicknesses and the material properties of Material 1. Thus, through these convergence studies, different aspect ratios, HSDTs and stacking sequences are investigated to prove the robustness of the RPIM.

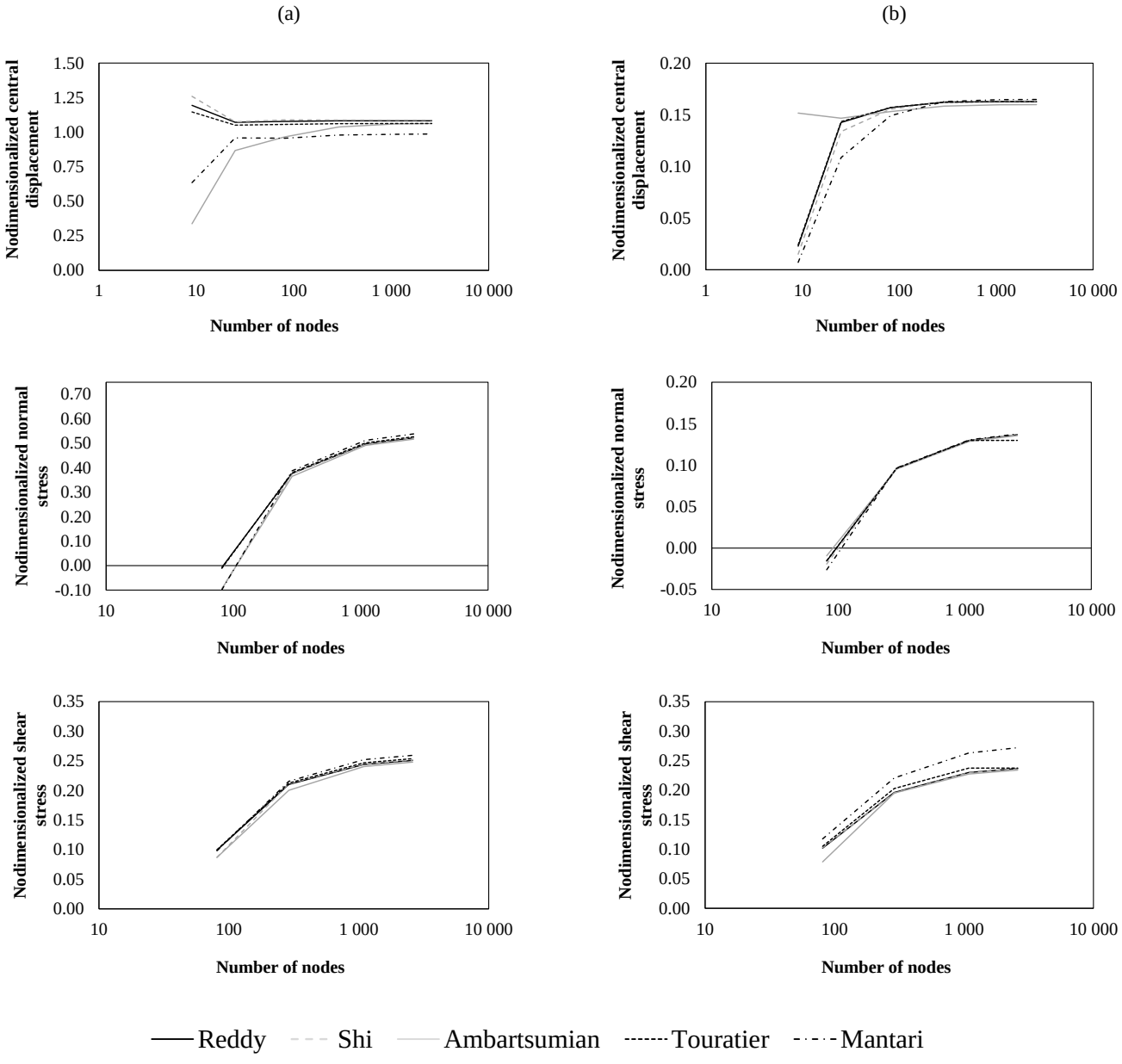


**Fig. 1** – Convergence studies of the nodimensionalized central transverse displacements, maximum normalized normal stress, $\overline{\sigma}_{xx}$, and maximum normalized shear stress, $\overline{\tau}_{xz}$, computed for: (a) an antisymmetric angle-ply square laminated plate $(30/-30)$ with a/h=4, subjected to a sinusoidal load (SSL); (b) an antisymmetric angle-ply square laminated plate $(45/-45)_3$ with a/h=100, subjected to a sinusoidal load (SSL).

By analysing **Erro! A origem da referência não foi encontrada.**Fig. 1, it can be concluded that the convergence rate of the central displacement depends on the HSDT, the thickness of the plate, and the number of layers. Nevertheless, for both laminates, faster convergences are observed. Additionally, the converged values of the central displacements are similar for all the analysed HSDTs. Regarding the maximum normal and shear stresses, the differences between the convergence curves for the different HSDTs are almost negligible. When the convergence studies of both laminates are compared, it can be seen that the convergence rate of the stresses is not as dependent on the stacking sequence and the laminate thickness as it is in the case of the convergence of the central displacements. Thus, based on these convergence studies, a regular nodal mesh with (32+1)×(32+1) nodes achieves similar results when compared with the nodal mesh composed of (50+1)×(50+1) nodes (having the last one a higher computational cost). Therefore, the first-mentioned mesh was used for further analysis in the next subsections.

### 2.2. Normalized Maximum Displacements and Stresses. Stress Distribution Across Thickness.

After the definition of the nodal mesh, the bending behaviour of antisymmetric angle-ply laminates subjected to sinusoidal and uniformly distributed loads was studied. In the first study, maximum transverse displacements were obtained using the RPIM and each HSDTs - and also the FSDT – for the laminates $(5/-5)$, $(5/-5)_3$, $(30/-30)$, $(30/-30)_3$, $(45/-45)$ and $(45/-45)_3$ using Material 1. These results are shown in Table 2 for different ratios of the length of the plate over its thickness, a/h. In the same table are also presented the exact analytical solutions for the FSDT and also for Reddy's TSDT, for comparison purposes, since there are no literature solutions for the remaining HSDTs.

The results show a solid agreement with the solutions proposed by Reddy [9], particularly for laminates with a higher number of layers (i.e. lower layer thickness) and a higher ply angle. The less satisfactory results are found for thinner laminates with stacking sequence $(5/-5)$ (this may be related to the nodal density - i.e. a higher number of nodes should decrease the error and approximate the present results to fully converged solutions). The results presented in the mentioned table for Reddy's TSDT were transformed in percentage errors regarding the respective exact solution. The absolute errors are obtained with $\varepsilon(\%) = 100 \times \left| \xi_{exact} - \xi_{present} \right| / \left| \xi_{exact} \right|$, (being $\xi$ a general variable, which can be assumed as the displacement or the stress at a given interest point) and are graphically represented in Fig. 2.

From Fig. 2, it becomes clear that the RPIM is an accurate numerical tool particularly when the laminates with six layers are analyzed where the absolute errors are always inferior to 0.7%.

Proved the accuracy of the RPIM in the determination of the central displacements, the maximum stresses were also obtained, using the laminates $(-45/45)$ and $(-45/45)_4$ with different thicknesses and under two load types. Table 3 shows the obtained RPIM results which, due to a lack of analytical solutions in the literature for this type of laminates analysed with HSDTs, could only be compared with the Navier solution [9] of the FSDT, provided by Reddy using Material 2.

The solutions presented in Table 3 show a good agreement between each other and present also a great agreement with the Navier solution (which used the FSDT, so it cannot be used as a reliable term of comparison with the present solutions using HSDTs). Mantari's theory predicts the highest values for the shear stresses, which may verify the statement made by Mantari: the errors between 3D Elasticity and 2D solutions are lowered in the majority of his calculations when compared with other existing HSDTs. Ambartsumian's theory predicts the lowest shear stresses, this is explained by the fact that this HSDT has the lowest coefficient of the third-order term in the transverse shear function – see part I of this paper. Shi and Reddy's TSDT produce similar solutions since their mathematical representations are formally similar. To prove that the traction boundary conditions are verified for these HSDTs and to verify the smooth stress distributions which are generally obtained with the RPIM, the nodimensionalized normal stress, $\bar{\sigma}_{xx}$, and shear stress, $\bar{\tau}_{xz}$, were computed as a function of the normalized thickness, *z/h* - Fig. 3. The graphs of Fig. 3 are plotted for laminates with the stacking sequences $(30/-30)$ and $(30/-30)_3$, being the aspect ratio *a/h*=10 for both cases using the elastic properties of Material 1.

From their observation, it can be concluded that the top and bottom boundary conditions are verified (condition of zero shear stresses). Additionally, as expected, the distribution of the normal stresses is discontinuous at layer interfaces (since these results are obtained from constitutive relations) and are non-symmetric. The differences between the curves are almost insignificant in the case of the normal stresses, but when the graphs concerning the transverse shear stresses are observed, it can be seen main differences between the stress distributions computed from each HSDT (with Mantari's

theory predicting the highest maximum shear stress). Regarding the two analysed laminate configurations, it could be verified that, maintaining the ply angles, it is possible to decrease the maximum normal stress by increasing the number of layers.

| | | | **θ = 5°** | | **θ = 30** | | **θ = 45°** | |
|---|---|---|---|---|---|---|---|---|
| **a/h** | **Solution** | **ESL** | **n=1** | **n=3** | **n=1** | **n=3** | **n=1** | **n=3** |
| **4** | Analytical [9] | Reddy | 1.2625 | 1.2282 | 1.0838 | 0.8851 | 1.0203 | 0.8375 |
| | | FSDT | 1.3165 | 1.2647 | 1.2155 | 0.8994 | 1.1576 | 0.8531 |
| | RPIM | Reddy | 1.2719 | 1.2256 | 1.0825 | 0.8812 | 1.0142 | 0.8336 |
| | | Shi | 1.2789 | 1.2323 | 1.0870 | 0.8849 | 1.0181 | 0.8371 |
| | | Ambartsumian | 1.2369 | 1.1920 | 1.0592 | 0.8617 | 0.9930 | 0.8149 |
| | | Touratier | 1.2580 | 1.2150 | 1.0629 | 0.8617 | 0.9945 | 0.8265 |
| | | Mantari | 1.1971 | 1.1647 | 0.9850 | 0.8352 | 0.9159 | 0.7864 |
| | | FSDT | 1.3435 | 1.2671 | 1.2245 | 0.8997 | 1.1581 | 0.8533 |
| **10** | Analytical [9] | Reddy | 0.4848 | 0.4485 | 0.5916 | 0.3007 | 0.5581 | 0.2745 |
| | | FSDT | 0.4883 | 0.4491 | 0.6099 | 0.2989 | 0.5773 | 0.2728 |
| | RPIM | Reddy | 0.5013 | 0.4496 | 0.6021 | 0.2997 | 0.5552 | 0.2729 |
| | | Shi | 0.5178 | 0.4520 | 0.6046 | 0.3010 | 0.5574 | 0.2746 |
| | | Ambartsumian | 0.4403 | 0.4387 | 0.5899 | 0.2938 | 0.5446 | 0.2683 |
| | | Touratier | 0.4979 | 0.4488 | 0.5991 | 0.2994 | 0.5523 | 0.2733 |
| | | Mantari | 0.5157 | 0.4499 | 0.5927 | 0.2995 | 0.5451 | 0.2730 |
| | | FSDT | 0.5254 | 0.4521 | 0.6248 | 0.2992 | 0.5777 | 0.2729 |
| **20** | Analytical [9] | Reddy | 0.3579 | 0.3209 | 0.5180 | 0.2127 | 0.4897 | 0.1905 |
| | | FSDT | 0.3586 | 0.3208 | 0.5224 | 0.2121 | 0.4944 | 0.1899 |
| | RPIM | Reddy | 0.3828 | 0.3224 | 0.5307 | 0.2121 | 0.4872 | 0.1898 |
| | | Shi | 0.3956 | 0.3242 | 0.5328 | 0.2130 | 0.4891 | 0.1906 |
| | | Ambartsumian | 0.3368 | 0.3149 | 0.5199 | 0.2080 | 0.4779 | 0.1863 |
| | | Touratier | 0.3819 | 0.3222 | 0.5296 | 0.2120 | 0.4862 | 0.1897 |
| | | Mantari | 0.3993 | 0.3264 | 0.5320 | 0.2141 | 0.4878 | 0.1914 |
| | | FSDT | 0.3979 | 0.3240 | 0.5385 | 0.2124 | 0.4947 | 0.1900 |
| **50** | Analytical [9] | Reddy | 0.3215 | 0.2842 | 0.4972 | 0.1878 | 0.4704 | 0.1668 |
| | | FSDT | 0.3216 | 0.2841 | 0.4979 | 0.1877 | 0.4712 | 0.1667 |
| | RPIM | Reddy | 0.3438 | 0.2858 | 0.5104 | 0.1873 | 0.4679 | 0.1662 |
| | | Shi | 0.3548 | 0.2874 | 0.5124 | 0.1881 | 0.4697 | 0.1668 |
| | | Ambartsumian | 0.3161 | 0.2791 | 0.4999 | 0.1837 | 0.4590 | 0.1631 |
| | | Touratier | 0.3478 | 0.2856 | 0.5099 | 0.1872 | 0.4675 | 0.1661 |
| | | Mantari | 0.3649 | 0.2904 | 0.5144 | 0.1896 | 0.4713 | 0.1681 |
| | | FSDT | 0.3563 | 0.2873 | 0.5141 | 0.1880 | 0.4713 | 0.1667 |
| **100** | Analytical [9] | Reddy | 0.3162 | 0.2789 | 0.4942 | 0.1842 | 0.4676 | 0.1634 |
| | | FSDT | 0.3162 | 0.2789 | 0.4944 | 0.1842 | 0.4678 | 0.1633 |
| | RPIM | Reddy | 0.3381 | 0.2805 | 0.5071 | 0.1837 | 0.4648 | 0.1627 |
| | | Shi | 0.3413 | 0.2820 | 0.5089 | 0.1845 | 0.4664 | 0.1634 |
| | | Ambartsumian | 0.3105 | 0.2739 | 0.4968 | 0.1801 | 0.4561 | 0.1597 |
| | | Touratier | 0.3374 | 0.2803 | 0.5067 | 0.1836 | 0.4645 | 0.1627 |
| | | Mantari | 0.3399 | 0.2850 | 0.5109 | 0.1860 | 0.4681 | 0.1646 |
| | | FSDT | 0.3419 | 0.2820 | 0.5101 | 0.1844 | 0.4675 | 0.1633 |

**Table 2** – Maximum normalized transverse displacements for simply supported antisymmetric angle-ply square laminates subjected to a sinusoidal load (SSL), with the stacking sequence $(\theta/-\theta)_n$ .

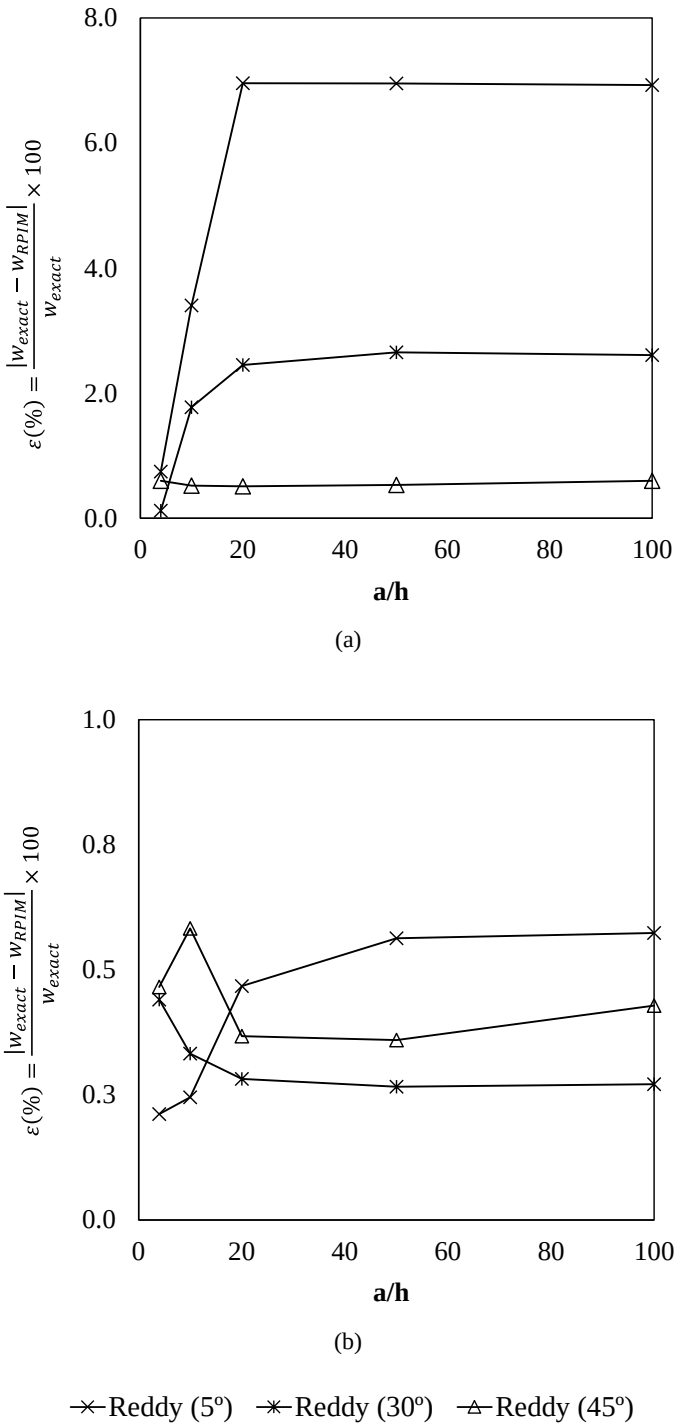


**Fig. 2** – Relative errors (%) regarding the respective exact solution for the maximum normalized transverse displacements of a simply supported laminated plate with antisymmetric angle-ply layer, subjected to a sinusoidal load (SSL). (a) $(\theta/-\theta)$ and (a) $(\theta/-\theta)_3$.

## 2.3. Maximum Central Displacement as Function of the Ply Angle

Using Material 2, maximum nondimensionalized transverse displacements were obtained for antisymmetric angle-ply laminates with different ply angles. Thus, in Fig. 4, graphs were plotted for laminates with a generic stacking sequence

$(-\theta/\theta)_n$ and a specific ratio of the length of the plate over its thickness (a/h=10). In Fig. 4, ply angles, $\theta$, are swept between $0^o$ and $90^o$, and the central displacements are computed for each angle and HSDT using the RPIM.

| | | | | **Angle-ply laminate (-45 / 45)** | | | | **Angle-ply laminate $(-45/45)_4$** | | | |
|---|---|---|---|---|---|---|---|---|---|---|---|
| **a/h** | **Source** | **ESL** | **Load** | $\overline{w} \times 10^2$ | $\overline{\sigma}_{xx}$ | $\overline{\tau}_{xy}$ | $\overline{\tau}_{xz}$ | $\overline{w}$ | $\overline{\sigma}_{xx}$ | $\overline{\tau}_{xy}$ | $\overline{\tau}_{xz}$ |
| 10 | Analytical | FSDT [9] | SSL | 0.8284 | 0.2498 | 0.2336 | 0.2143 | 0.4198 | 0.1445 | 0.1384 | 0.2487 |
| | | | UDL | 1.2792 | 0.3476 | 0.4274 | 0.4238 | 0.6366 | 0.1957 | 0.2463 | 0.4960 |
| | | Reddy [9] | SSL | 0.8250 | 0.2594 | 0.2029 | 0.2154 | - | - | - | - |
| | RPIM (Present) | Reddy | SSL | 0.7990 | 0.2412 | 0.2496 | 0.2115 | 0.4191 | 0.1490 | 0.1546 | 0.2298 |
| | | | UDL | 1.2361 | 0.3389 | 0.4759 | 0.3796 | 0.6358 | 0.2025 | 0.3017 | 0.4125 |
| | | Shi | SSL | 0.8021 | 0.2417 | 0.2506 | 0.2119 | 0.4208 | 0.1492 | 0.1549 | 0.2302 |
| | | | UDL | 1.2409 | 0.3394 | 0.4791 | 0.3804 | 0.6384 | 0.2027 | 0.3033 | 0.4133 |
| | | Ambartsumian | SSL | 0.7837 | 0.2390 | 0.2346 | 0.2093 | 0.4112 | 0.1480 | 0.1456 | 0.2275 |
| | | | UDL | 1.2111 | 0.3358 | 0.4408 | 0.3700 | 0.6231 | 0.2013 | 0.2775 | 0.4084 |
| | | Touratier | SSL | 0.7949 | 0.2417 | 0.2500 | 0.2155 | 0.4184 | 0.1500 | 0.1556 | 0.2368 |
| | | | UDL | 1.2301 | 0.3394 | 0.4771 | 0.3868 | 0.6350 | 0.2036 | 0.3042 | 0.4248 |
| | | Mantari | SSL | 0.7851 | 0.2442 | 0.2504 | 0.2276 | 0.4170 | 0.1538 | 0.1557 | 0.2617 |
| | | | UDL | 1.2162 | 0.3427 | 0.4767 | 0.4077 | 0.6333 | 0.2081 | 0.3031 | 0.4679 |
| 20 | Analytical | FSDT [9] | SSL | 0.6891 | 0.2498 | 0.2336 | 0.2143 | 0.2896 | 0.1445 | 0.1384 | 0.2487 |
| | | | UDL | 1.0907 | 0.3496 | 0.4357 | 0.4305 | 0.4483 | 0.1988 | 0.2550 | 0.4884 |
| | RPIM (Present) | Reddy | SSL | 0.6888 | 0.2309 | 0.2391 | 0.2123 | 0.2890 | 0.1366 | 0.1418 | 0.2312 |
| | | | UDL | 1.0767 | 0.3297 | 0.4461 | 0.3793 | 0.4473 | 0.1918 | 0.2673 | 0.4100 |
| | | Shi | SSL | 0.6915 | 0.2314 | 0.2397 | 0.2128 | 0.2902 | 0.1369 | 0.1418 | 0.2316 |
| | | | UDL | 1.0809 | 0.3303 | 0.4476 | 0.3801 | 0.4491 | 0.1921 | 0.2677 | 0.4107 |
| | | Ambartsumian | SSL | 0.6757 | 0.2287 | 0.2287 | 0.2101 | 0.2837 | 0.1356 | 0.1372 | 0.2291 |
| | | | UDL | 1.0554 | 0.3265 | 0.4240 | 0.3753 | 0.4388 | 0.1904 | 0.2566 | 0.4062 |
| | | Touratier | SSL | 0.6875 | 0.2310 | 0.2393 | 0.2166 | 0.2888 | 0.1369 | 0.1421 | 0.2385 |
| | | | UDL | 1.0747 | 0.3298 | 0.4466 | 0.3870 | 0.4470 | 0.1921 | 0.2681 | 0.4230 |
| | | Mantari | SSL | 0.6901 | 0.2327 | 0.2397 | 0.2296 | 0.2911 | 0.1385 | 0.1417 | 0.2655 |
| | | | UDL | 1.0788 | 0.3321 | 0.4470 | 0.4102 | 0.4506 | 0.1941 | 0.2675 | 0.4702 |
| 100 | Analytical | FSDT [9] | SSL | 0.6564 | 0.2498 | 0.2336 | 0.2143 | 0.2479 | 0.1445 | 0.1384 | 0.2487 |
| | | | UDL | 1.0305 | 0.3504 | 0.4417 | 0.4188 | 0.3883 | 0.2005 | 0.2630 | 0.4881 |
| | | CLPT [9] | SSL | 0.6547 | 0.2498 | 0.2336 | 0.2143 | 0.2462 | 0.1445 | 0.1384 | 0.2487 |
| | | | UDL | 1.0280 | 0.3504 | 0.4421 | 0.4188 | 0.3858 | 0.2006 | 0.2637 | 0.4338 |
| | RPIM (Present) | Reddy | SSL | 0.6527 | 0.2275 | 0.2362 | 0.2089 | 0.2469 | 0.1326 | 0.1381 | 0.2305 |
| | | | UDL | 1.0244 | 0.3267 | 0.4369 | 0.3721 | 0.3867 | 0.1890 | 0.2581 | 0.4057 |
| | | Shi | SSL | 0.6550 | 0.2279 | 0.2365 | 0.2078 | 0.2479 | 0.1328 | 0.1381 | 0.2302 |
| | | | UDL | 1.0280 | 0.3273 | 0.4375 | 0.3700 | 0.3882 | 0.1893 | 0.2580 | 0.4050 |
| | | Ambartsumian | SSL | 0.6404 | 0.2253 | 0.2289 | 0.2083 | 0.2424 | 0.1315 | 0.1356 | 0.2284 |
| | | | UDL | 1.0046 | 0.3236 | 0.4218 | 0.3715 | 0.3795 | 0.1875 | 0.2528 | 0.4025 |
| | | Touratier | SSL | 0.6522 | 0.2274 | 0.2362 | 0.2134 | 0.2468 | 0.1326 | 0.1381 | 0.2380 |
| | | | UDL | 1.0237 | 0.3267 | 0.4369 | 0.3801 | 0.3865 | 0.1890 | 0.2582 | 0.4190 |
| | | Mantari | SSL | 0.6577 | 0.2287 | 0.2352 | 0.2211 | 0.2498 | 0.1334 | 0.1372 | 0.2626 |
| | | | UDL | 1.0318 | 0.3283 | 0.4345 | 0.3944 | 0.3910 | 0.1901 | 0.2562 | 0.4620 |

**Table 3** – Maximum normalized transverse displacements and stresses in two simply supported antisymmetric angle-ply $(-45/45)_n$ square laminates subjected to sinusoidal (SSL) and uniformly distributed loads (UDL). Solutions found with the RPIM.

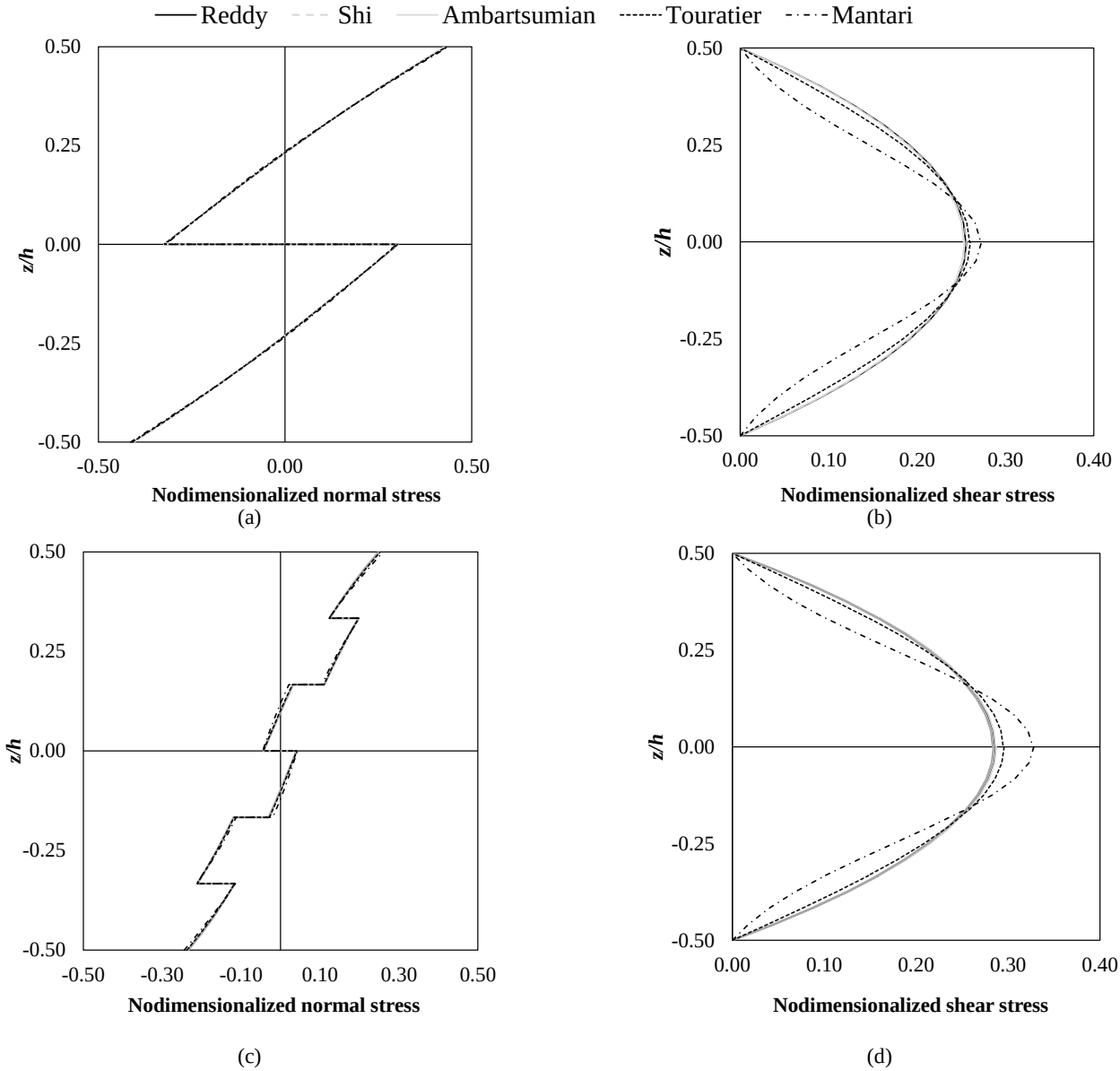


**Fig. 3** – Nodimensionalized normal, $\bar{\sigma}_{xx}$, and shear, $\bar{\tau}_{xz}$, stresses through the thickness of two simply supported antisymmetric square laminates with angle-ply layers subjected to sinusoidal loads (SSL), with aspect ratio *a/h*=10. (a) and (b): $(30/-30)$; (c) and (d): $(30/-30)_3$.

From Fig. 4(a), it can be concluded that for the laminates with two layers the maximum deflection occurs for ply angles of $17^{\circ}$ and $73^{\circ}$, while the minimum deflection occurs for ply angles of $0^{\circ}$ or $90^{\circ}$ (these angles make the laminate a simple orthotropic plate). For this last configuration (equivalent to an orthotropic plate) a laminate with eight layers (Fig. 4(b)) has its maximum value of deflection, while the minimum deflection is shown for $\theta = 45^{\circ}$. These observations are valid for Material 2. It can also be stated that the minimum value of the deflection for laminates with two layers is very close to the maximum value for laminates with eight layers. Concerning the HSDTs considered, the presented results do not show significant differences since it is not the purpose of the HSDT to predict with more accuracy the central transverse displacements.

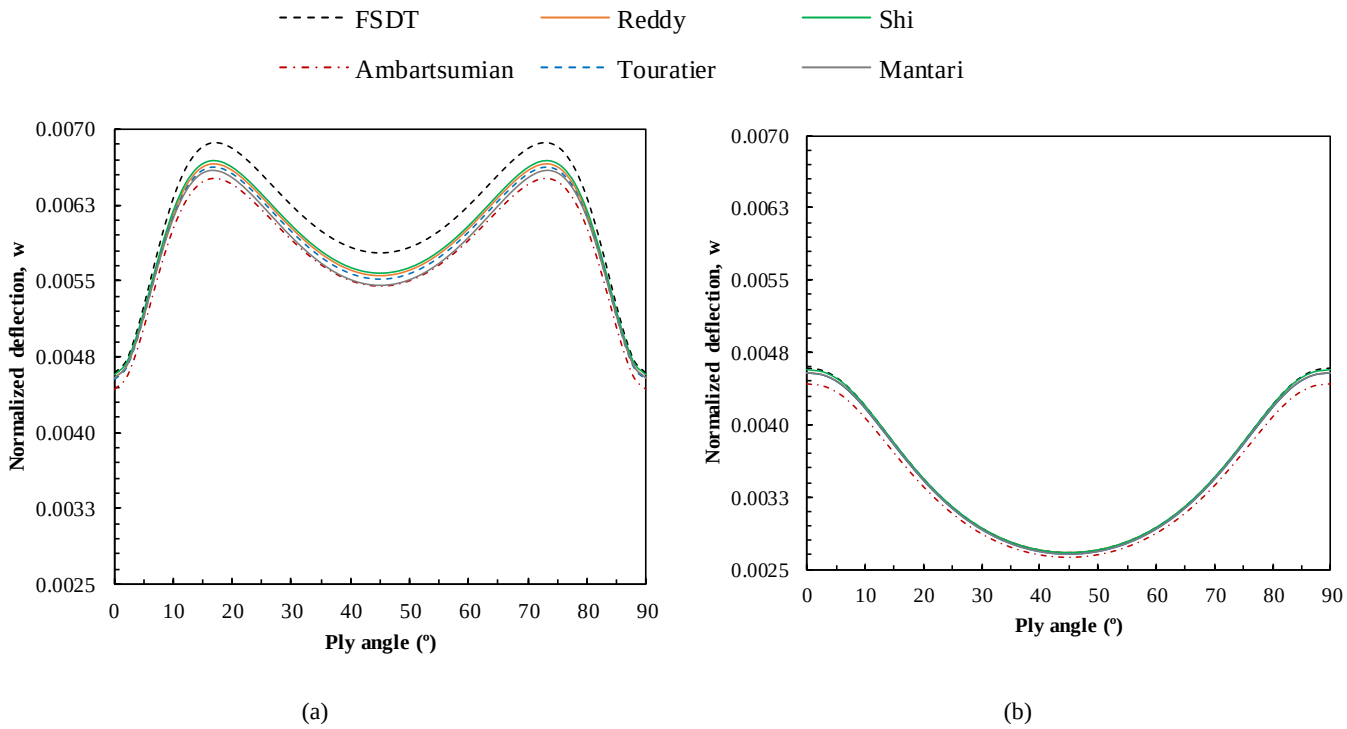


**Fig. 4** – Maximum normalized transverse displacements for two simply supported laminated plates with antisymmetric angle-ply layers, (a) $(-\theta/\theta)$ and (b) $(-\theta/\theta)_4$, subjected to a sinusoidal load (SSL). Displacements as a function of the ply angle computed with the RPIM, a/h=10.

## 3. Conclusions

In the problems studied, the HSDTs analysed proved to yield similar solutions in terms of central displacements and maximum normal stresses. Regarding the shear stresses – where the purpose of using HSDTs is found – Mantari's theory predicts higher values for these components of the stress tensor, which might better approximate the 3D Elasticity solutions than the remaining HSDTs. Reddy and Shi plate models allowed to obtain similar solutions, while Ambartsumian's theory shown a distinct behaviour, predicting the lower values for the shear stresses than the other two Third-Oder Shear Deformation Theories (TSDTs). The present approach ensures the condition of zero shear stresses at the top and bottom boundaries of the plate.

For Reddy's TSDT (the only HSDT which has documented solutions in the literature), very low errors were achieved with the performed bending analysis, in particular for laminates with plies with $45^o$ orientations of their fibres and with six layers.

In the authors' opinion, this work successfully extends the field of application of the RPIM – showing its robustness and accuracy – and enhances the state-of-the-art concerning angle-ply laminates for which the literature lacks in providing solutions regarding the bending behaviour of these structures.

## Acknowledgements and Funding

The authors truly acknowledge the funding provided by Ministério da Ciência, Tecnologia e Ensino Superior – Fundação para a Ciência e a Tecnologia (Portugal), under grant SFRH/BD/121019/2016, and by project funding MIT-EXPL/ISF/0084/2017. Additionally, the authors gratefully acknowledge the funding of Project NORTE-01-0145-FEDER-000022 – SciTech – Science and Technology for Competitive and Sustainable Industries, co-financed by Programa Operacional Regional do Norte (NORTE2020), through Fundo Europeu de Desenvolvimento Regional (FEDER).

## References

[1] P. Krysl and T. Belytschko, "Analysis of Thin Plates by the Element-Free Galerkin Method," *Comput. Mech.*, vol. 17, no. 1–2, pp. 26–35, 1995.

[2] J. Belinha and L. Dinis, "Analysis of plates and laminates using the element-free Galerkin method," *Comput. Struct.*, vol. 84, no. 22, pp. 1547–1559, 2006.

[3] J. Belinha, "Nonlinear analysis of plates and laminates using the element free Galerkin method," *Compos. Struct.*, vol. 78, no. 3, pp. 337–350, 2007, doi: 10.1016/j.compstruct.2005.10.007.

[4] B. M. Donning and W. K. Liu, "Meshless methods for shear-deformable beams and plates," *Comput. Methods Appl. Mech.*

*Eng.*, vol. 152, no. 1, pp. 47–71, 1998.

[5] J. Belinha, A. L. Araújo, A. J. M. Ferreira, L. M. J. S. Dinis, and R. M. N. Jorge, "The analysis of laminated plates using distinct advanced discretization meshless techniques," *Compos. Struct.*, vol. 143, pp. 165–179, 2016, doi: 10.1016/j.compstruct.2016.02.021.

[6] L. M. J. S. Dinis, R. M. Natal Jorge, and J. Belinha, "Analysis of plates and laminates using the natural neighbour radial point interpolation method," *Eng. Anal. Bound. Elem.*, vol. 32, no. 3, pp. 267–279, 2008, doi: 10.1016/j.enganabound.2007.08.006.

[7] A. J. M. Ferreira, "A formulation of the multiquadric radial basis function method for the analysis of laminated composite plates," *Compos. Struct.*, vol. 59, no. 3, pp. 385–392, 2003.

[8] D. Rodrigues, J. Belinha, A. Araújo, L. Dinis, R. N. Jorge, and A. Ferreira, "The computational analysis of composite laminates: Meshless formulation," in *Material Modelling: Applications, Challenges and Research*, 2017, pp. 167–214.

[9] J.N. Reddy, "Mechanics of laminated composite plates and shells: theory and analysis." CRC Press LLC, Boca Raton, Florida, 2004, doi: 10.1007/978-1-4471-0095-9.

[10] K. Y. Dai, G. R. Liu, K. M. Lim, and X. L. Chen, "A mesh-free method for static and free vibration analysis of shear deformable laminated composite plates," *J. Sound Vib.*, vol. 269, no. 3–5, pp. 633–652, 2004, doi: 10.1016/S0022-460X(03)00089-0.

[11] A. J. M. Ferreira, "Static analysis of functionally graded plates using third-order shear deformation theory and a meshless method," *Compos. Struct.*, vol. 69, no. 4, pp. 449–457, 2005, doi: 10.1016/j.compstruct.2004.08.003.

[12] A. J. M. Ferreira, C. M. C. Roque, R. M. N. Jorge, G. E. Fasshauer, and R. C. Batra, "Analysis of Functionally Graded Plates by a Robust Meshless Method," *Mech. Adv. Mater. Struct.*, vol. 14, no. 8, pp. 577–587, 2007, doi: 10.1080/15376490701672732.

[13] A. J. M. Ferreira, C. M. C. Roque, and P. a. L. S. Martins, "Analysis of composite plates using higher-order shear deformation theory and a finite point formulation based on the multiquadric radial basis function method," *Compos. Part B Eng.*, vol. 34, no. 7, pp. 627–636, 2003, doi: 10.1016/S1359-8368(03)00083-0.

[14] L. M. J. S. Dinis, R. M. N. Jorge, and J. Belinha, "Static and dynamic analysis of laminated plates based on an unconstrained third order theory and using a radial point interpolator meshless method," *Comput. Struct.*, vol. 89, no. 19–20, pp. 1771–1784, 2011, doi: 10.1016/j.compstruc.2010.10.015.

[15] D. Rodrigues, J. Belinha, R. N. Jorge, and L. Dinis, "Development of a Constitutive Model to Predict the Elasto-Plastic Behaviour of 3D-Printed Thermoplastics: A Meshless Formulation," pp. 311–329, 2020, doi: 10.1007/978-3-030-44522-5_10.

[16] D. E. S. Rodrigues, J. Belinha, L. M. J. S. Dinis, and R. M. Natal Jorge, "The numerical analysis of symmetric cross-ply laminates using the natural neighbour radial point interpolation method and high-order shear deformation theories," *Eng. Struct.*, vol. 225, p. 111247, Dec. 2020, doi: 10.1016/j.engstruct.2020.111247.

[17] D. E. S. Rodrigues, J. Belinha, L. M. J. S. Dinis, and R. M. Natal Jorge, "A meshless study of antisymmetric angle-ply laminates using high-order shear deformation theories," *Compos. Struct.*, vol. 255, p. 112795, 2021, doi: https://doi.org/10.1016/j.compstruct.2020.112795.

[18] S. Xiang, G. Li, W. Zhang, and M. Yang, "A meshless local radial point collocation method for free vibration analysis of laminated composite plates," *Compos. Struct.*, vol. 93, no. 2, pp. 280–286, 2011, doi: 10.1016/j.compstruct.2010.09.018.

[19] M. Levinson, "An accurate simple theory of the statics and dynamics of elastic plates," *Mech. Res. Commun*, no. 7, pp. 343–350, 1980.

[20] M. Aydogdu, "A new shear deformation theory for laminated composite plates," *Compos. Struct.*, vol. 89, no. 1, pp. 94–101, 2009, doi: 10.1016/j.compstruct.2008.07.008.

[21] M. Karama, K. S. Afaq, and S. Mistou, "A new theory for laminated composite plates," *Proc. Inst. Mech. Eng. Part L J. Mater. Des. Appl.*, vol. 223, no. 2, pp. 53–62, 2009, doi: 10.1243/14644207JMDA189.

[22] M. Touratier, "An efficient standard plate theory," *Int. J. Eng. Sci.*, vol. 29, no. 8, pp. 901–916, 1991.

[23] C. Wu and K. Chiu, "RMVT-based meshless collocation and element-free Galerkin methods for the quasi-3D free vibration analysis of multilayered composite and FGM plates," *Compos. Struct.*, vol. 93, no. 5, pp. 1433–1448, 2011, doi: 10.1016/j.compstruct.2010.11.015.

[24] D. F. Gilhooley and M. A. Mccarthy, "Analysis of thick functionally graded plates by using higher-order shear and normal deformable plate theory and MLPG method with radial basis functions," *Compos. Struct.*, vol. 80, no. 4, pp. 539–552, 2007, doi: 10.1016/j.compstruct.2006.07.007.

[25] J. R. Xiao, D. F. Gilhooley, and M. A. Mccarthy, "Analysis of thick composite laminates using a higher-order shear and normal deformable plate theory ( HOSNDPT ) and a meshless method," *Compos. Part B Eng.*, vol. 39, no. 2, pp. 414–427, 2008, doi: 10.1016/j.compositesb.2006.12.009.

[26] F. Tornabene, N. Fantuzzi, E. Viola, and A. J. M. Ferreira, "Radial basis function method applied to doubly-curved laminated composite shells and panels with a General Higher-order Equivalent Single Layer formulation," *Compos. Part B Eng.*, vol. 55, pp. 642–659, 2013, doi: https://doi.org/10.1016/j.compositesb.2013.07.026.

[27] F. Tornabene, E. Viola, and N. Fantuzzi, "General higher-order equivalent single layer theory for free vibrations of doubly-

curved laminated composite shells and panels," *Compos. Struct.*, vol. 104, pp. 94–117, 2013, doi: https://doi.org/10.1016/j.compstruct.2013.04.009.

[28] V. Shukla, P. C. Vishwakarma, J. Singh, and J. SIngh, "Vibration Analysis of angle-ply Laminated Plates with RBF based Meshless Approach," *Mater. Today Proc.*, vol. 18, pp. 4605–4612, 2019, doi: https://doi.org/10.1016/j.matpr.2019.07.444.

[29] R. Kumar, A. Lal, B. N. Singh, and J. Singh, "New transverse shear deformation theory for bending analysis of FGM plate under patch load," *Compos. Struct.*, vol. 208, pp. 91–100, 2019, doi: https://doi.org/10.1016/j.compstruct.2018.10.014.

[30] V. Shukla, P. C. Vishwakarma, and J. Singh, "Buckling Analysis of Symmetric and Antisymmetric Laminated Plates with Meshfree Approach," *Mater. Today Proc.*, vol. 18, pp. 4143–4150, 2019, doi: https://doi.org/10.1016/j.matpr.2019.07.358.

[31] V. Shukla and J. Singh, "Modeling and analysis of cross-ply and angle-ply laminated plates under patch loads using RBF based meshfree method and new HSDT," *Comput. Math. with Appl.*, vol. 79, no. 8, pp. 2240–2257, 2020, doi: https://doi.org/10.1016/j.camwa.2019.10.026.

[32] J. Belinha, L. M. J. S. Dinis, and R. M. Natal Jorge, "Analysis of thick plates by the natural radial element method," *Int. J. Mech. Sci.*, vol. 76, pp. 33–48, 2013, doi: http://dx.doi.org/10.1016/j.ijmecsci.2013.08.011.

[33] H.-H. Phan-Dao, "A Meshfree Radial Point Interpolation Method for Free Vibration of Laminated Composite Plates Analysis Based on Layerwise Theory," *Procedia Eng.*, vol. 142, pp. 349–356, 2016, doi: 10.1016/j.proeng.2016.02.061.

[34] R. Pilafkan, P. D. Folkow, M. Darvizeh, and A. Darvizeh, "Three dimensional frequency analysis of bidirectional functionally graded thick cylindrical shells using a radial point interpolation method (RPIM)," *Eur. J. Mech. - A/Solids*, vol. 39, pp. 26–34, May 2013, doi: http://dx.doi.org/10.1016/j.euromechsol.2012.09.014.

[35] H.-H. Phan-Dao, C. H. Thai, J. Lee, and H. Nguyen-Xuan, "Analysis of laminated composite and sandwich plate structures using generalized layerwise HSDT and improved meshfree radial point interpolation method," *Aerosp. Sci. Technol.*, vol. 58, pp. 641–660, Nov. 2016, doi: http://dx.doi.org/10.1016/j.ast.2016.09.017.

[36] K. Y. Dai, G. R. Liu, X. Han, and Y. Li, "Inelastic analysis of 2D solids using a weak-form RPIM based on deformation theory," *Comput. Methods Appl. Mech. Eng.*, vol. 195, no. 33–36, pp. 4179–4193, Jul. 2006, doi: http://dx.doi.org/10.1016/j.cma.2005.07.021.

[37] X. Qian, H. Yuan, M. Zhou, and B. Zhang, "A general 3D contact smoothing method based on radial point interpolation," *J. Comput. Appl. Math.*, vol. 257, pp. 1–13, Feb. 2014, doi: http://dx.doi.org/10.1016/j.cam.2013.08.014.

[38] N. T. Nguyen, T. Q. Bui, C. Zhang, and T. T. Truong, "Crack growth modeling in elastic solids by the extended meshfree Galerkin radial point interpolation method," *Eng. Anal. Bound. Elem.*, vol. 44, pp. 87–97, Jul. 2014, doi: http://dx.doi.org/10.1016/j.enganabound.2014.04.021.

[39] B. V Farahani, J. Belinha, F. M. Andrade Pires, A. J. M. Ferreira, and P. M. G. P. Moreira, "Extending a radial point interpolation meshless method to non-local constitutive damage models," *Theor. Appl. Fract. Mech.*, vol. 85, Part A, pp. 84–98, Oct. 2016, doi: http://dx.doi.org/10.1016/j.tafmec.2016.08.008.

[40] J. Belinha, *Meshless Methods in Biomechanics: Bone Tissue Remodelling Analysis*. Porto: Springer International Publishing, 2014.

*Journal of Computation and Artificial Intelligence in Mechanics and Biomechanics*
*Volume 2, Issue 2, Page 84-96, 2022*
ISSN 2184-8971

# Combining artificial neural networks with finite element methods to predict the structural response of the proximal femur

A.I. Pais[1], J.L. Alves[1,2] and J. Belinha[1,3]

[1] *INEGI - Institute of Science and Innovation in Mechanical and Industrial Engineering, Porto, Portugal, ana.i.pais@gmail.com*
[2] *Department of Mechanical Engineering, Faculty of Engineering, University of Porto (FEUP), Porto, Portugal, falves@fe.up.pt.pt*
[3] *Department of Mechanical Engineering, School of Engineering, Polytechnic of Porto (ISEP), Porto, Portugal, job@isep.ipp.pt*

***Abstract***
The finite element method (FEM) is a highly popular discretization numerical technique in computational mechanics. However, nowadays, numerical applications are becoming increasingly complex. Thus, traditional solving techniques generally demand a larger computational capacity and show higher computational costs. Machine learning techniques can be combined with the FEM to reduce the computational cost associated with the numerical analysis, being applied as surrogate solvers or as a predictive tool. This work presents a brief introduction to feed forward neural networks, a machine learning techinque, using MATLAB® with a first benchmark example of a classification problem, the "two moons" problem, with the objective of introducing the most important concepts. This first example allowed to understand the basic machine artificial learning with neural networks (NN) MATLAB® tools. Then, a second problem was analysed with the objective of showing the potential of combining FEM with artificial NN for a biomechanical application. It was observed that the artificial NN allow to predict displacements and stresses with a high level of accuracy and, simultaneously, save a significant computational time. Surprisingly, feature analysis through connection weights approach on the input variables showed that the neural network was capable of detecting the physical importance of the variables for each problem. The most significant disadvantage of artificial NN is the necessity of acquiring large amounts of data and prepare such data for training and testing, which is time consuming.

DOI: 10.5281/zenodo.7492971

*Article Info*

*Keywords:*
*Artificial neural networks*
*Machine learning*
*Finite element method*
*Biomechanics*

*Article History*

*Received: 14/10/2022*
*Revised: 12/11/2022*
*Accepted: 11/12/2022*

## 1 Introduction

The finite element method (FEM) is a powerful numerical technique, which has allowed the acceleration of mechanical design and research since its creation. However, with the growing complexity of the mechanical systems under analysis, systems with often millions of unknowns must be solved which requires a great deal of computational power and computing time.
Artificial intelligence (AI), a branch of computer science that develops machines and software with human-like intelligence, is proving to be an efficient alternative approach to classical modelling techniques [1, 2]. The AI, using artificial neural networks (NN), the core technique of deep learning (DL), has already been tested and applied in relevant computational mechanics fields [1, 3]. Artificial NN can be classified by their architectural structure as “feed forward neural networks” or “mutually connected neural networks” [1]. ML uses training data to learn and develop models, which later can deliver trends and predictions [3]. More, since artificial NN are capable of nonlinear mapping, NN are suitable to provide a solution for multi-variable problems in a fraction of time, when compared with conventional computational methodologies [1].



*Corresponding Author:*
*Jorge Belinha*
*job@isep.ipp.pt*

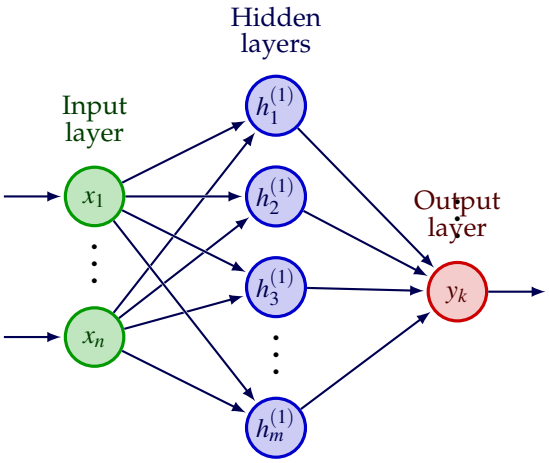


Figure 1: Artificial Neural Network architecture

Recently, there has been growing interest in the application of artificial neural networks in the field of computational mechanics [1], for example in computational homogenization of random heterogeneous materials [4], in the constitutive modelling of composites [5], in the prediction of the stress fields of solid mechanics benchmarks [6], in non-linear structural analysis [7], and in the field of biomechanics for example to predict body posture, [8, 9, 10], modelling the properties of scaffolds [11] and predicting the mechanical response and load in long bones [12, 13].
This work uses the in-house MATLAB® function *feedforwardnet*. The *feedforwardnet* and other functions mentioned in this manuscript are included in the *Deep Learning Toolbox* of MATLAB®. The first example shown in this work introduces the most important concepts and functions. The second analysed problem shows an application of artificial neural networks in the field of computational biomechanics.

## 1.1 Artificial neural networks

Figure 1 shows a scheme of a simple neural network. Any hidden or output node consists of a non-linear transformation $f$ of the values of the nodes in the previous layer. This transformation is the weighted sum of the inputs passed through a non linear activation function, and is shown in equation (1)

$$z = f\left(b + \mathbf{x}^T \cdot \mathbf{w}\right) = f\left(b + \sum_{i=1}^{m} x_i \cdot w_i\right) \tag{1}$$

where $b$ is the bias, $x_i$ is the value from the node $i$ in the previous layer and $w_i$ is the weight corresponding to that node. It is the training process of the network that allows to obtain the values for the weights and bias.
Some examples of activation functions include the sigmoid function:

$$f(\Sigma) = \frac{1}{1+e^{-\Sigma}} \tag{2}$$

and the hyperbolic tangent:

$$f(\Sigma) = \frac{e^{+\Sigma} - e^{-\Sigma}}{e^{+\Sigma} + e^{-\Sigma}} \tag{3}$$

where $\Sigma$ is, according to equation 1, the weighted sum of the nodes from the previous layer [14]. The final network is therefore able to perform some non-linear transformation and create decision boundaries capable of accurately classifying complex sets of data. In order to determine the accuracy of the neural network predictions, the mean squared error (MSE) calculates the difference between the target vector and the output vector according to equation 4,

$$MSE = \frac{1}{m}\sum_{i=1}^{m}(t_i - y_i)^2 \tag{4}$$

where $t_i$ is the element of the target vector and $y_i$ is the prediction made by the neural network for the same inputs that

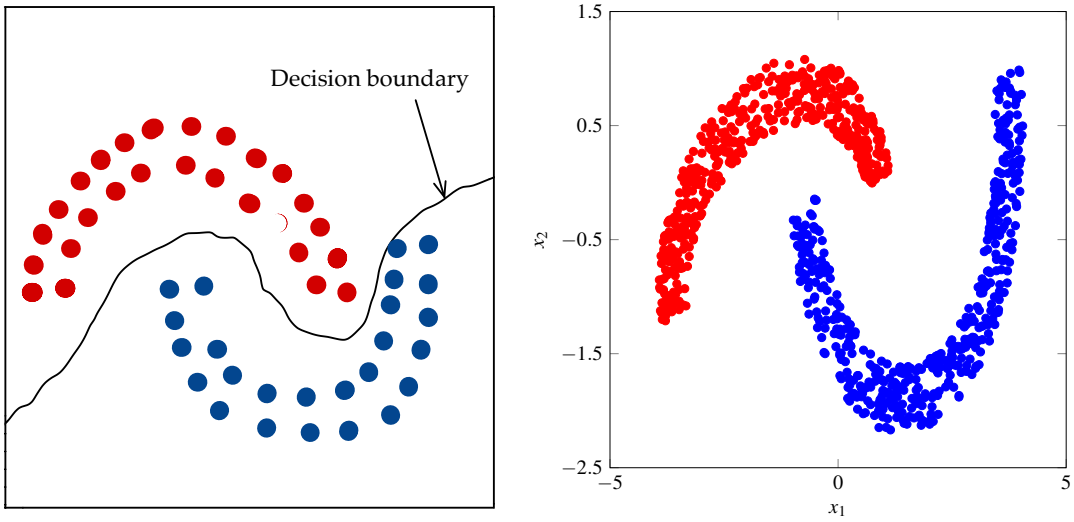


Figure 2: Schematic representation of the classification problem with the decision boundary (a) and dataset used for the training of the neural network (b)

originate the target $t_i$. The differences are squared in order to make sure that negative differences are not subtracted form positive ones [14]. Different accuracy metrics can be used, such as the mean absolute error (MAE) and mean absolute percentage error (MAPE). In a neural network training there are two different propagation moments, forward propagation where data goes from the input layer to the output layer (thus giving a prediction or classification), and backward propagation, which allows to train the network. In backward propagation data does the reverse transformation in order to determine the error and adjust the weights and bias by minimizing the cost function, which can be the MSE or any other function [14]. Each passing of data forwards and backwards through the network is called an *epoch*, thus, an *epoch* consists of using the training data only once. An *epoch* can consist on one or more iterations depending on whether the *batch size* is the same as the size of the training data. There are several algorithms to adjust the weights, which must be chosen according to the type of problem being analysed, whether the artificial neural network aims at solving a regression problem or a classification problem. The main difference between the two tasks is that a classification problem predicts a label and a regression problem predicts a quantity.

# 2 Methodology

## 2.1 Two-moons

The first example is a simple "two moons" classification example. In this example it is not possible to use a linear regression model to accurately classify the points, as the boundary between the two moon is not linear, as it can be observed in Figure 2(a). Figure 2(b) shows the training data for the "two moons" example. The input data consists on the coordinates of the point: $x_1$ and $x_2$, and the colour of each moon is the output label of the classification problem, which is going to be represented as $-1$ for blue and 1 for red.
The full code is shown next and it is going to be explained line by line afterwards.

```
1 clc
2 clear all
3 load('2Moons_sets.mat')
4 inputs = x';
5 targets = y';
6 untrained_net = feedforwardnet([4,3]);
7 view(untrained_net)
8 [trained_net,tr] = train(untrained_net,inputs,targets);
```

The previous code builds in line 6 a neural network with an input layer, two hidden layers, each with 4 and 3 nodes, respectively, and the output layer. The number of nodes in the input and output layer is inferred from the dimension of the

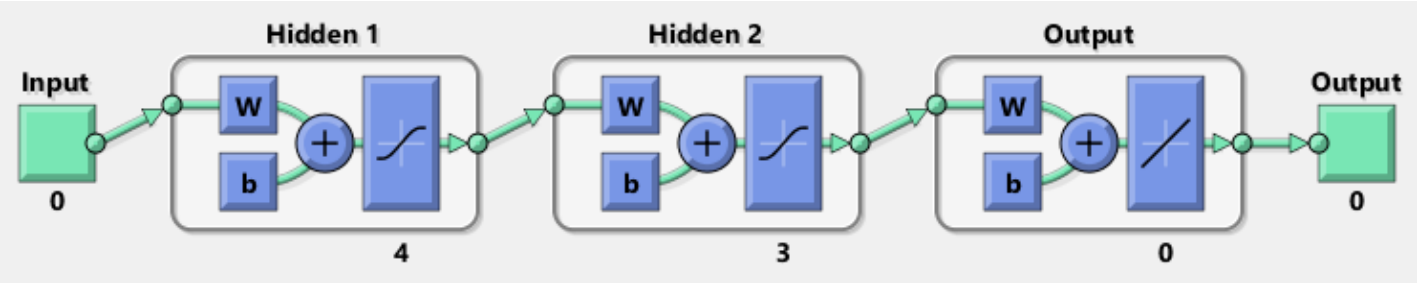


(a)

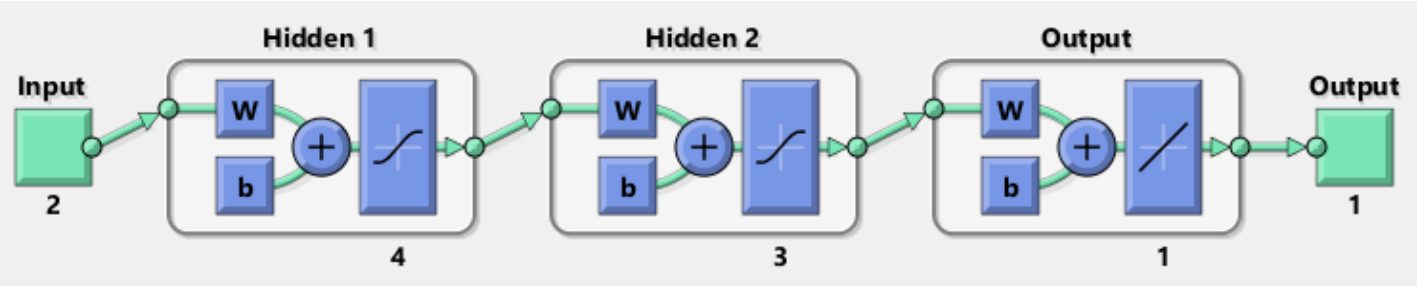


(b)

Figure 3: Result of the *view* function (a) untrained (b) trained.

arrays used and inputs and targets in line 8 when the network is trained. Because the "two-moons" dataset is not linearly separable, two hidden layers are used. If more hidden layers were used, overfitting problems are likely to occur. In Figure 3(a) it is possible to observe the output from the view net function, where it can be seen that at that stage it is still not possible to know how many nodes are at the input and output, as it indicates zero nodes. Moreover, it is possible to visualise that, by default, the transfer function in the hidden layers is a symmetric sigmoid transfer function, or *tanh* function and in the output layer we have a *'purelin'* function. This means that after the last hidden layer a linear transformation is performed, and that the input to that layer equals the output. Table 1 shows a list of available activation functions. In line 8, the *train* function will display the network with the correct number of nodes as can be seen in Figure 3(b).

Table 1: List of possible activation functions

| Name of the function | Description |
|---|---|
| *'compet'* | Competitive transfer function |
| *'elliotsig'* | Elliot sigmoid transfer function |
| *'hardlim'* | Positive hard limit transfer function |
| *'hardlims'* | Symmetric hard limit transfer function |
| *'logsig'* | Logarithmic sigmoid transfer function |
| *'netinv'* | Inverse transfer function |
| *'poslin'* | Positive linear transfer function |
| *'purelin'* | Linear transfer function |
| *'radbas'* | Radial basis transfer function |
| *'radbasn'* | Radial basis normalized transfer function |
| *'satlin'* | Positive saturating linear transfer function |
| *'satlins'* | Symmetric saturating linear transfer function |
| *'softmax'* | Soft max transfer function |
| *'tansig'* | Symmetric sigmoid transfer function (by default) |
| *'tribas'* | Triangular basis transfer function |

The *network* function is another MATLAB® function, which creates custom neural networks. The following code generates, using the network function, a neural network *net2* with the same architecture as *net1*.

```
net1 = feedforwardnet([4,3]);
view(net1)
net2 = network(1,3,[1;1;1],[1;0;0],[0 0 0;1 0 0;0 1 0],[0 0 1]);
net2.layers{1}.size = 4;
net2.layers{2}.size = 3;
net2.layers{1:2}.transferFcn = 'tansig';
view(net2);
```

The output of both the *feedforwardnet* or *network* function is an object of type *net*. Nevertheless, if the objective is to create a fully connected feed forward network, using the *feedforwardnet* allows to use less lines of code.
A second input in the *feedforwardnet* function, which was omitted in the example, is the training function. If omitted, this parameter assumes the *'trainlm'* function, which is the Levenberg-Marquardt training function. Another common training function is the "gradient descent". If one wishes for the network to be trained this way, it must be indicated in the second input of the function as *'traingd'*. A list of available training functions is shown in Table 2. The most appropriate training function will depend on the characteristics of the problem at study.

Table 2: List of available training functions in the *feedforwardnet* function

| Input in the function | Training function name |
|---|---|
| *'trainlm'* | Levenberg-Marquardt (used by default) |
| *'trainbr'* | Bayesian Regularization |
| *'trainbfg'* | BFGS Quasi-Newton |
| *'trainrp'* | Resilient Backpropagation |
| *'trainscg'* | Scaled Conjugate Gradient |
| *'traincgb'* | Conjugate Gradient with Powell/Beale Restarts |
| *'traincgf'* | Fletcher-Powell Conjugate Gradient |
| *'traincgp'* | Polak-Ribiére Conjugate Gradient |
| *'trainoss'* | One Step Secant |
| *'traingdx'* | Variable Learning Rate Gradient Descent |
| *'traingdm'* | Gradient Descent with Momentum |
| *'traingd'* | Gradient Descent |

The final step consists of the training of the network, which is achieved by means of the function *train*, also available in the *Deep Learning Toolbox*.
Additionally, it is important to perform data normalisation before the training process, in order to obtain a mean close to zero (which will lead to faster learning and convergence). Data normalisation will allow the data to be dimensionless or to present similar distributions within different data sets. Next, two examples of data normalisation are shown. The first, where the *mapminmax* function is used in order to scale the inputs and targets to fall within the $[-1, 1]$ range, and the second, where the *mapstd* function is used, normalising the data by transforming the mean and standard deviation to 0 and 1, respectively. In lines 4 to 6 of the examples, it shown how to transform the test data according to the parameters in the training data.

```
[n_inputs,ps_inputs] = mapminmax(inputs);
[n_targets,ps_targets] = mapminmax(targets);
[trnet_n,tr_n] = train(net,n_inputs,n_targets);
test_data_n = mapminmax('apply',test_data,ps_inputs);
test_target_n = net(test_data_n);
test_target = mapminmax('reverse',test_target_n,ps_targets);
```

```
[n_inputs,ps_inputs] = mapstd(inputs);
[n_targets,ps_targets] = mapstd(targets);
[trnet_n,tr_n] = train(net,n_inputs,n_targets);
test_data_n = mapstd('apply',test_data,ps_inputs);
test_target_n = net(test_data_n);
test_target = mapstd('reverse',test_target_n,ps_targets);
```

Due to the nature of the "two moons" classification problem, the first approach is chosen. Lastly, the test data is shown next, in Figure 4. Test data 1 changes the two moons configuration, while test data 2 consists of points within the two moons used in the training set, only sightly changing the points coordinates. The difference between all data sets are more easily

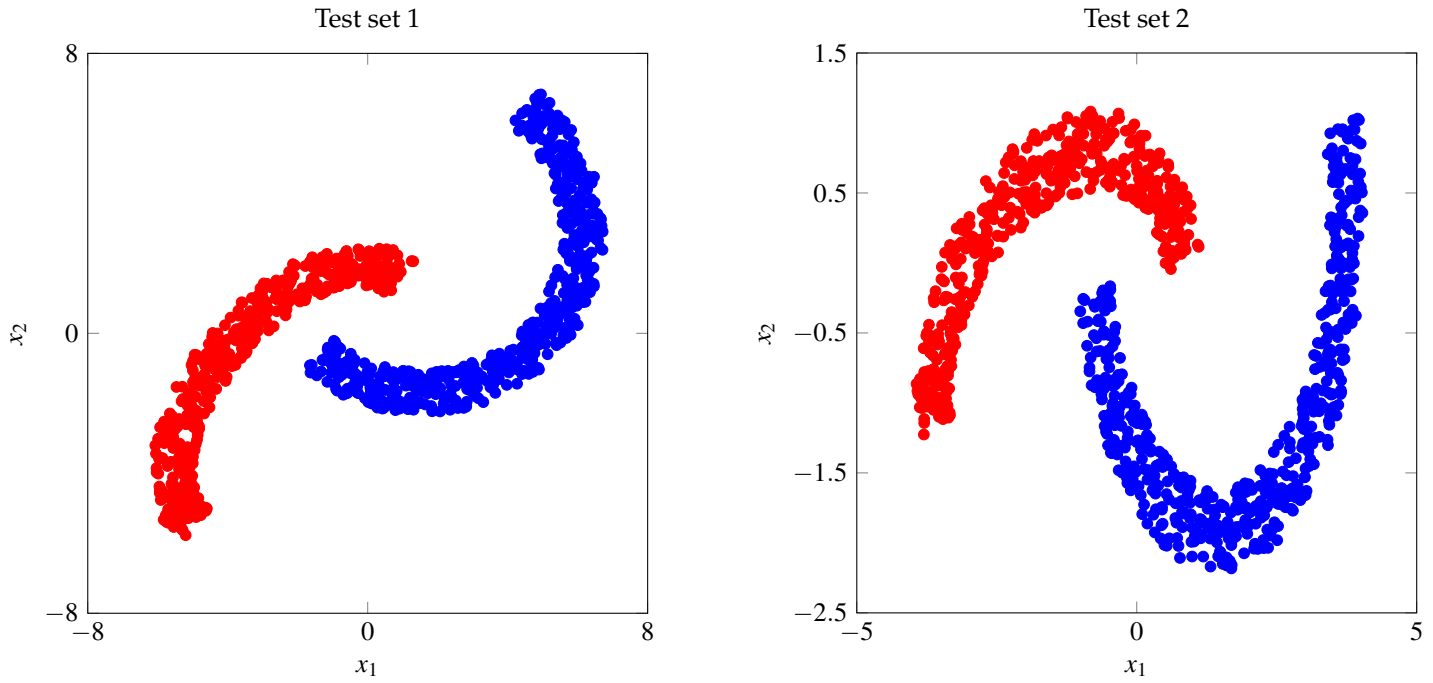


Figure 4: Test data without normalization

understood in Figure 5, which shows that test set 1 is largely different from the training set, while test set 2 is very similar, as both sets are almost completely overlapping in the scatter plot.
However, the *feedforwardnet* function has by default some data pre-processing procedures, such as cleaning constant rows and data normalisation using the *mapminmax*. Thus, the data normalisation step will do nothing, as the input is already normalised. Nevertheless, doing this previous data normalisation step provides the normalisation parameters *ps_inouts* and *ps_targets* so that when testing with different datasets the data can be fed to the net with the correct format.
Because the size of the input layer is 2, it is possible to visualise the decision boundary obtained by the training of the neural network. In order to have a visual representation of the decision boundary, the following code aids in the visualisation of the trained boundary, where the coordinates of points defined in a mesh grid are passed through the trained network and thus, the output will be a colour map showing the output of the network for all points in space.

```
increment = 0.01; %resolution of the meshgrid
xx = min(n_inputs(1,:)):increment:max(n_inputs(1,:));
yy = min(n_inputs(2,:)):increment:max(n_inputs(2,:));
[X,Y] = meshgrid(xx,yy);
grid_coordinates = [X(:), Y(:)]';
final = trnet_n(grid_coordinates);
hold on
colormap('jet');
scatter(grid_coordinates(1,:)',grid_coordinates(2,:)',25,final,'filled');
scatter(n_inputs(1,n_targets==-1)',n_inputs(2,n_targets==-1)',25,'white','filled');
scatter(n_inputs(1,n_targets==1)',n_inputs(2,n_targets==1)',25,'black','filled');
colorbar;
```

## 2.2 Displacements and normal stresses in the proximal femur (2D analysis)

The second studied problem is a 2D analysis of the proximal femur. In section 2.1, the concepts relevant to the coding of this problem were already presented in previous sections, so this section will only show the variables and network architecture. The input and output variables are shown in Figure 6(a), and 6(b) shows the meaning of such variables. Therefore, $P_1$ is any random point located in the greater trochanter and $P_2$ is any random point approximately in the centre of the femur head. In this problem, the objective is to predict the normal stresses $\sigma_{xx}$ and $\sigma_{yy}$ at the proximal diaphysis, and displacements $u_x$ and $u_y$ in the femoral head. The variables $h$ and $\overline{P_1P_2}(l)$ quantify size differences in the model, height and width respectively, and $\theta$ accounts for the model distortions. The test and training data were obtained using FEM analysis on models of 13

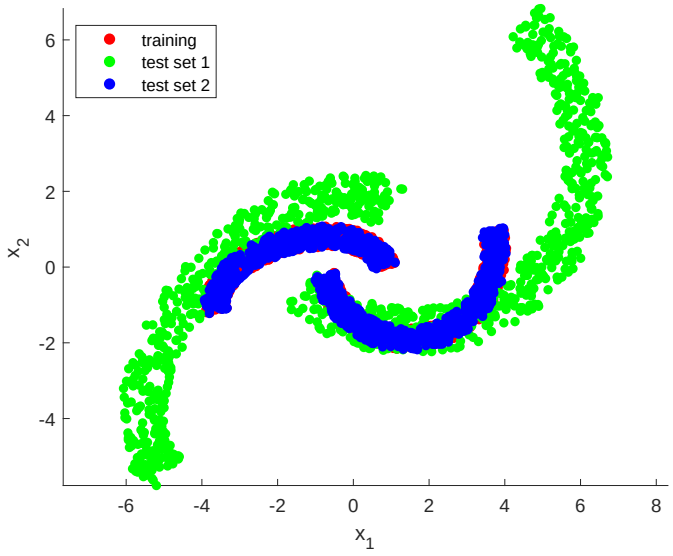


Figure 5: Comparison of the training set and the test sets

different geometries by applying different scales to the $x$ and $y$ axes, and 19 different combinations of angles at which the loads are applied. The magnitude of $F_2$ was defined as being $F_2 = 0.3 \times F_1$, and $F_1$ is enough that the material reaches its elastic limit. The model which was used to gather the training and test data is discretized with 3300 nodes and 3150 quadrilateral elements. The elastic modulus considered for the model is $E = 33$ GPa and the Poisson's coefficient is $\nu = 0.3$. The use of data standardisation is highlighted in this example because human bones present geometrical and dimensional differences from individual to individual. Thus, the data is mapped using the *mapstd* function because human properties will usually follow a normal probability distribution. This will transform each input and output variable so that the mean $\mu$ is 0 and the standard deviation $\sigma^2$ is 1.
A total of *n_instances* = 152 analyses were run in order to obtain the necessary data. First, the simulation files were read and summarised into a table containing all the inputs and outputs named *all_data* with the following structure:

| $h$ | $\overline{P_1P_2}(l)$ | $\theta$ | $\alpha$ | $\beta$ | $u_x$ | $u_y$ | $\sigma_{xx}$ | $\sigma_{yy}$ |
|---|---|---|---|---|---|---|---|---|
| ... | ... | ... | ... | ... | ... | ... | ... | ... |

so the inputs correspond to the first 5 columns of the table and the targets correspond to the last four columns of the table. Additionally, the data is standardised so that each variable has mean $\mu = 0$ and standard deviation $\sigma^2 = 1$.

```
%normalizing the data for the training of the network
inputs = data(:,1:5);
ux = data(:,6); %horizontal displacement
uy = data(:,7); %horizontal displacement
sxx = data(:,8); %normal stress xx
syy = data(:,9); %normal stress xx
[inputs_n,ps_inputs] = mapstd(inputs');
[ux_n,ps_ux] = mapstd(ux(:,1)'); %standardizing the horizontal displacement
[uy_n,ps_uy] = mapstd(uy(:,1)'); %standardizing the vertical displacement
[sxx_n,ps_sxx] = mapstd(sxx(:,1)'); %standardizing the normal stress xx
[syy_n,ps_syy] = mapstd(syy(:,1)'); %standardizing the normal stress yy
```

For this problem the network architecture used in both cases consists of a two layered network, the hidden layer with 20 nodes and the output layer with one node for the output. Figure 7 shows the network used in both cases. The activation function used in the hidden layer was the symmetric sigmoid (*'tansig'*) and the output layer also consisted of a linear transformation, where the input equals the output. Similarly to the first problem, the training function defined by default is used, which is the *trainlm* function. During the training process, 106 of the samples are used in the training, 23 samples are used in validation and 23 samples are used in the testing. The samples used in the training were chosen randomly from the training data. Additionally, 12 samples which had never been used were used to test the accuracy of the network. These 12 samples all present the same distortion but vary between themselves the $\alpha$ and $\beta$ parameters.

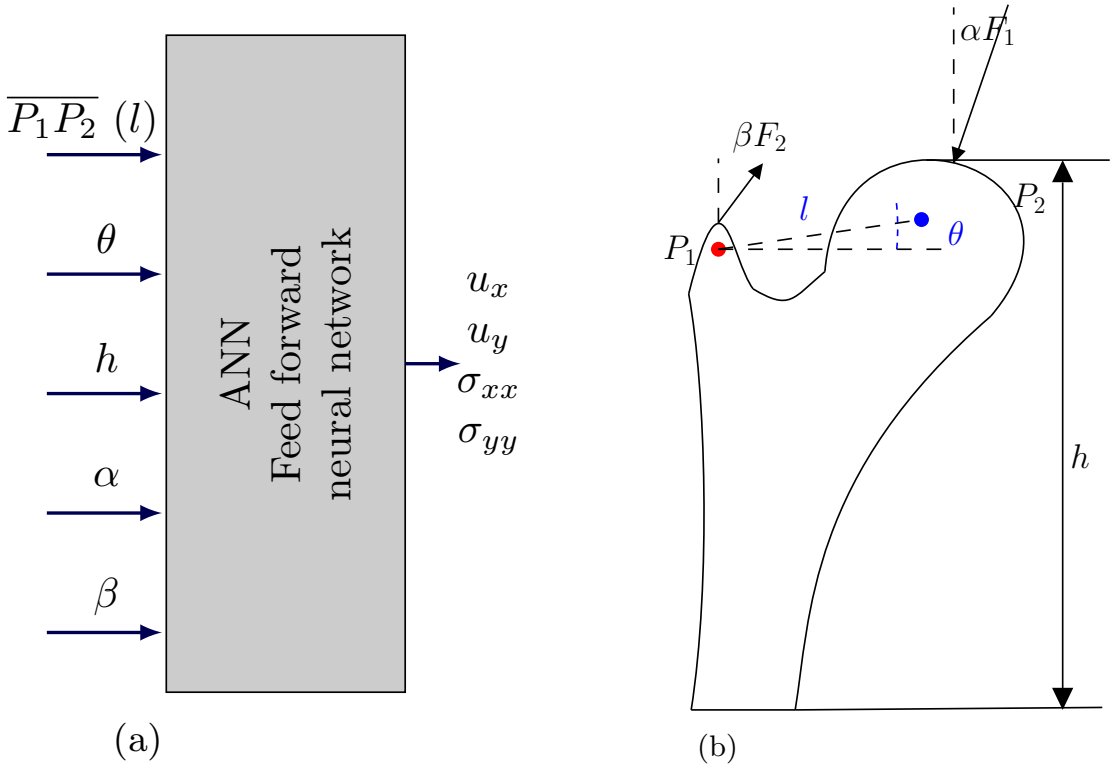


Figure 6: Problem summary (a) input and output variables (b) variable scheme

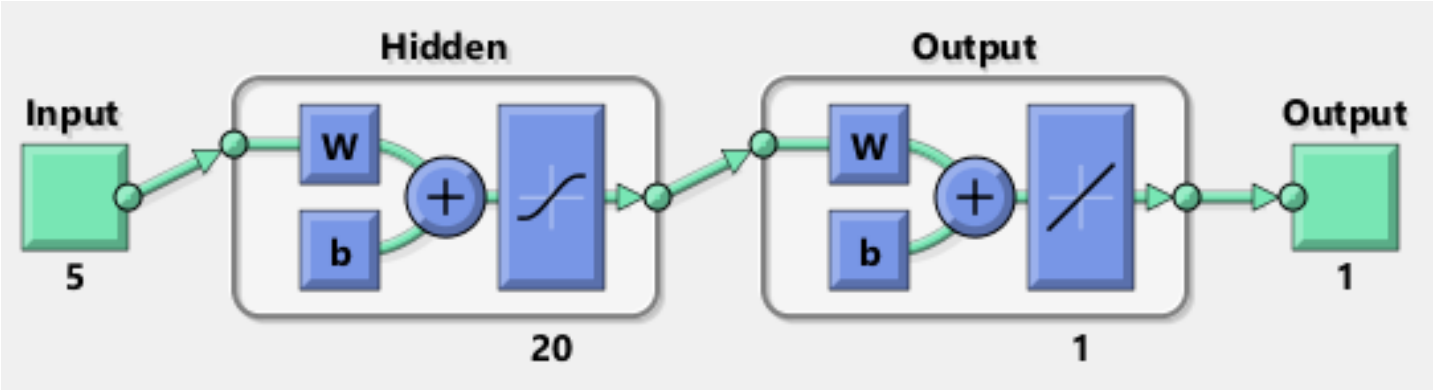


Figure 7: Network architecture used to obtain the displacements $d_x$ and $d_y$ and the normal stresses $\sigma_{xx}$ and $\sigma_{yy}$

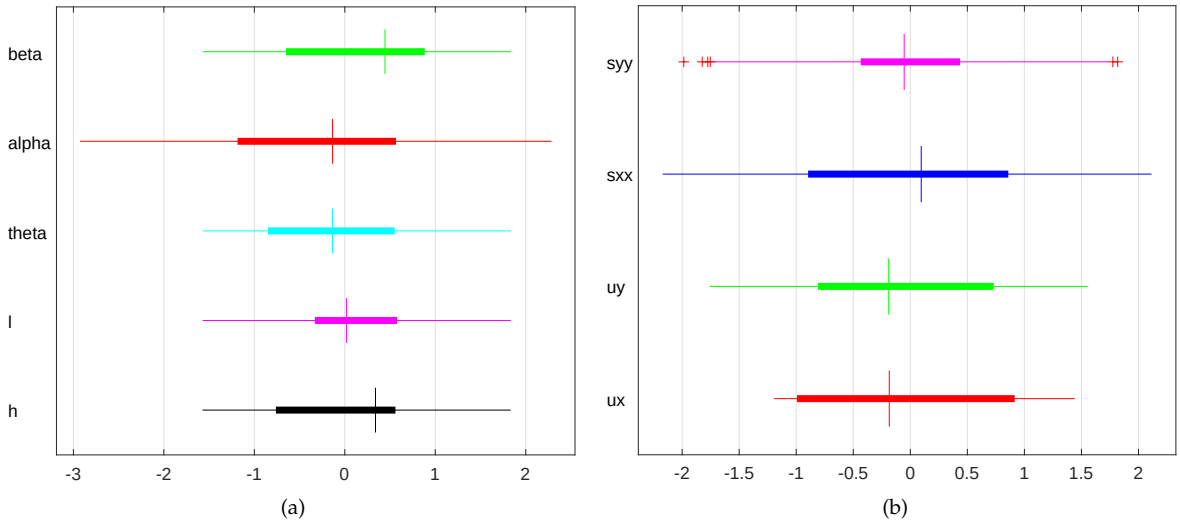


Figure 8: Distribution of the standardized variables (a) input and (b) target

The training procedure requires weight initialisation, which shows a heavy influence in the final training result of the neural network. In order to achieve the best possible weight initialisation, the network was initialised and trained $N$ times. The final network corresponds to the initialisation which provided the lower mean absolute percentage error (MAPE) with the 12 additional samples, which had not been seen by the network. The MAPE is given by

$$MAPE = \frac{1}{n}\sum_{t=1}^{n}\left|\frac{A_t - P_t}{A_t}\right| \tag{5}$$

where $A_t$ is the actual value, calculated through the FEM and $P_t$ is the predicted value from the artificial neural network. The $N$ value was determined iteratively until the network with the best performance showed a maximum relative error lower than 10% within the 12 samples not previously seen by the network, starting $N$ at $N = 1000$ with increments of 1000. The network initialisation (only for the horizontal displacement, it is the same for the remaining networks) and training is showed next

```
targets_n = ux_n;
net_ux = feedforwardnet(20);
[tr_net_ux,param_ux] = train(net_ux,inputs_n,targets_n);
```

Because the network takes the normalised inputs, the same normalisation parameters are used for the 12 example samples. Having obtained the results from the network, it is necessary to revert the normalisation of the output array.

```
ins_test = [h;P1P2_l;theta;alpha;beta];%inputs for the test case
ins_n = mapstd('apply',ins_test,ps_inputs); %normalized inputs
ux_n_test = tr_net_ux(ins_n); %normalized horizontal displacement output
uy_n_test = tr_net_uy(ins_n); %normalized vertical displacement output
sxx_n_test = tr_net_sxx(ins_n); %normalized normal stress xx output
syy_n_test = tr_net_syy(ins_n); %normalized normal stress yy output
ux = mapstd('reverse',ux_n_test,ps_ux); %unscaled horizontal displacement
uy = mapstd('reverse',uy_n_test,ps_uy); %unscaled horizontal displacement
sxx = mapstd('reverse',sxx_n_test,ps_sxx); %unscaled normal stress xx
syy = mapstd('reverse',syy_n_test,ps_syy); %unscaled normal stress yy
```

The distribution of the standardised input and target variables used in the training of this example is shown in Figure 8.

# 3 Results and discussion

## 3.1 Two-moons

Figure 10(a) shows an example of a run of the trained network on two different test sets. It should be noted that the data division done in the training takes a default data division and weight initialisation and, therefore, the results should change

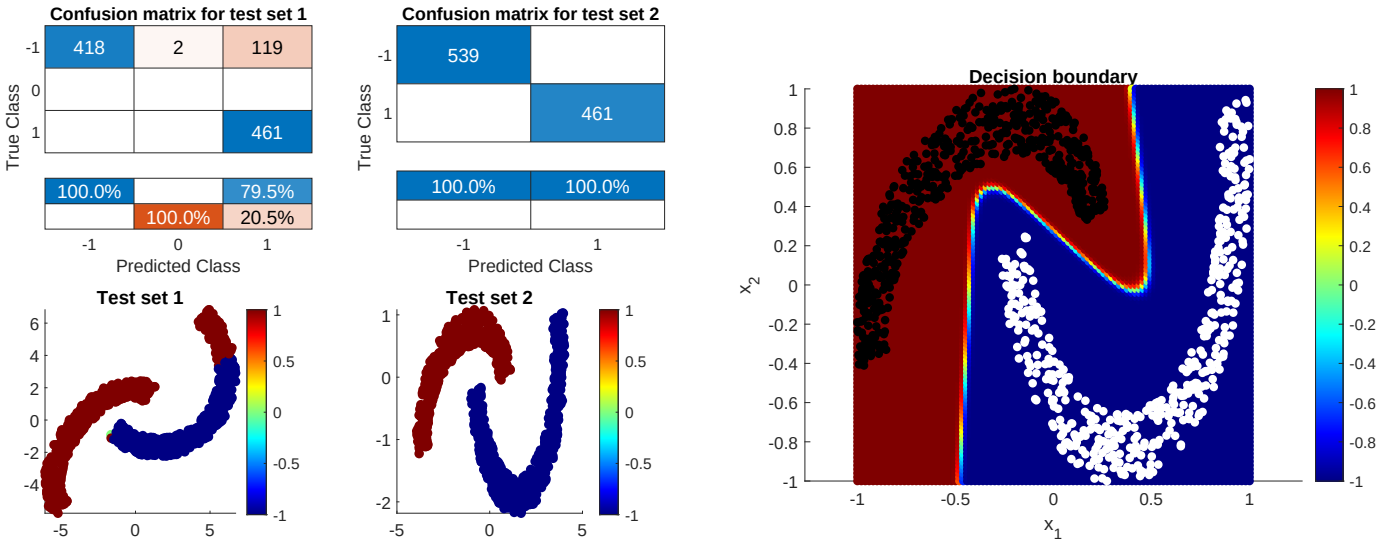


(a) (b)

Figure 9: (a) Example of the trained network on two different test sets and (b) Decision boundary for normalised inputs on the training dataset

Table 3: Performance comparison between the artificial neural networks and the reference results, obtained through the FEM

| | best net (s) | total training (s) | prediction time (s) | FEM time (s) | MAPE | necessary runs |
|---|---|---|---|---|---|---|
| $u_x$ | 1.199 | 1110.135 | 1.374 | 30 | 1.63% | 1000 |
| $u_y$ | 1.807 | 1635.129 | 1.374 | 30 | 1.62% | 1000 |
| $\sigma_{xx}$ | 1.627 | 9269.034 | 1.374 | 30 | 5.20% | 5000 |
| $\sigma_{yy}$ | 2.578 | 2452.89 | 1.374 | 30 | 3.90% | 1000 |

every time the code is run.
Since test set 2 is quite similar to the training set, where the point coordinates differ within the same range of the training data set, the network had 100% precision. On the other hand, test set 1 changes the two moons configuration quite a lot and, therefore, 20.5% of the points are misclassified. The decision boundary obtained is shown in Figure 10(b) for the normalised inputs. The points classified with 1 are marked in black and the points classified with -1 are marked in white.

## 3.2 Displacement and stress in the proximal femur

The results of the trained networks for each of the displacements and stresses are shown in Figure 10. First, it is shown the MSE plotted along the epochs, as well as the absolute percentage error (APE) given by

$$APE = \left| \frac{P_t - A_t}{A_t} \right| \tag{6}$$

along for each of the 12 samples that the network did not see during the training.
Analysing the regression plots (which correlate the predicted outputs with the correct target value), it can be seen that all the displacements were correctly predicted as well as the normal stress $\sigma_{yy}$.
It is possible to visualise that with enough tries, the weight initialisation provided errors that are acceptable bellow 10%. More, from Table 3, which shows how the artificial neural network compares to the FEM performance, it is possible to visualise how a well trained neural network outperforms the FEM in terms of computational time with satisfactory accuracy. Due to the fact that the training data has a relatively small size, the training of one network took, in some cases, a lower time than the prediction. The small amount of data, conjugated with the randomness of the weight initialisation algorithm, led to a high number of tries. Such number was required in order to get a neural network with good enough performance.

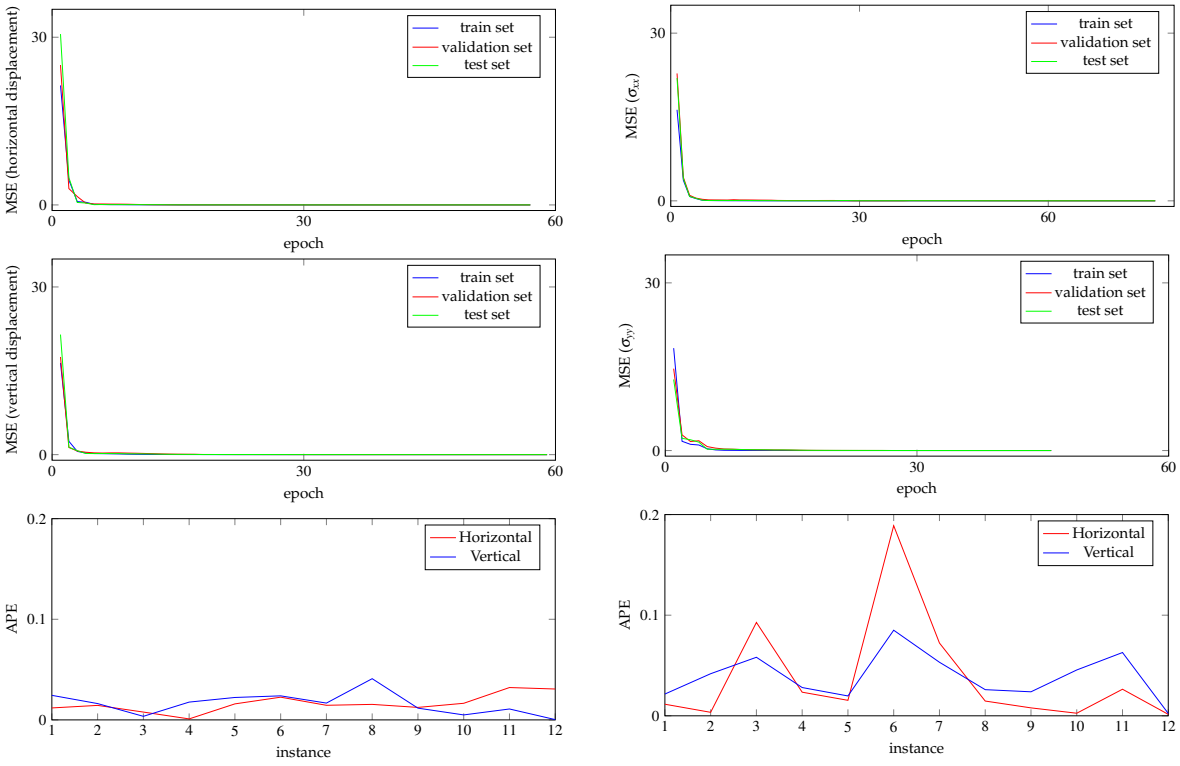


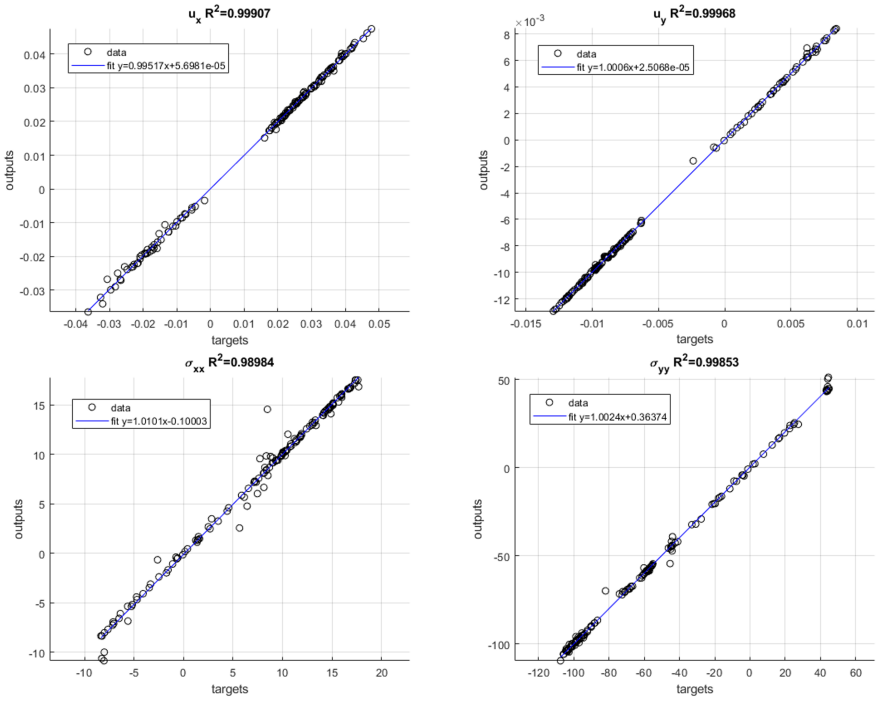


Figure 10: Performance results of the networks with the best performance (a) displacement at the femoral head (b) normal stresses at the diaphysis

Table 4: Importance of each variable using the connection weight approach by Olden et al. [15]

| | $u_x$ | | $u_y$ | | $\sigma_{xx}$ | | $\sigma_{yy}$ | |
|---|---|---|---|---|---|---|---|---|
| | importance | rank | importance | rank | importance | rank | importance | rank |
| $h$ | 0.062400554 | 5 | -1.415369025 | 3 | -0.489007928 | 3 | 0.553022086 | 5 |
| $l$ | 0.837122148 | 4 | 0.08092881 | 4 | 0.893937726 | 2 | -0.657534966 | 4 |
| $\theta$ | 2.847490417 | 1 | -0.072197728 | 5 | 2.162784543 | 1 | -0.732870909 | 3 |
| $\alpha$ | -1.433177231 | 2 | -6.012677872 | 1 | 0.273148366 | 4 | -8.961103865 | 1 |
| $\beta$ | -1.195840853 | 3 | -3.15426349 | 2 | -0.08160777 | 5 | -3.403068005 | 2 |

Consequently, the total training time increased drastically. For example, in the work of Mouloodi et al. [12] (who worked on displacement), experimental data was used to predict load and strain. This work showed the amount of data that is required in order to train the artificial neural network so it presents a low error [12].
Nevertheless, it was possible to train the network to an acceptable level of error. Even though the stresses and displacements are only required at two points of the model, the complex shape of the femur requires FEM analysis in order to output those variables. The trained artificial neural network thus provides good enough data so that the FEM step can be abandoned when calculating such a small number of parameters.
Finally, it is possible to assess the importance of each variable for the calculation of the output, for each variable, using the approach by Olden et al. [15]. This is done by multiplying the matrix of connections weights between the input and hidden layer $W_I$ with the matrix of connection weights between the hidden and the output layer $W_O$. $W_I$ is $[N_{in} \times M]$, where $M$ is the number of neurons in the hidden layer and $N_{in}$ is the number of neurons in the input layer and $W_O$ is $[M \times N_o]$ where $N_o$ is the number of outputs. The result is

$$I = W_I \cdot W_O \tag{7}$$

which is $[N_{in} \times N_o]$ and consists in the importance that each input variable has for the output result. A negative sign signifies a negative correlation of the input variable with the output. Table 4 ranks the variables. Olden's approach shows some advantages in comparison to other feature selection approaches, as it also provides information regarding the excitation or inhibition effect of a variable.
Due to the specificity of each problem, each neural network relies differently on different features. Because the magnitude of the force applied to the femoral head is higher than the magnitude of the force applied to the grater trochanter, it is expected, considering the physical explanation of the problem, that $\alpha$ would consistently rank higher than $\beta$ in variable importance, which was verified. It would be interesting to re-run the training procedure and to each network omit the variables with the least or very low importance. Other differences may be due to the dataset used in the analysis.

# 4 Conclusion

In conclusion, this work shows that a large amount of computational time can be saved through the use of artificial neural networks, especially for models with a large number of nodes where the computational time increases drastically. However, large amounts of data must be acquired in order to have a quality approximation from the neural network. Moreover, the significance analysis of the input features allowed to conclude that even though artificial intelligence is often a "black box" approach, the neural network was capable to capture the physical meaning of the problem, as the most important variables for each case are in agreement with the expectations developed from the mechanics of the problem. Finally, it was shown that the network was capable of solving both classification and regression problems.

# Acknowledgements

The authors acknowledge the funding provided by Ministério da Ciência, Tecnologia e Ensino Superior - Fundação para a Ciência e a Tecnologia (Portugal) and LAETA, under internal project UIDB/ 50022/ 2020 and Doctoral Grant SFRH/ BD/ 151362/ 2021 financed by the by Ministério da Ciência, Tecnologia e Ensino Superior - Fundação para a Ciência e a Tecnologia (Portugal).

# References


[1] Atsuya Oishi and Genki Yagawa. Computational mechanics enhanced by deep learning. *Computer Methods in Applied Mechanics and Engineering*, 327:327–351, 2017.

[2] Jorge Belinha. Artificial Intelligence in Computational Mechanics and Biomechanics. *Journal of Computation and Artificial Intelligence in Mechanics and Biomechanics*, 1(1):1–6, April 2021. doi: 10.5281/zenodo.4669522.

[3] G Yagawa and H Okuda. Neural networks in computational mechanics. *Archives of Computational Methods in Engineering*, 3(4):435, 1996. doi: 10.1007/BF02818935.

[4] Florent Pled, Christophe Desceliers, and Tianyu Zhang. A robust solution of a statistical inverse problem in multiscale computational mechanics using an artificial neural network. *Computer Methods in Applied Mechanics and Engineering*, 373:113540, 2021. doi: 10.1016/j.cma.2020.113540.

[5] Fei Tao, Xin Liu, Haodong Du, and Wenbin Yu. Finite element coupled positive definite deep neural networks mechanics system for constitutive modeling of composites. *Computer Methods in Applied Mechanics and Engineering*, 391:114548, 2022. doi: 10.1016/j.cma.2021.114548.

[6] J.P.A. Ribeiro, L.F.F. Gomes, and S.M.O. Tavares. Artificial Neural Networks Applied in Mechanical Structural Design. *Journal of Computation and Artificial Intelligence in Mechanics and Biomechanics*, 1(1):14–21, April 2021. doi: 10.5281/zenodo.4669797.

[7] Marcus Stoffel, Franz Bamer, and Bernd Markert. Artificial neural networks and intelligent finite elements in non-linear structural mechanics. *Thin-Walled Structures*, 131(April):102–106, 2018. doi: 10.1016/j.tws.2018.06.035.

[8] A. Gholipour and N. Arjmand. Artificial neural networks to predict 3D spinal posture in reaching and lifting activities; Applications in biomechanical models. *Journal of Biomechanics*, 49(13):2946–2952, 2016. doi: 10.1016/j.jbiomech.2016.07.008.

[9] Mahdi Mohseni, Farzad Aghazadeh, and Navid Arjmand. Improved artificial neural networks for 3D body posture and lumbosacral moment predictions during manual material handling activities. *Journal of Biomechanics*, 131(December 2021):110921, 2022. doi: 10.1016/j.jbiomech.2021.110921.

[10] F. Aghazadeh, N. Arjmand, and A. M. Nasrabadi. Coupled artificial neural networks to estimate 3D whole-body posture, lumbosacral moments, and spinal loads during load-handling activities. *Journal of Biomechanics*, 102:109332, 2020. doi: 10.1016/j.jbiomech.2019.109332.

[11] B. S. Reddy, Kim Hong In, Bharat B. Panigrahi, Uma Maheswera Reddy Paturi, K. K. Cho, and N. S. Reddy. Modeling tensile strength and suture retention of polycaprolactone electrospun nanofibrous scaffolds by artificial neural networks. *Materials Today Communications*, 26(February):102115, 2021. doi: 10.1016/j.mtcomm.2021.102115.

[12] Saeed Mouloodi, Hadi Rahmanpanah, Soheil Gohari, Colin Burvill, and Helen M.S. Davies. Feedforward backpropagation artificial neural networks for predicting mechanical responses in complex nonlinear structures: A study on a long bone. *Journal of the Mechanical Behavior of Biomedical Materials*, 128(January):105079, 2022. doi: 10.1016/j.jmbbm.2022.105079.

[13] Saeed Mouloodi, Hadi Rahmanpanah, Colin Burvill, and Helen M.S. Davies. Prediction of load in a long bone using an artificial neural network prediction algorithm. *Journal of the Mechanical Behavior of Biomedical Materials*, 102(April 2019):103527, 2020. doi: 10.1016/j.jmbbm.2019.103527.

[14] Miroslav Kubat. *An Introduction to Machine Learning*. Springer Cham, 2017. ISBN 9783319639130. doi: 10.1007/978-3-319-63913-0.

[15] Julian D Olden, Michael K Joy, and Russell G Death. An accurate comparison of methods for quantifying variable importance in artificial neural networks using simulated data. *Ecological Modelling*, 178(3):389–397, 2004. doi: https://doi.org/10.1016/j.ecolmodel.2004.03.013.

*Journal of Computation and Artificial Intelligence in Mechanics and Biomechanics*
*Volume 2, Issue 2, Page 97-110, 2022*
ISSN 2184-8971

# An elastoplastic constitutive model to simulate the non-linear behaviour of chitosan material for nerve regeneration guide tubes applications

J. Gomes[1], R.M. Natal Jorge[1,2] and J. Belinha[1,3]

[1] *INEGI - Institute of Science and Innovation in Mechanical and Industrial Engineering, Porto, Portugal*
[2] *Department of Mechanical Engineering, Faculty of Engineering, University of Porto (FEUP), Porto, Portugal, rnatal@fe.up.pt.pt*
[3] *Department of Mechanical Engineering, School of Engineering, Polytechnic of Porto (ISEP), Porto, Portugal, job@isep.ipp.pt*

***Abstract***
Neurotmesis is the most severe injury a peripheral nerve can endure. One of the strategies to treat this type of nerve injury is the tubulization technique, consisting of bridging the two nerve tips enclosed by a tube made of a compatible biomaterial. Chitosan scaffolds is one of the most popular (and successful) solutions used for the tubulization technique. After implanting the chitosan tube, it will experience mechanical stimuli due to natural movements, inducing strain-stress states in the biomaterial. It is relevant to characterize the mechanical behaviour of chitosan scaffolds in order to improve the structural design of chitosan tubes. First, in this work, it is proposed an elastoplastic constitutive model to predict the nonlinear behaviour of chitosan scaffolds in both compression and tensile conditions. Then, using the data available from experimental tests documented in the literature, the most relevant mechanical properties for the proposed elastoplastic constitutive model were retrieved, allowing the construction of phenomenological laws for each required mechanical property. The proposed phenomenological law is capable to provide the Young's modulus, the tangent modulus and the yield stress (in both compression and tensile states) as a function of the degree of deacetylation.

DOI: 10.5281/zenodo.7492983

*Article Info*

*Keywords:*
*Phenomenological laws*
*Chitosan*
*Elasto-plasticity*
*Constitutive model*

*Article History*

*Received: 07/10/2022*
*Revised: 13/11/2022*
*Accepted: 07/12/2022*

## 1 Introduction

Every year, there are more than 500.000 new cases of peripheral nerve injuries worldwide due to traumatic events. It is a major cause of morbidity and life-long disabilities and it represents approximately 3% of all trauma patients [1, 2, 3]. There are different causes for injuries in the peripheral nervous system, being the most common direct mechanical trauma and surgical resection secondary to tumour excision [4]. The peripheral nervous system is composed of motor, sensory and mixed nerves. The cell bodies of peripheral nerves are located in the spinal cord and the long cytoplasmic extensions that transmit electrical signals to target organs are called axons [5]. As it is shown in Figure 1, different layers of connective tissue encase peripheral nerves both internally and externally. The epineurium protects and nourishes the nerve fascicles, which are surrounded individually by a layer of connective tissue called perineurium. This layer provides tensile strength to the nerves. Inside each fascicle there is a loose connective tissue matrix called endoneurium that protects and nourishes each axon [6, 7]. Schwann cells surround axons with a membrane of myelin with interposed spaces called nodes of Ranvier, where the saltatory propagation of action potentials occur [8].
Contrarily to what happens in the central nervous system, the peripheral nervous system is able to regenerate after a nerve lesion in the presence of a suitable environment, and to recover some of the lost functions [1, 4, 9, 10]. However, the



*Corresponding Author:*
*Jorge Belinha*
*job@isep.ipp.pt*

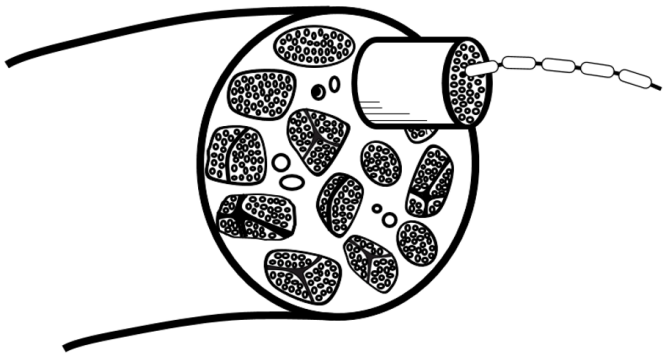

Figure 1: Representation of the cross-sectional area of a peripheral nerve

regenerating capacity and the recovery outcome are dependent on some factors such as the age of the patient, the length and type of injury, the quality of the repair technique, and the proximity of the injury to the nerve cell body [4, 9, 10, 11].

## 1.1 Types of injuries

Seddon [12] and Sunderland's [13] classifications are typically used to define the different types of injuries based on their response. Seddon's classification is based on the architecture of the nerve and its ability to transmit nerve signals [6]. Later on, this classification was expanded by Sunderland and depending on the severity, it divides peripheral nerve injuries into five grades [13]. Neurapraxia (grade 1) is the mildest form of nerve injury and it is related to a block in the fiber conduction due to nerve stretching or compression [8, 14]. It results in temporary motor paralysis, with or without sensory loss. Although demyelination occurs, the structural integrity is preserved since the epineurium, perineurium and endoneurium remain intact, allowing for a full nerve recovery [8, 15]. As a more severe injury, axonotmesis (grade 2) brings more tragic consequences such as complete motor, sensory and autonomic dysfunction. In this case, the structural integrity of the surrounding support structure of the nerve is also preserved, even though the axon suffers some damage and the endoneurium remains intact. As for the recovery rate, it is slow and may be incomplete [6, 14, 15]. The most severe injury is known as neurotmesis (grade 3/4/5), ranging from transection (with intact perineurium) to a completely transected nerve, where there is the total interruption of the structural integrity of the support structure of the nerve [14, 15]. This prevents the occurrence of spontaneous recovery and leads to complete motor, sensory, and autonomic dysfunction [15]. These neurotmetic injuries require surgical intervention while neurapraxia and axonotmetic injuries can be treated by conservative methods [6, 8, 16].

## 1.2 Nerve repair strategies

Being neurotmesis the most severe injury a peripheral nerve can endure, this work only focused on the strategies currently implemented to treat this type of nerve injury. These strategies can be divided into two categories: bridging, using grafting and tubulization techniques, and end-to-end suturing of the nerve stumps [2, 11]. The latter can only be performed in small nerve gaps (<5 mm), where a tension-free coaptation between the proximal and distal nerve stumps is possible. Otherwise, the regrowth of the nerve fibers will be impaired [17, 18, 19]. Also, it has become more apparent over the years that a purely surgical strategy does not address all the molecular and cellular events which occur during the regeneration of the peripheral nerve [4]. On the other hand, bridging nerve gaps of critical length in humans, which are over 3 cm, using an autologous nerve graft (autograft) remains the gold standard for repairing non-suturable peripheral nerve injuries [9, 17, 20, 21]. However, some disadvantages are associated to this technique, such as the need for a second surgery to harvest the nerve graft, and consequent sacrifice of a healthy nerve, the mismatch in size, and the neurological morbidity at the donor site, which makes it a non-optimal strategy [2, 9, 10, 22]. Moreover, because of the unavailability of motor nerves, autografts are primarily obtained from sensory nerves. This is a drawback when it comes to grafting sensory or mixed nerves and may be another reason to explain the poor functional recovery rates associated to autografts [19]. Over the years, an effort has been made in order to develop biomaterials that can be used as substitutes of autografts, including natural and synthetic polymers [22]. These biomaterials, which affect the final outcome, can be easily modified to provide an optimized environment for peripheral nerve regeneration [9, 17]. Some tissue engineering strategies are focused on increasing the ability of these nerve guidance channels to guide and sustain axon regeneration, overcoming the nerve gap limitation

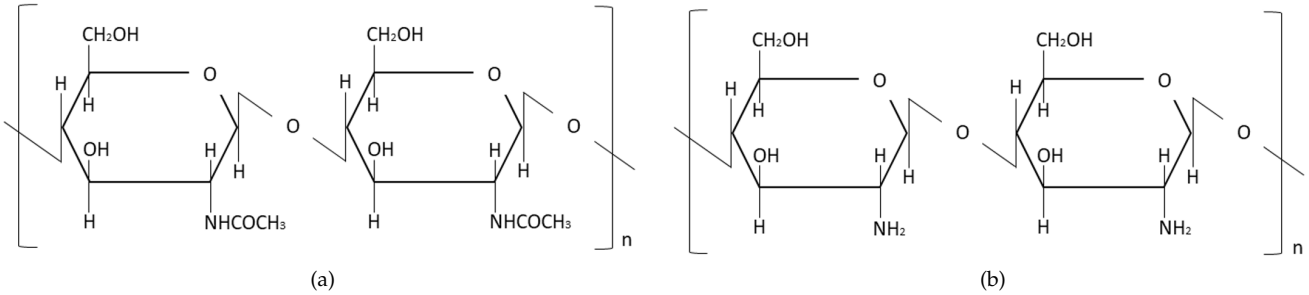


(a) (b)

Figure 2: Chemical structure of chitin (a) and chitosan (b)

[9, 23, 24]. They can assume different forms, being that hollow tubes are the clinically approved alternative to autografts, and are sutured between the proximal and the distal nerve stumps. These nerve guidance channels create a more favourable environment and allow to reach better regenerative results when comparing with autografts [2, 9, 19, 22]. Nowadays there are some FDA-approved nerve guidance channels commercially available, such as NeuraGen$^{TM}$, Neurotube$^{TM}$ and Neurolac$^{TM}$ [9, 25]. Although they avoid donor site morbidity and have an unlimited supply, they also have limitations when it comes to supporting peripheral nerve regeneration and the consequent functional outcomes [1, 19]. These hollow tubes can only be used for small diameter nerves, such as digital nerves, and for nerve defects up to 2-3 cm in length, which leaves the majority of patients with peripheral nerve injuries out of the scope [2, 9, 10, 24, 26]. From these limitations arises the need to construct a nerve guidance channel made from a biomaterial, which has already demonstrated good results in peripheral nerve regeneration and that performs better than autografts in larger nerve gaps. The process of choice of this material must be well considered since the use of different materials and fabrication techniques leads to variable physical properties. One of these materials is chitosan, which has been used as a scaffold to help in the peripheral nerve regeneration process. It can assume many shapes and forms and this variability leads to a set of very different physical, biological and chemical properties that will ultimately influence the results concerning nerve regeneration.

## 1.3 Chitosan

Although many different biomaterials have been used to construct neural scaffolds, for the past years chitosan has been considered a preferable candidate for peripheral nerve regeneration. It derives from chitin, which is a structural element found in the exoskeleton of crustaceans, and it can be obtained by N-deacetylation of chitin [9, 27], Figure 2(a). This polymer is a linear polysaccharide composed of glucosamine and N-acetylglucosamine units which are linked by $\beta$(1-4)-glycosidic bonds [28, 29, 30], Figure 2(b).

Chitosan has a set of characteristics that make it a viable choice as a biomaterial for the construction of nerve guidance channels. Some of these characteristics are its facile chemical modification and excellent reproducibility, which enables it to be applied in medicinal, drug delivery, tissue engineering, and other industrial fields [27, 30, 31, 32]. As a natural polymer, chitosan is regarded as non-toxic and biologically compatible, being that it promotes cell adhesion and proliferation [1, 22, 30, 32]. It also presents an excellent antibacterial and antifungal activity, biodegradability and a film-forming ability [11, 31, 33]. Several studies have demonstrated that chitosan is a good option for neural tissue engineering and more specifically that chitosan tubes promote the repair of the peripheral nervous system [9, 11, 17, 22]. Chitosan nerve guidance channels can undergo surface modification in order to provide guiding and structural cues for growing axons and they can also be constructed as interconnected-porous structures by freezing and lyophilizing methods [17, 34]. In its pure state, chitosan can take many forms that can differ between them on the degree of deacetylation, which is represented by the ratio between glucosamine and N-acetylglucosamine units [28, 35, 36]. The degree of deacetylation is one of the most important properties of chitosan and it allows to differentiate it from chitin considering the amount of free amino groups (NH2) [28, 37, 38]. During the process of deacetylation of chitin, an acetyl group (C2H3O) is removed from its molecular chain, leaving behind an amino group [38]. Thus, when a polymer molecule consists of more than 50% of N-acetylglucosamine units it is known as chitin. The one with more than 50% of N-glucosamine units becomes soluble in aqueous acidic solutions and is known as chitosan [29, 39]. The degree of deacetylation is determined by the conditions selected for the deacetylation process and generally it ranges from 50% to $90-95$% [11, 37, 40]. Moreover, for biological applications, chitosan can be further deacetylated, reaching a degree of deacetylation higher than 95% [38]. The degree of deacetylation influences the physical, chemical and biological properties of this polymer, such as cell response, crystallinity, solubility, and the tensile strength of chitosan films [37, 41]. Considering for example solubility, when the degree of deacetylation is below 70% it

becomes difficult to dissolve chitosan in acetic acid solutions, which makes it harder to fabricate chitosan conduits [23]. Another parameter that varies with the degree of deacetylation is the degradation rate. Several studies have confirmed that highly deacetylated chitosan scaffolds ($> 85\%$) have a lower degradation rate, meaning that they may last in vivo for several months [28, 30, 34, 40]. Therefore, when considering a peripheral nerve injury, the goal is to develop a chitosan nerve guidance channel that maintains its physical structure long enough to ensure nerve regeneration since it takes the proximal regenerating nerve stump several weeks to reach the injured distal nerve stump [29, 42].

### 1.4 The biomechanical behaviour

In order to facilitate the use of chitosan scaffolds for peripheral nerve repair, one must take into account the biomechanical behaviour of the peripheral nerves. The stresses to which nerves are exposed under physiological conditions must be analysed in order to understand how these scaffolds should behave after implantation so they can better play their role as nerve regeneration enablers. Peripheral nerves are subjected to mechanical stresses, which are defined as the applied external forces divided by the cross-sectional area over which they act. They can be applied as tensile, compressive, shear stress or triaxial stress state [43]. Many in vitro and in vivo studies have demonstrated that peripheral nerves behave as non-homogeneous, viscoelastic tissues and present non-linear stress-strain characteristics when subjected to tensile forces [44]. Tension tests can be performed in order to determine the mechanical properties of nerves, whose mechanical behaviour can be described by a stress-strain curve. Experimentally, an increasing uniaxially tensile load can be applied to the specimen, which will deform until a fracture occurs [43, 45]. These loads can be applied perpendicularly or in parallel to the length of the nerve causing transverse or longitudinal stress, respectively. Thus, in physiological conditions, when the nerve bed (defined as the tract formed by the structures that surround the nerve) is elongated due to joint motion, the nerve is placed under increasing tensile stress and it will elongate and glide [43, 46]. In this case, the elongation of the nerve will cause an increase in nerve strain, which will be greater in the nerve segment closest to the moving joint. In other cases, where a tensile stress is applied, peripheral nerves initially present a low elastic modulus that gradually increases with increasing strain until reaching a maximal value [43, 44]. The tolerance to stretching of peripheral nerves can go up to $6-8\%$ of their total length without undergoing morphological and functional changes. On the other hand, further stretching $(> 15\%)$ leads to a complete block of intraneural flow [47]. Under physiological conditions, chitosan scaffolds have low mechanical strength and are unable to maintain a predefined shape for transplantation, which limits their use as nerve guidance channels in clinical applications [9, 22, 32, 33, 48, 49]. Also, because the conduits may compress the regenerating nerve, they may not be able to maintain their physical structure until the injury is healed. This occurs because chitosan is more brittle and rigid than nervous tissue [50]. Determining the mechanical properties of chitosan nerve guidance channels is crucial for they allow to predict their performance in the physiological environment, including their influence on specific cell functions. For example, a balance between strength and flexibility must be found when planning the ideal mechanical characteristics of the nerve guidance channels since they have to be able to hold the nerve in place after being implanted [51, 52]. Chitosan scaffolds can be characterized via compression testing in order to obtain their compressive modulus and/or strength [28]. These values reported in the literature range from 0.0038 MPa to 2.56 MPa for the compressive elastic modulus and from 0.059 MPa to 0.125 MPa for the compressive strength (or ultimate compressive stress) [32]. Scaffolds that do not exhibit any apparent pores can have an elastic modulus from 5 to $7MPa$. These values change whenever a degree of porosity is added to the scaffolds, which decreases both the elastic modulus and the mechanical strength [29]. Soft biomaterials with a low Young's modulus are the preferable candidates when it comes to mimicking the mechanical properties of nerves [50]. There are several factors that influence the mechanical properties of chitosan scaffolds, such as the pore size and orientation, the degradation rate, and the degree of crosslinking [34, 39]. Some technologies and strategies have been upgraded in order to improve the mechanical properties of chitosan scaffolds, which should lead to better outcomes considering nerve regeneration. Crosslinking these scaffolds by the addition of a reinforcement agent, incorporation of a synthetic polymer or complexing with another polymer, are some of the methods that improve the mechanical properties of chitosan and also decrease the degradation rate [32, 48]. This makes chitosan scaffolds less susceptible to the enzymes responsible for their degradation [53]. However, the concentration of added crosslinker agent must not be too high or the biological properties of the chitosan scaffolds might be impaired. For this reason, non-crosslinked chitosan is often chosen for biomedical applications [32].

## 2 Elastoplastic constitutive model

The literature shows that structures made of chitosan present a nonlinear behaviour when submitted to external uniaxial loads [54, 55]. Linear behaviour is followed by a yield plateau before rupture is reached. It is observed that if the yield stress

is reached and the applied load is removed, chitosan specimens experiment permanent and non-recoverable deformations. Thus, in this work, it is proposed to numerically reproduce the behaviour of chitosan material using an elasto-plastic formulation. First, in order to capture the nonlinear behaviour of an elastoplastic material it is necessary to define the mathematical law for the plastic component of the deformation. Thus, three aspects must be considered: a yield criterion (permitting to analyse the beginning of the plastic regime and indicating the stress level in terms of the stress tensor); a flow rule (defining the relationship between stress and deformation after plastification); and a hardening law (describing if, and how, the yield criterion depends on the plastic deformation) [56]. The yield criterion permits to define the beginning of the plastic regime. Usually, a yield criterion can be formulated as: $F(\sigma,\kappa) = f(\sigma) - \sigma_Y(\kappa) = 0$. The yield criterion allows to define the beginning of the plastic regime. The yield criterion $F(\sigma,\kappa)$ depends on the stress tensor $\sigma$ and on the hardening parameter $\kappa$. Notice that the yield criterion expression allows to define the triaxial stress state, $\sigma$, as a scalar function, $f(\sigma)$. It is the scalar value from $f(\sigma)$ that will be compared with the material yield stress $\sigma_Y(\kappa)$, obtained experimentally. If the stress state at a material point exhibits $f(\sigma) > \sigma_Y(\kappa)$, it means that the point shows an elastic behaviour, governed by the linear equations of the theory of elasticity [57]. Instead, if $f(\sigma) \leq \sigma_Y(\kappa)$, it indicates that the point is yielding. The modified Hill's yield criterion is most suited when the material exhibit anisotropy in its plastic behaviour and asymmetry in its yield-stress behaviour [29]. This means that the yield function is able to describe the behaviour of materials with different compressive and tensile yield stresses. The mathematical law for the criterion is represented in equation 1, [29].

$$\left(F\cdot(\sigma_{yy}-\sigma_{zz})^2 + G\cdot(\sigma_{zz}-\sigma_{xx})^2 + H\cdot(\sigma_{xx}-\sigma_{yy})^2 + 2\cdot L\cdot\tau_{yz}^2 + 2\cdot M\cdot\tau_{zx}^2 + 2\cdot N\cdot\tau_{xy}^2\right)^{0.5} + I\cdot\sigma_{xx} + J\cdot\sigma_{yy} + K\cdot\sigma_{zz} = 1 \tag{1}$$

The parameters $F$, $G$, $H$, $L$, $M$, $N$, $I$, $J$ and $K$ are determined experimentally, representing the current state of anisotropy of the material. Considering the material plastically isotropic the value of the material parameters is given by

$$F = G = H = \frac{1}{2}\left(\frac{\sigma_0^t + \sigma_0^c}{2\cdot\sigma_0^t\cdot\sigma_0^c}\right)^2 \tag{2}$$

$$I = J = K = -\frac{\sigma_0^t - \sigma_0^c}{2\cdot\sigma_0^t\cdot\sigma_0^c} \tag{3}$$

$$L = M = N = \frac{3}{2}\left(\frac{\sigma_0^t + \sigma_0^c}{2\cdot\sigma_0^t\cdot\sigma_0^c}\right)^2 = 3F \tag{4}$$

Since the plastic flow is associated with the yield criterion, in this work an associated flow rule is considered - the Prandtl-Reuss flow rule – which defined the plastic strain rate as,

$$d\varepsilon_{ij}^p = d\lambda\frac{\partial f}{\partial\sigma_{ij}} = d\lambda\cdot\mathbf{a} \tag{5}$$

Notice that $d\varepsilon$ is the plastic rate multiplier and $\mathbf{a}$ is the flow vector, normal to the adopted yield function, $f(\sigma)$. Thus, the flow vector can be presented as,

$$\mathbf{a} = \frac{\partial f}{\partial\sigma} = \left\{\frac{\partial f}{\partial\sigma_{xx}}, \frac{\partial f}{\partial\sigma_{yy}}, \frac{\partial f}{\partial\sigma_{zz}}, \frac{\partial f}{\partial\sigma_{xy}}, \frac{\partial f}{\partial\sigma_{yz}}, \frac{\partial f}{\partial\sigma_{zx}}\right\}^T \tag{6}$$

Following the linear elastic generalised Hooke law, the following relation between the stress rate $d\sigma$ and the elastic strain rate $d\varepsilon_e$ is assumed:

$$d\sigma = \mathbf{D}\cdot d\varepsilon_e = \mathbf{D}\cdot(d\varepsilon - d\varepsilon_p) \tag{7}$$

in which $d\varepsilon$ is the total strain rate and $d\varepsilon_p$ is the plastic strain rate. Matrix $\mathbf{D}$ represents the material elastic constitutive matrix,

$$\mathbf{D} = \begin{bmatrix} \frac{1}{E_{xx}} & -\frac{\nu_{yx}}{E_{yy}} & -\frac{\nu_{zx}}{E_{zz}} & 0 & 0 & 0 \\ -\frac{\nu_{xy}}{E_{xx}} & \frac{1}{E_{yy}} & -\frac{\nu_{zy}}{E_{zz}} & 0 & 0 & 0 \\ -\frac{\nu_{xz}}{E_{xx}} & -\frac{\nu_{yz}}{E_{yy}} & \frac{1}{E_{zz}} & 0 & 0 & 0 \\ 0 & 0 & 0 & \frac{1}{G_{xy}} & 0 & 0 \\ 0 & 0 & 0 & 0 & \frac{1}{G_{yz}} & 0 \\ 0 & 0 & 0 & 0 & 0 & \frac{1}{G_{zx}} \end{bmatrix}^{-1} \tag{8}$$

Where $E_{ii}$ is the Young modulus in direction $i$, $\nu_{ij}$ is the Poisson ration and $G_{ij}$ is the shear modulus, with respect to directions $i$ and $j$. Assuming the associated flow rule and considering that the yield surface only depends on the magnitude of the applied principal stresses and of a hardening parameter, equation 7 be rewritten as,

$$d\sigma = \mathbf{D} \cdot (d\varepsilon - d\lambda \cdot \mathbf{a}) \tag{9}$$

Since the stress must remain on the yield surface in order to occur plastic flow, the following has to be verified,

$$dF = \left(\frac{\partial f}{\partial \sigma}\right)^T d\sigma - \frac{\partial \sigma_Y}{\partial \kappa} d\kappa = \mathbf{a}^T \cdot d\sigma - A \cdot d\lambda = 0 \tag{10}$$

being $A$ an hardening parameter that depends on the hardening rule [56], defined by,

$$A = \frac{1}{d\lambda} \frac{\partial \sigma_Y}{\partial \kappa} d\kappa \tag{11}$$

Applying equation 9 into equation 10,

$$d\lambda = \frac{a^T c d\varepsilon}{A + a^T c a} \tag{12}$$

Introducing the value of $d\lambda$ into equation 5, the plastic strain rate can be written as,

$$\varepsilon^p = \partial\lambda \cdot \mathbf{a} = \frac{\mathbf{a}^T \cdot \mathbf{D} \cdot d\varepsilon}{A + \mathbf{a}^T \cdot \mathbf{D} \cdot \mathbf{a}} \cdot \mathbf{a} \tag{13}$$

and then, consequently, using equation 7, it is possible to write the stress rate as,

$$d\sigma = \mathbf{D} \cdot \left(d\varepsilon - \frac{\mathbf{a}^T \cdot \mathbf{D} \cdot d\varepsilon}{A + \mathbf{a}^T \cdot \mathbf{D} \cdot \mathbf{a}} \cdot \mathbf{a}\right) = \left(\mathbf{D} - \frac{\mathbf{D} \cdot \mathbf{a} \cdot \mathbf{a}^T \cdot \mathbf{D}}{A + \mathbf{a}^T \cdot \mathbf{D} \cdot \mathbf{D} \cdot \mathbf{a}}\right) \cdot d\varepsilon = (\mathbf{D} - \mathbf{D}_{ep}) \cdot d\varepsilon \tag{14}$$

Matrix $\mathbf{D}_{ep}$ represents the elasto-plastic constitutive matrix. Since the work hardening hypothesis is employed [56] considering the associated flow rule, it is possible to define explicitly the hardening parameter $A$. Thus, because chitosan $\sigma - \varepsilon$ experimental curves can be adjusted to a linear elastic-linear plastic hardening model, the hardening parameter $A$ can be defined as in [56], i.e.,

$$A = H'(\overline{\varepsilon}_p) = \frac{d\overline{\sigma}}{d\overline{\varepsilon}_p} = \frac{d\sigma}{d\varepsilon - d\varepsilon_e} = \frac{1}{\frac{d\varepsilon}{d\sigma} - \frac{d\varepsilon_e}{d\sigma}} = \frac{1}{\frac{1}{E_t} - \frac{1}{E}} = \frac{E_t}{1 - \frac{E_t}{E}} \tag{15}$$

Notice that $E$ and $E_t$ represent the elastic modulus and the tangential modulus in the reference direction and corresponding stress state (tensile or compression), respectively. In order to build a nonlinear solution procedure, the material behaviour can be modelled in the form of an incremental relation between the incremental stress vector and the strain increment. The "backward-Euler" procedure [58] is considered to force the stress to return to the yield surface. The nonlinear solution can be obtained using the several variations of the Newton-Raphson non-linear solution method, as described in the literature [59]. One of the simplest variations, the initial stiffness method combined with an incremental solution, is shown in Figure 3.

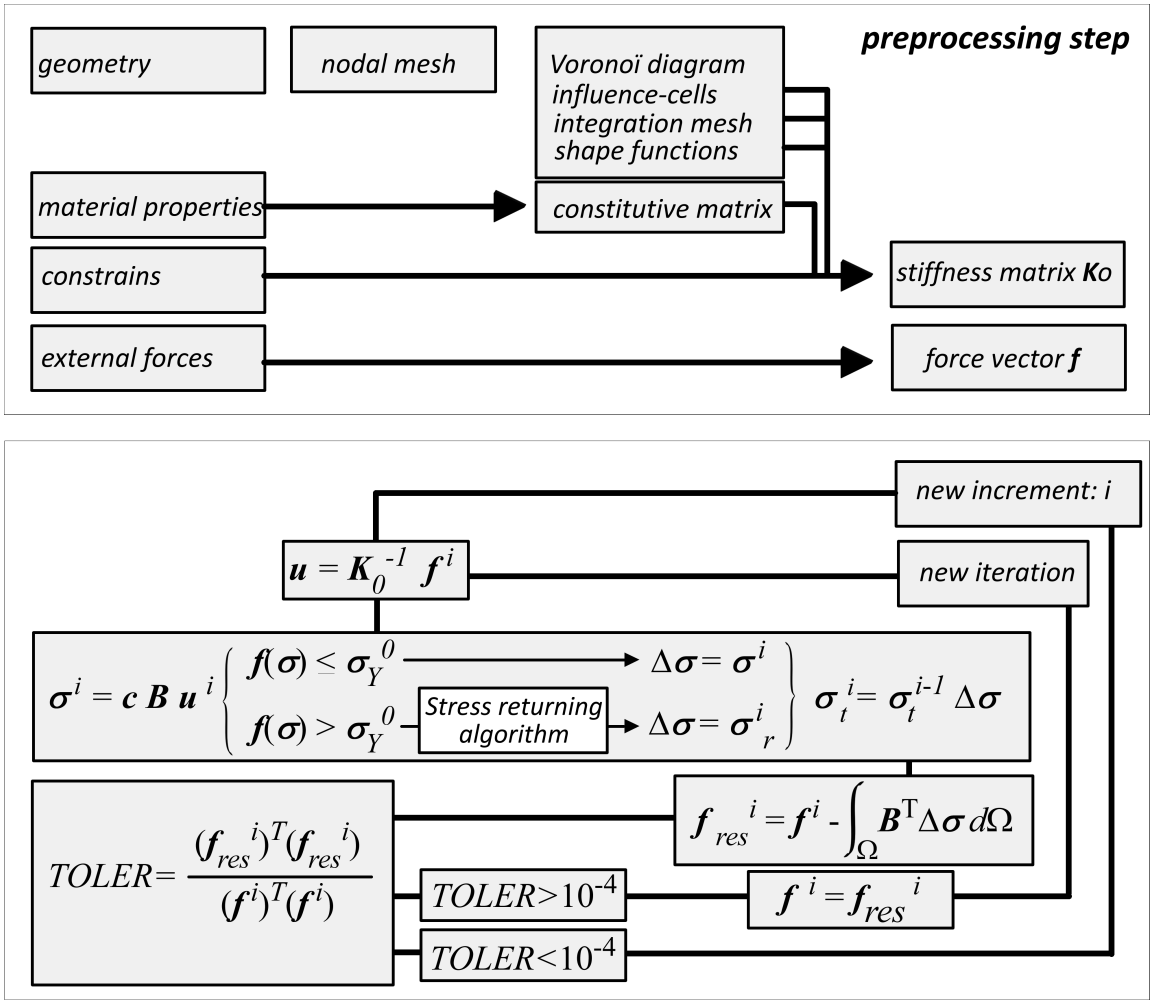


Figure 3: Newton-Raphson non-linear solution method, assuming the initial stiffness method combined with an incremental solution.

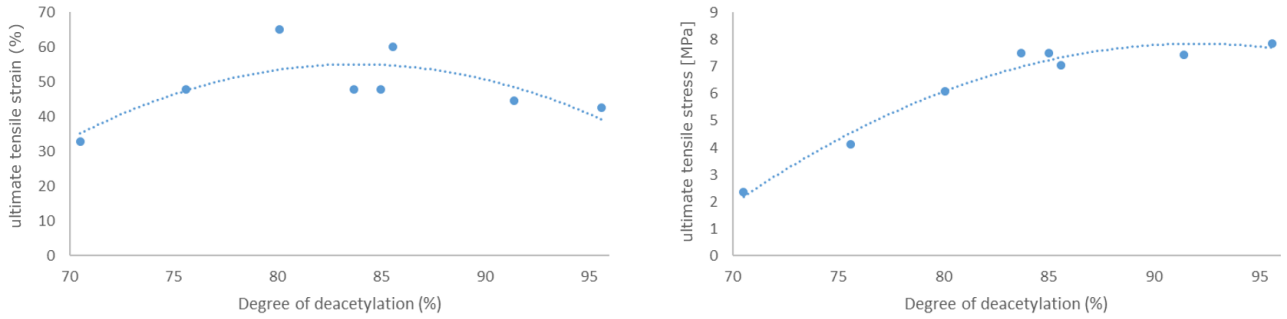


(a) (b)

Figure 4: Relationship between the tensile elongation at break (a) and the tensile strength (b) with the degree of deacetylation of chitosan in a tensile state.

## 3 Phenomenological laws

This work proposes a constitutive material model to allow the prediction of the nonlinear elastoplastic behaviour of chitosan. Experimental tests documented in the literature were studied and gathered [43, 44, 45, 46, 47, 48, 49, 50, 51, 52, 53, 55], and the most relevant mechanical properties for the proposed elastoplastic constitutive model were retrieved. The acquired data allowed to construct the figures presented in this section, and consequently, build the proposed phenomenological laws. The mechanical properties found were obtained by analysing the stress-strain curves documented in the mentioned literature, or by directly assuming the values proposed by their authors.

Both the yield criterion and the corresponding yield surface are considered. The model respects a flow rule defining the relationship between stress and deformation after the plasticity point, and a hardening law that describes if, and how, the yield criterion depends on the plastic deformation. For this, it is important to obtain the mechanical properties of chitosan, such as Young's modulus ($E$), the yield stress ($\sigma_Y$) and the strain for both compression and tension tests. In the compression test, it is also possible to obtain the tangential Young's modulus ($E_t$). These isotropic material properties were related with the degree of deacetylation of chitosan, which importance was explained previously. Therefore, assuming the nonlinear elastoplastic behaviour of chitosan and resorting to the literature, it was possible to obtain these mechanical properties and to analyse how they vary with the degree of deacetylation. The literature shows that when in tension, the curve representative of the relation between breaking elongation and the degree of deacetylation of chitosan depicts a second-order polynomial behaviour. Thus, when constructing the curves relative to the strain both in the elastic and elastoplastic limits, it was considered the same second-order polynomial behaviour. Figures 4 and 5 illustrate the variation of the mechanical properties of chitosan with its degree of deacetylation in a tensile state. These properties include the tensile elongation at break ($\varepsilon_u^t$) (or the ultimate tensile strain), Figure 4(a), the tensile strength ($\sigma_u^t$) (or the ultimate tensile stress), Figure 4(b), the tensile Young's modulus ($E^t$), Figure 5(a), and the tensile elastic limit strain ($\varepsilon_0^t$), Figure 5(b). In Figures 4(a) and (b) and in Figure 5(b), the trend line followed a second-order polynomial behaviour, while in Figure 5(a) it followed a linear behaviour.

The following equations describe the behaviour of the curves presented in Figures 4 and 5.

$$\varepsilon_u^t = -0.1127 \cdot d_d^2 + 18.882 \cdot d_d - 735.87, \quad in \quad [\%], \quad with \quad R^2_{\varepsilon_u^t} = 0.5769 \tag{16}$$

$$\sigma_u^t = -0.0122 \cdot d_d^2 + 2.2457 \cdot d_d - 95.516, \quad in \quad [MPa], \quad with \quad R^2_{\sigma_u^t} = 0.9718 \tag{17}$$

$$E^t = 0.5558 \cdot d_d - 33.747, \quad in \quad [MPa], \quad with \quad R^2_{E^t} = 0.9063 \tag{18}$$

$$\varepsilon_0^t = -0.0008 \cdot d_d^2 + 0.1274 \cdot d_d - 4.6255, \quad in \quad [\%], \quad with \quad R^2_{\varepsilon_0^t} = 0.5376 \tag{19}$$

Being $d_d$ the degree of deacetylation, in [%], and $R^2$ the correlation coefficient of the corresponding approximation curve. Notice that with $\varepsilon_0^t$ and $E^t$ it is possible to estimate the elastic limit stress: $\sigma_0^t = E^t / \varepsilon_0^t$.

In Figures 6, 7 and 8 are represented the variations of the mechanical properties of chitosan with its degree of deacetylation

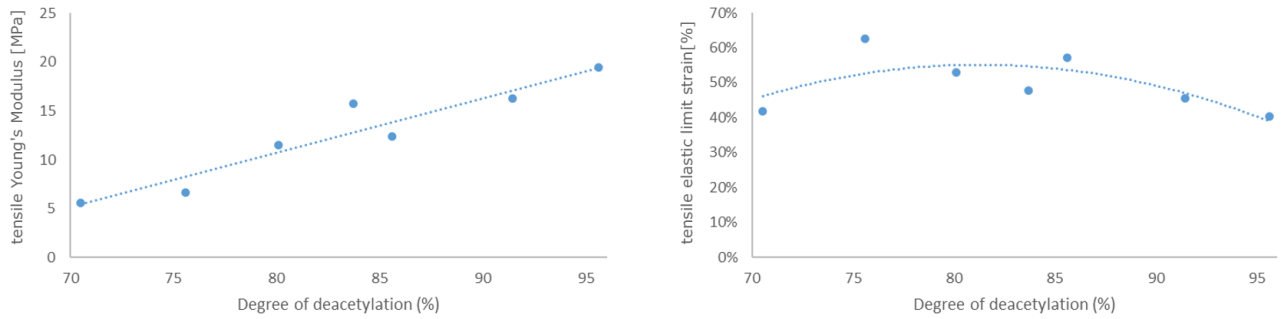


(a) (b)

Figure 5: Relationship between the tensile Young's modulus (a) and the tensile elastic limit strain (b) with the degree of deacetylation of chitosan in a tensile state.

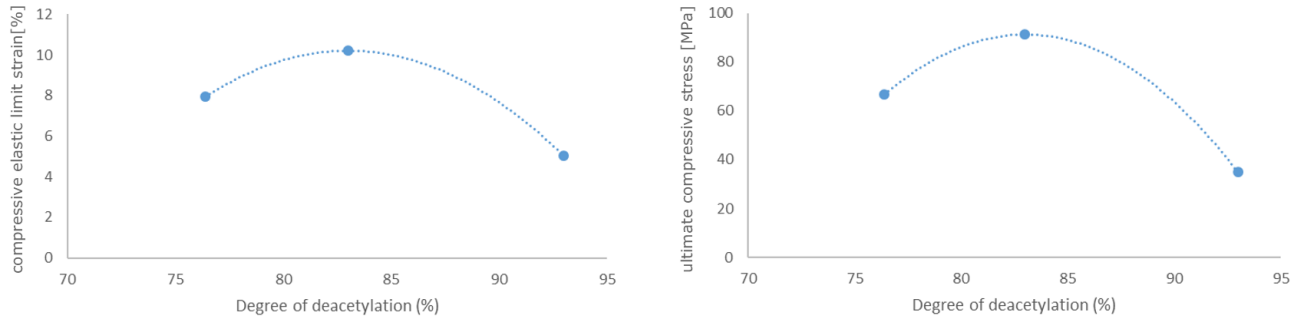


(a) (b)

Figure 6: Relationship between the compression elastic limit strain (a), the compression elasto-plastic limit strain (b) with the degree of deacetylation of chitosan in a compressive state.

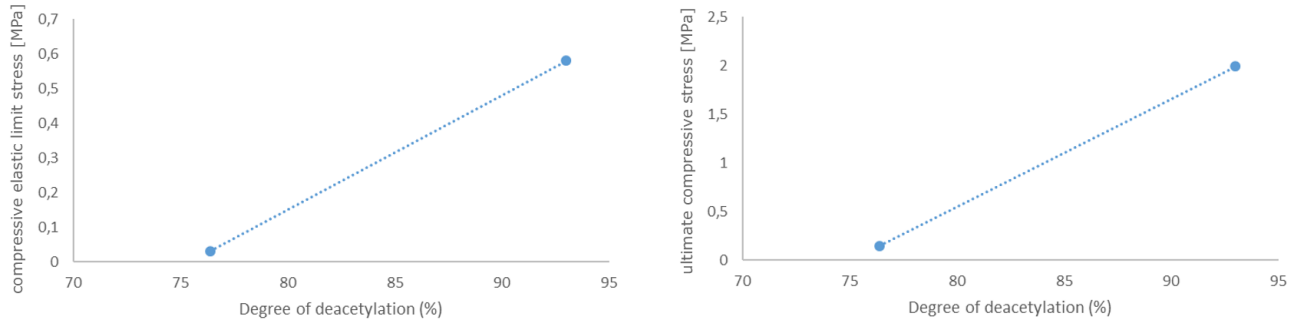


(a) (b)

Figure 7: Relationship between the elastic limit stress (a) and the elasto-plastic limit stress (b) with the degree of deacetylation of chitosan in a compressive state.

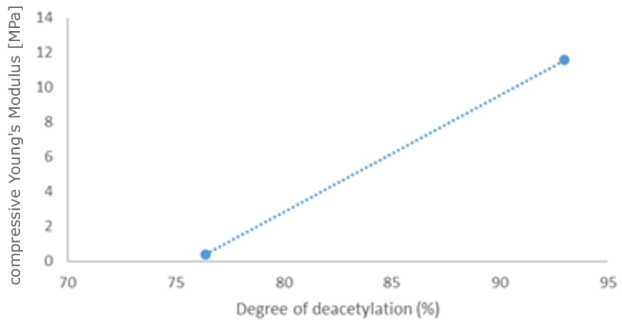


Figure 8: Relationship between Young's modulus (E) with the degree of deacetylation of chitosan in a compressive state.

in a compressive state. These properties are the compressive elastic limit strain ($\varepsilon_0^c$), Figure 6(a), the compressive elastoplastic limit strain ($\varepsilon_u^c$) (or the ultimate compression strain), Figure 6(b), the compressive elastic limit stress ($\sigma_0^c$), Figure 7(a), the compressive elastoplastic limit stress ($\sigma_u^c$) (or the ultimate compression stress), Figure 7(b), and the compression Young's modulus ($E^c$), Figure 8.
Such as in the case of the tensile state, the following equations and correlation coefficients describe the behaviour of the curves presented in Figures 6, 7 and 8.

$$\varepsilon_0^c = -0.0519 \cdot d_d^2 + 8.617 \cdot d_d - 347.4, \quad in \quad [\%], \quad with \quad R^2_{\varepsilon_0^c} = 1.00 \tag{20}$$

$$\varepsilon_u^c = -0.5643 \cdot d_d^2 + 93.668 \cdot d_d - 3795.9, \quad in \quad [MPa], \quad with \quad R^2_{\varepsilon_u^c} = 1.00 \tag{21}$$

$$\sigma_0^c = 0.033 \cdot d_d - 2.4899, \quad in \quad [MPa], \quad with \quad R^2_{\sigma_0^c} = 1.00 \tag{22}$$

$$\sigma_u^c = 0.1109 \cdot d_d - 8.3199, \quad in \quad [\%], \quad with \quad R^2_{\sigma_u^c} = 1.00 \tag{23}$$

$$E^c = 0.6738 \cdot d_d - 51.088, \quad in \quad [MPa], \quad with \quad R^2_{E^c} = 1.00 \tag{24}$$

Again, $d_d$ represents the degree of deacetylation, in $[\%]$, and $R^2$ is the correlation coefficient of the corresponding approximation curve. Although it is possible to obtain the Young's modulus for a compressive state directly from equation 24, it is also possible to obtain the same variable using the values from equations 20 and 22. Thus, following the schematic figure 9, it is possible to understand that all the parameters required to build the bi-linear elastoplastic constitutive model can be obtained with equations 16 to 24. The tensile and compression Young's modulus ($E^t$ and $E^c$, respectively) can be obtained with:

$$\begin{cases} E^t = \dfrac{\sigma_0^t}{\varepsilon_0^t} \\ E^c = \dfrac{\sigma_0^c}{\varepsilon_0^c} \end{cases} \tag{25}$$

The tangent elastic modulus, $E_T^t$ and $E_T^c$ for tensile and compression cases, respectively, can be calculated with:

$$\begin{cases} E_T^t = \dfrac{\sigma_u^t - \sigma_0^t}{\varepsilon_u^t - \varepsilon_0^t} \\ E_T^c = \dfrac{\sigma_u^c - \sigma_0^c}{\varepsilon_u^c - \varepsilon_0^c} \end{cases} \tag{26}$$

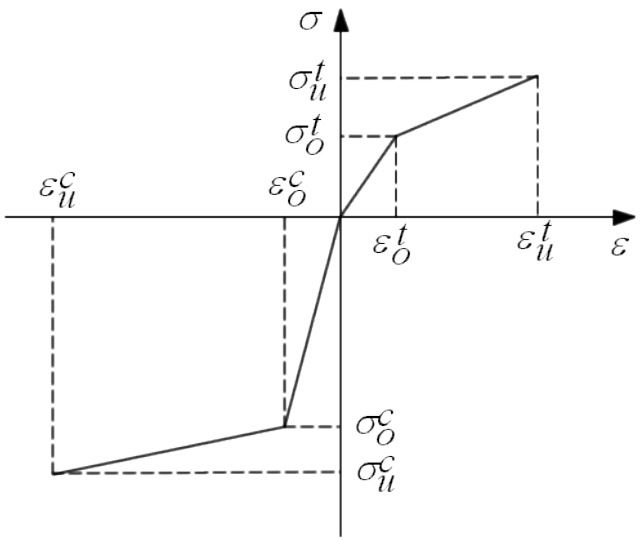


Figure 9: Schematic stress-strain tensile-compression curve.

## 4 Conclusion

Being a nonlinear material, chitosan behaves differently when being compressed or tensioned. When subjected to a compressive force, chitosan presents a clear elasto-plastic behaviour, which can be simulated using an elasto-plastic model. On the other hand, chitosan presents a slight ductile behaviour (almost brittle) when subjected to a tensile force. Nevertheless, it can also be represented with an elasto-plastic model. The degree of deacetylation was shown to have a marked effect on the physicochemical properties of chitosan films. Higher degree of deacetylation chitosan films showed a greater crystallinity, a higher elastic modulus and tensile strength and a lower swelling index than those with lower degree of deacetylation [23]. The relationship here established between different mechanical properties of chitosan and its degree of deacetylation can be adapted to the crystallinity and swelling index of chitosan. With the development of this constitutive model, it is now possible to obtain the different mechanical properties of chitosan for both conditions: compression and tension, as functions of the degree of deacetylation. Combined with advanced discretisation techniques, such as the finite element method or meshless methods, the proposed constitutive model will allow to perform computational simulations capable to predict the non-linear response of chitosan scaffolds, or other chitosan-made structures, under mechanical solicitations. Since computational simulations are less expensive than experimental trials, this numerical approach will contribute to reduce the total cost associated with the research of new geometries of chitosan tubes for the regeneration of the peripheral nerve.

## Acknowledgements

The authors acknowledge the funding provided by Ministério da Ciência, Tecnologia e Ensino Superior - Fundação para a Ciência e a Tecnologia (Portugal) and LAETA, under internal project UIDB/50022/2020.

## References

[1] Kirsten Haastert-Talini, Stefano Geuna, Lars B. Dahlin, Cora Meyer, Lena Stenberg, Thomas Freier, Claudia Heimann, Christina Barwig, Luis F.V. Pinto, Stefania Raimondo, Giovanna Gambarotta, Silvina Ribeiro Samy, Nuno Sousa, Antonio J. Salgado, Andreas Ratzka, Sandra Wrobel, and Claudia Grothe. Chitosan tubes of varying degrees of acetylation for bridging peripheral nerve defects. *Biomaterials*, 34(38):9886–9904, 2013. ISSN 0142-9612. doi: https://doi.org/10.1016/j.biomaterials.2013.08.074.

[2] Yuval Shapira, Michael Tolmasov, Moshe Nissan, Evgeniy Reider, Akiva Koren, Tali Biron, Yifat Bitan, Mira Livnat, Giulia Ronchi, Stefano Geuna, and Shimon Rochkind. Comparison of results between chitosan hollow tube and autologous nerve graft in reconstruction of peripheral nerve defect: An experimental study. *Microsurgery*, 36(8):664–671, 2016. doi: https://doi.org/10.1002/micr.22418.

[3] Cristiana R. Carvalho, Rita López-Cebral, Joana Silva-Correia, Joana M. Silva, João F. Mano, Tiago H. Silva, Thomas Freier, Rui L. Reis, and Joaquim M. Oliveira. Investigation of cell adhesion in chitosan membranes for peripheral nerve regeneration. *Materials Science and Engineering: C*, 71:1122–1134, 2017. ISSN 0928-4931. doi: https://doi.org/10.1016/j.msec.2016.11.100.

[4] Alessandro Faroni, S. Atefeh Mobasseri, Paul J. Kingham, and Adam J. Reid. Peripheral nerve regeneration: Experimental strategies and future perspectives. *Advanced Drug Delivery Reviews*, 82-83:160–167, 2015. ISSN 0169-409X. doi: https://doi.org/10.1016/j.addr.2014.11.010. Regenerative medicine strategies in Urology.

[5] D. Grinsell and C.P. Keating. Peripheral nerve reconstruction after injury: A review of clinical and experimental therapies. *BioMed research International*, 2014:698256, 2014. doi: https://doi.org/10.1155/2014/698256.

[6] Matthew T. Houdek and Alexander Y. Shin. Management and complications of traumatic peripheral nerve injuries. *Hand Clinics*, 31(2):151–163, 2015. doi: https://doi.org/10.1016/j.hcl.2015.01.007.

[7] Hugh G. Auchincloss and Dean M. Donahue. Prevention and management of nerve injuries in thoracic surgery. *Thoracic Surgery Clinics*, 25(4):509–515, 2015. doi: 10.1016/j.thorsurg.2015.07.012.

[8] Richard Brull, Admir Hadzic, Miguel A. Reina, and Michael J. Barrington. Pathophysiology and etiology of nerve injury following peripheral nerve blockade. *Regional Anesthesia & Pain Medicine*, 40(5):479–490, 2015. doi: 10.1097/AAP.0000000000000125.

[9] F. Gonzalez-Perez, S. Cobianchi, S. Geuna, C. Barwig, T. Freier, E. Udina, and X. Navarro. Tubulization with chitosan guides for the repair of long gap peripheral nerve injury in the rat. *Microsurgery*, 35(4):300–308, 2015. doi: 10.1002/micr.22362.

[10] Cora Meyer, Lena Stenberg, Francisco Gonzalez-Perez, Sandra Wrobel, Giulia Ronchi, Esther Udina, Seigo Suganuma, Stefano Geuna, Xavier Navarro, Lars B. Dahlin, Claudia Grothe, and Kirsten Haastert-Talini. Chitosan-film enhanced chitosan nerve guides for long-distance regeneration of peripheral nerves. *Biomaterials*, 76:33–51, 2016. ISSN 0142-9612. doi: https://doi.org/10.1016/j.biomaterials.2015.10.040.

[11] M. Dash, F. Chiellini, R.M. Ottenbrite, and E. Chiellini. Chitosan—a versatile semi-synthetic polymer in biomedical applications. *Progress in Polymer Science*, 36(8):981–1014, 2011. ISSN 0079-6700. doi: https://doi.org/10.1016/j.progpolymsci.2011.02.001. Special Issue on Biomaterials.

[12] H.J. Seddon. Three types of nerve injury. *Brain*, 66(4):237–288, 1943.

[13] S. Sunderland. A classification of peripheral nerve injuries producing loss of function. *Brain*, 74(4):491–516, 1951.

[14] Valeria Chiono and Chiara Tonda-Turo. Trends in the design of nerve guidance channels in peripheral nerve tissue engineering. *Progress in Neurobiology*, 131:87–104, 2015. ISSN 0301-0082. doi: https://doi.org/10.1016/j.pneurobio.2015.06.001.

[15] Borislav Radic, Petra Radic, and Din Durakovic. Peripheral nerve injury in sports. *Acta Clinica Croatica*, 57(3):561–569, 2018. doi: 10.20471/acc.2018.57.03.20.

[16] Shivanand P. Lad, Jay K. Nathan, Ryan D. Schubert, and Maxwell Boakye. Trends in median, ulnar, radial, and brachioplexus nerve injuries in the united states. *Neurosurgery*, 66(5):953–960, 2010. doi: 10.1227/01.neu.0000368545.83463.91.

[17] Sandra Wrobel, Sofia Cristina Serra, Silvina Ribeiro-Samy, Nuno Sousa, Claudia Heimann, Christina Barwig, Claudia Grothe, Antonio Jose Salgado, and Kirsten Haastert-Talini. In vitro evaluation of cell-seeded chitosan films for peripheral nerve tissue engineering. *Tissue Engineering - Part A*, 20(17-18):2339–2349, 2014. doi: 10.1089/ten.TEA.2013.0621.

[18] Yi-Cheng Huang and Yi-You Huang. Biomaterials and strategies for nerve regeneration. *Artificial Organs*, 30(7):514–522, 2006. doi: 10.1111/j.1525-1594.2006.00253.x.

[19] W. Daly, L. Yao, D. Zeugolis, A. Windebank, and A. Pandit. A biomaterials approach to peripheral nerve regeneration: bridging the peripheral nerve gap and enhancing functional recovery. *Journal of The Royal Society Interface*, 9(67):202–221, 2012. doi: 10.1098/rsif.2011.0438.

[20] Salazar Jones, Howard M Eisenberg, and Xiaofeng Jia. Advances and future applications of augmented peripheral nerve regeneration. *International Journal of Molecular Sciences*, 17(9):1494, 2016. doi: 10.3390/ijms17091494.

[21] Alexander R. Nectow, Kacey G. Marra, and David L. Kaplan. Biomaterials for the development of peripheral nerve guidance conduits. *Tissue Engineering - Part B*, 18(1):40–50, 2012. doi: 10.1089/ten.TEB.2011.0240.

[22] Francesca Ruini, Chiara Tonda-Turo, Stefania Raimondo, Pierluigi Tos, Pierfrancesco Pugliese, Stefano Geuna, and Gianluca Ciardelli. Nerve guidance conduits based on bi-layer chitosan membranes for peripheral nerve regeneration. *Biomedical Science and Engineering*, 1(1):1–7, 2016. doi: https://doi.org/10.4081/bse.2016.12.

[23] Cao Wenling, Jing Duohui, Li Jiamou, Gong Yandao, Zhao Nanming, and Zhang Xiufang. Effects of the degree of deacetylation on the physicochemical properties and schwann cell affinity of chitosan films. *Journal of Biomaterials Applications*, 20(2):157–177, 2005. doi: 10.1177/0885328205049897.

[24] Georgios N. Panagopoulos, Panayiotis D. Megaloikonomos, and Andreas F. Mavrogenis. The present and future for peripheral nerve regeneration. *Orthopedics*, 40(1):e141–e156, 2017. doi: 10.3928/01477447-20161019-01.

[25] S. Kehoe, X. F. Zhang, and Boyd D. Fda approved guidance conduits and wraps for peripheral nerve injury: a review of materials and efficacy. *Injury*, 43(5):553–572, 2012. doi: 10.1016/j.injury.2010.12.030.

[26] J.H.A. Bell and J.W. Haycock. Next generation nerve guides: materials, fabrication, growth factors, and cell delivery. *Tissue Engineering - Part B*, 18(2):116–128, 2012. doi: 10.1089/ten.TEB.2011.0498.

[27] Judite N. Barbosa, Isabel F. Amaral, Artur P. Aguas, and Mário A. Barbosa. Evaluation of the effect of the degree of acetylation on the inflammatory response to 3d porous chitosan scaffolds. *Journal of Biomedical Materials Research Part A*, 93(1):20–28, 2010. doi: 10.1002/jbm.a.32499.

[28] Sheeny Lan Levengood and Miqin Zhang. Chitosan-based scaffolds for bone tissue engineering. *Journal of Materials Chemistry B*, 2 (21):3161–3184, 2014. doi: 10.1039/C4TB00027G.

[29] C. Liu, Y. Huang, and M.G. Stout. On the asymmetric yield surface of plastically orthotropic materials: A phenomenological study. *Acta Materialia*, 45(6):2397–2406, 1997. ISSN 1359-6454. doi: https://doi.org/10.1016/S1359-6454(96)00349-7.

[30] T. Kean and M. Thanou. Biodegradation, biodistribution and toxicity of chitosan. *Advanced Drug Delivery Reviews*, 62(1):3–11, 2010. ISSN 0169-409X. doi: https://doi.org/10.1016/j.addr.2009.09.004. Chitosan-Based Formulations of Drugs, Imaging Agents and Biotherapeutics.

[31] Li-Hua Li, Jian-Cheng Deng, Hui-Ren Deng, Zi-Ling Liu, and Ling Xin. Synthesis and characterization of chitosan/zno nanoparticle composite membranes. *Carbohydrate Research*, 345(8):994–998, 2010. ISSN 0008-6215. doi: https://doi.org/10.1016/j.carres.2010.03.019.

[32] Soumen Jana, Stephen J. Florczyk, Matthew Leung, and Miqin Zhang. High-strength pristine porous chitosan scaffolds for tissue engineering. *Journal of Materials Chemistry*, 22:6291–6299, 2012. doi: https://doi.org/10.1039/C2JM16676C.

[33] H.N. Lim, N.M. Huang, and C.H. Loo. Facile preparation of graphene-based chitosan films: Enhanced thermal, mechanical and antibacterial properties. *Journal of Non-Crystalline Solids*, 358(3):525–530, 2012. ISSN 0022-3093. doi: https://doi.org/10.1016/j.jnoncrysol.2011.11.007.

[34] In-Yong Kim, Seog-Jin Seo, Hyun-Seuk Moon, Mi-Kyong Yoo, In-Young Park, Bom-Chol Kim, and Chong-Su Cho. Chitosan and its derivatives for tissue engineering applications. *Biotechnology Advances*, 26(1):1–21, 2008. ISSN 0734-9750. doi: https://doi.org/10.1016/j.biotechadv.2007.07.009.

[35] Joel Jerushan Thevarajah, Matthew Paul Van Leeuwen, Herve Cottet, Patrice Castignolles, and Marianne Gaborieau. Determination of the distributions of degrees of acetylation of chitosan. *International Journal of Biological Macromolecules*, 95:40–48, 2017. ISSN 0141-8130. doi: https://doi.org/10.1016/j.ijbiomac.2016.10.056.

[36] Elson Santiago de Alvarenga, Cristiane Pereira de Oliveira, and Carlos Roberto Bellato. An approach to understanding the deacetylation degree of chitosan. *Carbohydrate Polymers*, 80(4):1155–1160, 2010. ISSN 0144-8617. doi: https://doi.org/10.1016/j.carbpol.2010.01.037.

[37] Su Ching Tan, Eugene Khor, Teck Koon Tan, and Sek Man Wong. The degree of deacetylation of chitosan: advocating the first derivative uv-spectrophotometry method of determination. *Talanta*, 45(4):713–719, 1998. ISSN 0039-9140. doi: https://doi.org/10.1016/S0039-9140(97)00288-9.

[38] Rabiul Hussain, Murshid Iman, and Tarun Maji. Determination of degree of deacetylation of chitosan and their effect on the release behavior of essential oil from chitosan and chitosan-gelatin complex microcapsules. *International Journal of Advanced Engineering Applications*, 1:4–12, 01 2013.

[39] Marguerite Rinaudo. Chitin and chitosan: Properties and applications. *Progress in Polymer Science*, 31(7):603–632, 2006. ISSN 0079-6700. doi: https://doi.org/10.1016/j.progpolymsci.2006.06.001.

[40] J.-K Francis Suh and Howard W.T Matthew. Application of chitosan-based polysaccharide biomaterials in cartilage tissue engineering: a review. *Biomaterials*, 21(24):2589–2598, 2000. ISSN 0142-9612. doi: https://doi.org/10.1016/S0142-9612(00)00126-5. Orthopaedic Polymeric Biomaterials: Applications of Biodegradables.

[41] Y Yuan, BM Chesnutt, WO Haggard, and JD Bumgardner. Deacetylation of chitosan: Material characterization and in vitro evaluation via albumin adsorption and pre-osteoblastic cell cultures. *Materials (Basel)*, 4(8):1399–1416, 2011. doi: 10.3390/ma4081399. PMID:28824150.

[42] Wilfred den Dunnen, Berend Van der Lei, P Robinson, A Holwerda, AJ Pennings, and J Schakenraad. Biological performance of a degradable poly(lactic acid-?-caprolactone) nerve guide: Influence of tube dimensions. *Journal of biomedical materials research*, 29:757–66, 06 1995. doi: 10.1002/jbm.820290612.

[43] KS Topp and BS. Boyd. Structure and biomechanics of peripheral nerves: nerve responses to physical stresses and implications for physical therapist practice. *Physical Therapy - Oxford Academic*, 86(1):92–109, 2006. doi: 10.1093/ptj/86.1.92.PMID:16386065.

[44] P Fleming, B Lenehan, S O'Rourke, P McHugh, K Kaar, and JP McCabe. Strain on the human sciatic nerve in vivo during movement of the hip and knee. *Journal of bone and joint surgery*, 85(3):363–365, 2003. doi: 10.1302/0301-620x.85b3.13220.

[45] William D. Callister Jr. and David G. Rethwisch. Materials science and engineering: An introduction. *John Wiley and Sons*, 1:992, 2018.

[46] MW Coppieters and AM Alshami. Longitudinal excursion and strain in the median nerve during novel nerve gliding exercises for carpal tunnel syndrome. *Journal Orthopaedic Research*, 25(7):972–980, 2007. doi: 10.1002/jor.20310.

[47] U.Z. Sladjana, J.D. Ivan, and S.D. Bratislav. Microanatomical structure of the human sciatic nerve. *Surgical and Radiologic Anatomy*, 30:619–626, 2008. doi: https://doi.org/10.1007/s00276-008-0386-6.

[48] M.J. Simões, A. Gärtner, Y. Shirosaki, R.M. Gil da Costa, P.P. Cortez, F. Gartnër, J.D. Santos, M.A. Lopes, S. Geuna, A.S.P. Varejão, and A.C. Maurício. In vitro and in vivo chitosan membranes testing for peripheral nerve reconstruction. *Acta Médica Portuguesa*, 24(1):43–52, 2011. doi: hhttps://doi.org/10.20344/amp.344.

[49] Ana Colette Mauricio, Andrea Gartner, Paulo Armada-da Silva, Sandra Amado, Tiago Pereira, António Veloso, Artur Varejao, Ana Luis, and Stefano Geuna. *Cellular Systems and Biomaterials for Nerve Regeneration in Neurotmesis Injuries*, page 415–440. 11 2011. ISBN 978-953-307-661-4. doi: 10.5772/24247.

[50] Mingyu Cheng, Jinguang Deng, Fei Yang, Yandao Gong, Nanming Zhao, and Xiufang Zhang. Study on physical properties and nerve cell affinity of composite films from chitosan and gelatin solutions. *Biomaterials*, 24(17):2871–2880, 2003. ISSN 0142-9612. doi: https://doi.org/10.1016/S0142-9612(03)00117-0.

[51] A Pabari, H Lloyd-Hughes, AM Seifalian, and A Mosahebi. Nerve conduits for peripheral nerve surgery. *Plastic and Reconstructive Surgery*, 133(6):1420–1430, 2014. doi: 10.1097/PRS.0000000000000226.

[52] R Seda Tiğli, A Karakeçili, and M. Gümüşderelioğlu. In vitro characterization of chitosan scaffolds: influence of composition and deacetylation degree. *Journal of Materials Science: Materials in Medicine*, 18(9):1665–1674, 2007. doi: 10.1007/s10856-007-3066-x.

[53] Wenling Cao, Mingyu Cheng, Qiang Ao, Yandao Gong, Nanming Zhao, and Xiufang Zhang. Physical, mechanical and degradation properties, and schwann cell affinity of cross-linked chitosan films. *Journal of Biomaterials Science, Polymer Edition*, 16(6):791–807, 2005. doi: 10.1163/1568562053992496.

[54] Wei Wang, Soichiro Itoh, Atsushi Matsuda, Shizuko Ichinose, Kenichi Shinomiya, Yuiro Hata, and Junzo Tanaka. Influences of mechanical properties and permeability on chitosan nano/microfiber mesh tubes as a scaffold for nerve regeneration. *Journal of biomedical materials research. Part A*, 84:557–66, 03 2008. doi: 10.1002/jbm.a.31536.

[55] Ying Wan, Hua Wu, Xiaoying Cao, and Siqin Dalai. Compressive mechanical properties and biodegradability of porous poly(caprolactone)/chitosan scaffolds. *Polymer Degradation and Stability*, 93(10):1736–1741, 2008. ISSN 0141-3910. doi: https://doi.org/10.1016/j.polymdegradstab.2008.08.001.

[56] D.R.J. Owen and E. Hinton. Finite elements in plasticity. *Pineridge Press Limited*, 1:450, 1980.

[57] S. Timoshenko and J.N. Goodier. Theory of elasticity. *Mc Graw Hill*, 1:567, 1933.

[58] R. Borst, M.A. Crisfield, J.J.C. Remmers, and C.V. Verhoosel. Non-linear finite element analysis of solids and structures. *John Wiley & Sons*, 1:516, 2012. doi: 10.1002/9781118375938.

[59] R. Hill. The mathematical theory of plasticity. *Oxford Classic Texts in the Physical Sciences*, 1:366, 1950.